Earth-Science Reviews
May 2023, Volume 240, Pages 104389 (29p.)
https://doi.org/10.1016/j.earscirev.2023.104389
https://archimer.ifremer.fr/doc/00829/94092/

The Palaeoproterozoic Hotazel BIF-Mn Formation as an archive of Earth's earliest oxygenation

Mhlanga X.R. [1, *], Tsikos H. [2], Lee B. [3], Rouxel Olivier [4], Boyce A.C. [5], Harris C. [6], Lyons T.W. [3]

[1] Geology Department, Rhodes University, Makhanda (Grahamstown) 6140, South Africa
[2] Department of Geology, University of Patras, GR-26504 Rio, Greece
[3] Department of Earth & Planetary Sciences, University of California, Riverside, CA 92521, USA
[4] IFREMER, Centre de Brest, Geo-Ocean UMR 6538, F-29280 Plouzane, France
[5] Scottish Universities Environmental Research Centre, East Kilbride G750QF, Scotland, UK
[6] Department of Geosciences, University of Cape Town, Rondebosch 7700, South Africa

* Corresponding author : X. R. Mhlanga, email address : mhlangaxr@live.com

Abstract :

The 2.4Ga Hotazel Formation is a cyclically interlayered sequence of banded iron formation (BIF) and manganese-rich sedimentary rock at the uppermost part of the Neoarchaean-Palaeoproterozoic Transvaal Supergroup in South Africa. It represents an unusual stratigraphic association in the context of the origin of BIF and the coevolution of oxygen and life on early Earth and hence bears special relevance to the environmental conditions and processes that characterized the period leading up to the Great Oxidation Event (GOE) at ca. 2.3Ga. The mineral assemblages that characterize the Hotazel rocks are dominated by carbonate, silicate and oxide minerals, which are traditionally interpreted as predominantly diagenetic in origin, particularly the carbonates. By contrast, primary mineral assemblages are inferred to have been dominated by ferric oxyhydroxides and tetravalent manganese oxides, which show no preservation in the rock record and consequently hinder reconstruction of environmental conditions during sedimentation. Here, we revisit the Hotazel succession with a focus on its bulk-rock and carbonate-specific mineralogical, geochemical and stable isotope (C, Fe) composition by applying for the first time a high-resolution stratigraphic approach to sampling and analysis. Our main aim is to constrain the precursor mineralogy to the Fe- and Mn-rich facies in the Hotazel strata in order to unravel the redox conditions behind the massive cyclic deposition of Fe and Mn at the onset of the GOE. Our carbonate-specific results question traditional diagenetic models for the development of the carbonate fraction of the rocks and instead place the origin of much of the present mineralogy on water-column processes in a stratified basin characterized by successive redox pathways with changing water depth. These pathways exploited a series of thermodynamically predictable electron acceptors for organic carbon recycling, which included – probably for the first time in Earth history – aqueous Mn(III) and O2 as electron acceptors for the oxidation of both Fe(II) and organic carbon. The emergence of Mn(III) was also critical for the development of a Mn redox shuttle, which led to effective water-column stratification between aqueous Mn and Fe in the depositional basin. We conclude that the first known record of Mn(II) to Mn(III) oxidation as recorded in the Hotazel Formation must be a fundamentally diagnostic step in the redox evolution of the oceans and atmosphere in the lead-up to the GOE.

Keywords : Manganese, BIF, Carbonate, Redox, GOE

Introduction and background

The 2.4Ga manganese-bearing Hotazel Formation is one of the key sequences within the Paleoproterozoic chemical sedimentary record as a window to the evolution of oxygen and life in the atmosphere and oceans at the dawn of the Great Oxidation Event (GOE: see Lyons *et al*., 2014, and references therein). The sedimentary succession of the Hotazel Formation records unique three-fold interlayering between Banded Iron Formation (BIF) and Mn-rich sedimentary rock that has not been documented previously from any other classic Precambrian sedimentary sequence in which BIF is a stratigraphically major component (*e.g.*, Hamersley Supergroup of Australia, Minas Gerais Supergroup of Brazil, etc.). Worldwide BIF deposits usually contain negligible amounts of bulk-rock MnO content that hardly ever exceeds 1.0 wt.% on average, but few exceptions do exist such as the Rooinekke and Griquatown BIF of South Africa which contain several wt.% MnO

exclusively in carbonate minerals (Johnson et al., 2013b; Siahi *et al*., 2020). The atypical association between BIF and Mn-rich sedimentation of the Hotazel Formation has been regarded by several previous authors as a strong indication of the GOE. This contention is based on the premise that massive manganese deposition for the first time in Earth history would have been the direct consequence of oxidation of soluble oceanic Mn(II) to insoluble Mn(IV) oxyhydroxides in the presence of free molecular oxygen. The assumption of full oxidation of aqueous Mn(II) to its tetravalent state is in fact intrinsic to several published references that have historically considered the Hotazel Formation as strong evidence for oxic conditions associated with the GOE (*e.g.*, Kirshvink *et al*., 2000; Johnson *et al*., 2016). This assertion comes even though the mineralogy of unaltered sections of the Hotazel rocks registers no preservation of tetravalent Mn minerals (Tsikos and Moore, 1997; Tsikos *et al*., 2003, 2010; Schneiderhahn *et al*., 2006).

The mineralogy of the Hotazel rocks has been reported in several previous publications (e.g., Kleyenstuber, 1984; 1993; Gutzmer and Beukes, 1996; Tsikos and Moore, 1997; Tsikos *et al*., 2003; Schneiderhahn *et al*., 2006). Tsikos and Moore (1997) delineated three major sub-facies within the Fe-rich (BIF) portion of the Hotazel Formation, which have a consistent distribution with the three Mn ore layers that typify the classic Hotazel stratigraphy: hematite-rich BIF in the lowermost part of the succession below the lower Mn ore layer, carbonate-poor BIF between the lower and upper Mn ore layers and carbonate-rich BIF immediately below and above the upper Mn ore layer. Mineralogically, the hematite-rich facies BIF is characterized by an abundance of very fine-grained hematite along with chert, carbonate minerals, and occasional magnetite (Lantink *et al*., 2018). The dominance of hematite imparts a strong red coloration to the rock, which is very similar to that of the characteristic hematitic lutite zones that typify all lithologic transitions between BIF *sensu stricto* and the three Mn ore layers (Fig. 1). By contrast, the carbonate-rich and carbonate-poor BIF facies are hematite-free, quartz- and magnetite-rich rocks, further distinguished by the relative modal abundance of carbonate minerals (calcite, ankerite, siderite) *versus* the Fe-silicate fraction (minnesotaite, stilpnomelane, greenalite). The above mineral phases occur either as monomineralic, mm-thick laminae (mainly in the case of magnetite), or as mm- to cm-thick bands containing variable proportions of chert and Fe-rich minerals (Tsikos and Moore, 1997).

The mineralogy of the Mn-rich layers in the Hotazel Formation is dominated by the Mn silicate braunite (Mn_7SiO_{12}), along with mm-scale laminae, ovoids and disseminations of manganese carbonate minerals (Mn calcite, kutnahorite, minor rhodocrosite), while hematite is a lesser oxide phase, and quartz is curiously absent. The transitional hematite lutite zones display mineralogical composition that is comparable to that of the Mn ore layers, with the only major variable being the modally increased abundance of hematite(+quartz) at the expense of braunite, and hence the progressively higher whole-rock Fe/Mn ratio moving away from peak bulk-rock manganese concentrations at the center of the Mn ore layers (Tsikos and Moore, 1997; Tsikos *et al*., 2003).

It follows from these details that the oxidation state of manganese in the Hotazel strata represents a mixture of Mn(II) and Mn(III), hosted predominantly in the corresponding carbonate and silicate (braunite) mineral fractions. The complete absence of Mn(IV)-oxyhydroxides in the presently observed mineral assemblages does not preclude the possibility that such species were present in the precursor sediment; in fact, it is possible that Mn(IV) mineralogy could have dominated initially but was subsequently erased wholesale via diagenetic reactions that utilized Mn(IV) as an electron acceptor in the presence of reductants such as organic carbon. In fact, one of the most common interpretations in the literature for the presence of low-$\delta^{13}C$ carbonate minerals in the manganiferous portions of the Hotazel Formation (Mn calcite, kutnahorite) is an argument for diagenetic, bacterially mediated reduction of Mn(IV) by co-occurring organic matter (Lovley and Phillips, 1988; Okita *et al*., 1988; Pongari *et al*., 1991; Okita and Shanks, 1992; Nealson and Myers, 1992; Maynard, 2010). This secondary model for carbonate Mn formation finds analogously popular support in the case of BIF siderite and ankerite and their postulated ferric oxyhydroxide precursors.

The absence of Mn(IV)-oxyhydroxides preserved in the Hotazel Formation could also indicate that the precursor Mn species could have been a lower valence oxide such as Mn(III)-oxyhydroxide, possibly due to low pO_2 levels during the time of deposition at the onset of the GOE. Experimental work by Murray *et al*. (1985) has suggested that the final product of abiotic oxidation of dissolved Mn(II) in an aqueous solution is likely to be γ–MnOOH (manganite) at slightly alkaline pH levels. According to Morgan, (2004), this one step oxidation of dissolved Mn(II) could occur through the following reaction:

$$4Mn^{2+}(aq) + O_2(aq) + 6H_2O \rightarrow 4MnOOH + 8H^+$$

Rationale and objectives

The utility of chemical sedimentary rocks such as BIF as proxies for ancient seawater chemical and biological processes and conditions is a frequently pursued topic in past research (*e.g.*, Anbar *et al.*, 2007; Bekker *et al.*, 2012). One of the biggest challenges faced by researchers involved in the study of rocks such as BIF lies with the difficulty in elucidating with confidence the mineralogical composition of the precursor sediments and their causative links to processes operating in the ancient oceanic water column. Indeed, in many instances the exact redox character of the primary sedimentary precipitates can only be assumed or indirectly inferred. For example, a number of previous studies have deduced from the isotopically light carbonate minerals in BIF that the carbon must have originated solely by bacterially mediated coupled reduction of Fe(III) and Mn(IV) oxyhydroxides and anaerobic organic matter oxidation (Walker, 1984; Pecoits *et al.*, 2009; Heimann *et al.*, 2010; Kohler *et al.*, 2013; Posth *et al.*, 2013; Kurzweil *et al*. 2016). To this end, the generally low and variable $\delta^{13}C$ in BIF carbonate minerals is thought to reflect the interplay between two bicarbonate sources in pore fluids: isotopically light bicarbonate sourced through diagenetic organic carbon remineralization ($\delta^{13}C_{TOC}$ value: *ca.* -28 ‰) and isotopically heavy DIC derived from the overlying seawater mass ($\delta^{13}C_{DIC}$ value: *ca.* 0 ‰) (Baur *et al.*, 1985; Kaufman *et al.*, 1990; Klein, 2005; Heimann *et al.*, 2010). Variable mixing of these two bicarbonate reservoirs would account for the isotopic range between -13 and -5 ‰ recorded in BIF deposits globally (Figure 2). An analogous interpretation would also apply in the case of the Mn ore layers in the Hotazel Formation, which likewise contain low-$\delta^{13}C$, Mn-bearing carbonate minerals such as kutnahorite (Tsikos *et al*., 2003; Schneiderhahn *et al*., 2006). Diagenetic Fe(III) and Mn(IV) reduction is also thought to explain variations in the iron isotope ($\delta^{56}Fe$) composition of BIF and Mn-rich sediments (Johnson *et al.*, 2003; 2005; 2008b; Anbar and Rouxel, 2007; Heimann *et al.*, 2010; Craddock and Dauphas, 2011; Planavsky *et al.*, 2012), although in some instances a combination of primary and secondary (diagenetic) fractionation pathways are invoked (*e.g.*, Tsikos *et al*., 2010).

A leading argument that arises from the above discussion is whether carbon isotope depletion in iron and manganese carbonate minerals in chemical sediments and sedimentary rocks should always be taken as evidence for processes and effects that occur exclusively diagenetically, that is, below the sediment-water interface. Such a scenario carries the additional requirement that

chemical precipitates for the formation of these rocks must have been dominated almost entirely by high valence Fe(+Mn) (oxide) precursors as most likely electron acceptors coupled to organic matter remineralization. The reactivity of such precursors in the presence of organic carbon would account for the presently observed reduced Fe-Mn mineralogy, while the complete lack of preservation of the same precursors would be attributed to the overwhelming control of organic matter as effective reductant for both Mn(IV) and Fe(III). The latter possibility is further supported by standard redox chemical reactions between organic carbon and Fe-Mn oxyhydroxides, which suggest that one mole of the former can reduce up to four moles of $Fe(OH)_3$ or two moles of MnO_2, and could result in the quantitative reduction of primary (oxyhydr)oxides to stable new minerals (chiefly carbonates).

Recent studies, however, have revealed a far more complex range of possibilities. For example, several authors highlight the vanishingly low abundances of preserved organic carbon in BIF (Dodd *et al*, 2019; Thompson *et al*, 2019; Jelavić *et al*, 2020), which some researchers attribute to substantial rates of primary water-column precipitation of iron carbonate minerals to account for the carbonate budget in BIF and its bulk isotopic signature (see Thompson *et al*., 2019). Jiang et al. (2022) on the other hand, suggest that the depleted C-isotope signatures of Fe carbonates such as siderite in BIF could be explained by kinetic isotope effects linked to abiotic crystal growth from ambient seawater and/or pore fluids. At the same time, practically all BIF reported in the literature from the Neoarchaean and Palaeoproterozoic contain magnetite (and thus unreduced ferric iron) as arguably the most dominant iron-rich rock-forming mineral. It is therefore likely that diagenetic reduction of Fe(III) by organic matter respiration would have been at best incomplete, unless magnetite formed either in the water column as a primary mineral or represents the product of post-depositional Fe(II) oxidation during later diagenesis (*e.g.,* Rasmussen and Muhling, 2018). Moreover, new evidence from the South African BIF of the Transvaal Supergroup (Siahi *et al*., 2020) indicates that at least a portion of the carbonate fraction of the rocks takes the form of primary high-Mg calcite (HMC) with a low $\delta^{13}C$ signature, which is comparable to that typically seen in the abundant ankerite and siderite of BIF. The related interpretations placed the origin of low-$\delta^{13}C$ ankerite and siderite with isotopically conservative replacement of HMC during diagenesis (Siahi *et al*., 2020). The inference can thus be made that the presently observed complex mixtures of reduced and mixed-valence Fe- and Mn-rich minerals in the Hotazel rocks are likely to have equally complex origins that remain largely unconstrained.

In this more nuanced chemical and mineralogical landscape, the Hotazel Formation offers one of the most promising chemical sedimentary records to shed new light on the long-standing issue of "primary *versus* diagenetic mineralogy." Our present paper aims to address that specific question by applying, for the first time, a high-resolution mineralogical and geochemical approach to the Hotazel rocks through the combination of bulk-rock geochemistry, carbonate-specific analyses, Fe and Mn speciation and stable (C and Fe) isotope systematics. Sequential extraction procedures were based on the method of Poulton and Canfield (2005) as informed by recent improvements in analytical protocols for rocks such as BIF (Oonk *et al.*, 2017) and were applied to both the BIF and the Mn-rich rocks of the Hotazel Formation. Our emphasis in this study is placed on the carbonate fraction of the rocks as a mineral fraction that is both relatively easily extracted through partial dissolution techniques and is almost universally interpreted as entirely diagenetic in origin, forming from the reduction of high-valence precursor (oxyhydr)oxides of iron and manganese. The carbonate fraction therefore carries highest potential to illuminate the relative impact of primary *versus* diagenetic mineral-forming pathways and consequently reconstruct the redox regime during primary deposition and diagenesis of the Hotazel sediments. At the center of our approach is the need to constrain as accurately as possible the likely precursor mineralogical composition of the Hotazel rocks through a rigorous analysis of the present mineral assemblages. Thorough understanding of the primary mineralogy is certain to shed important new light on the redox conditions and processes that surrounded the initial precipitation of the Hotazel sediments — and ultimately on the marine redox regime in the build-up to the GOE.

As our results will hopefully demonstrate, there is no evidence from our present work (and the work of others) that would unequivocally prove the oxidation of soluble Mn(II) to its tetravalent state during deposition of the Hotazel Formation. Instead, we provide new evidence that the Hotazel succession must have been deposited in a marine environment characterized by primary mineral formation under well-developed chemical and isotopic gradients across the ambient water column. These gradients would have resulted, in large part, from the earliest oxidation of aqueous Mn(II) to predominantly its trivalent state, followed by effective redox recycling of (most likely) soluble Mn(III) in the water column by reductants such as Fe(II) and/or organic carbon. Cyclic precipitation of BIF and Mn(III)-rich carbonate sediment would have operated under favorable, periodically fluctuating physicochemical conditions, during which Fe(III) and Mn(III) precipitation as solid primary oxyhydroxides (*e.g.* $Fe(OH)_3$, MnOOH) would have transiently

outcompeted their reductive recycling in the water column and associated primary nucleation of partly to wholly reduced Fe and Mn minerals. Given the presently available age constraints for the Hotazel Formation, we assert that these interpreted processes and conditions would have characterized the period leading up to the GOE. It remains unresolved, however, whether or not peak redox conditions at the GOE would have been conducive to full oxidation of Mn(II) to its insoluble tetravalent state.

Regional Geology

The Transvaal Supergroup of South Africa was deposited on the Kaapvaal Craton during the end of the Archean and early Proterozoic — *i.e.*, the period between 2.65- 2.05 Ga (Moore *et al*., 2001). According to Cheney (1996), the Kaapvaal craton is one of three lithospheric fragments along with the Pilbara Province of NW Australia and the Gruneholgra Province of Antarctica; these together would have formed the ~3.05-1.5 Ga Vaalbara Province. The Transvaal Supergroup is preserved in the Transvaal and Griqualand West Basins (Figure 3), which are geographically disconnected. The Transvaal Basin occurs on the eastern part of a paleo-topographic high known as the "Vryburg arch" and consists of two stratigraphic groups, namely the Chuniespoort and Pretoria Groups. By contrast, the Griqualand West Basin — which lies west of the Vryburg arch — consists of the Ghaap and Postmasburg Groups (Moore *et al*., 2001). The subdivision between the two basins and their stratigraphic correlation have been a major topic of debate in previous studies, with clearest correlation potential demonstrated for the lower stratigraphic groups (*i.e.,* Ghaap and Chuniespoort Groups; see Moore *et al*., 2001, 2012). This study does not include a detailed review of these correlations but rather focuses on the Griqualand West Basin and more specifically on the uppermost part of the Postmasburg Group that contains the Hotazel Formation.

At the lower part of the Griqualand West Supergroup, the Ghaap Group is made up of four major stratigraphic subgroups: the Schmidtsdrif Subgroup with basal shale, quartzite, carbonate and volcanic rocks; the Campbellrand Subgroup containing dolomite, limestone and shale; the Asbestos Hills Subgroup, which successively contains the Kuruman and Griquatown BIFs; and the Koegas Subgroup, dominated by siliciclastic sediments, BIF and lesser carbonate rock (Beukes and Smit, 1987). The Postmasburg Group overlies the Ghaap Group and is made up of a sequence of diverse lithologic units. A glacial diamictite layer of small and variable thickness regionally

(50-150m) known as the Makganyene Formation occurs at the base of the Postmasburg Group (Polteau *et al*., 2006). The Makganyene diamictite is overlain by the Ongeluk Formation, which is comprised almost entirely of massive basaltic andesite and associated volcaniclastics. The Hotazel Formation, which lies above the Ongeluk volcanic sequence and contains BIF intercalated with three manganese-rich ore layers, is the central theme of this paper. The Hotazel Formation is conformably overlain by carbonate rocks (limestone, dolostone) of the Moodraai Formation (Tsikos and Moore, 2001). Together, the Hotazel and Moodraai formations make up the Voëlwater Subgroup in the uppermost stratigraphic portion of the Postmasburg Group in the Griqualand West Basin. A sequence of terrigenous siliciclastic rocks and minor volcanic units belonging to the late Paleoproterozoic Olifantshoek Supergroup overlies the Transvaal Supergroup on a regional angular unconformity.

The age of the Hotazel Formation remained contentious for many years. Indirect age constraints derived from the overlying Mooidraai Formation (2.39Ga) and the underlying Ongeluk volcanics (2.22Ga) placed the Hotazel rocks at the center of an implausible combination of minimum and maximum age constraints (Cornell *et al*., 1996; Bau *et al*., 1999; Fairey *et al*., 2013; see also Fig. 3). This age uncertainty appears to have been conclusively resolved through dating of feeder dykes to the Ongeluk Formation at 2424 ± 32 Ma (Gumsley *et al*., 2017) and further verified by a recently published age for the Hotazel Formation itself at 2413 Ma (Schier *et al*., 2020).

In terms of economic significance, the manganese deposits in the Hotazel Formation constitute one of the largest land-based resources in the world, with approximately 14 billion tons of proven ore reserves estimated to be hosted within the Kalahari Manganese Field (KMF) — the main geographical area for the Hotazel Formation (Cairncross *et al*., 1997; Cairncross and Beukes, 2013; Roy, 2006). Varying ore-types are currently preserved in the KMF. The so-called "Mamatwan-type" ore is the most dominant in terms of volume. This ore type prevails over the largest part of the KMF and is made up of braunite, hematite and manganese-rich carbonates (Mn calcite, kutnahorite) in the form of mm-scale laminae and ovoids, with maximum whole-rock Mn contents usually not exceeding 40 wt.%. The geographical distribution of Mamatwan-type ore corresponds to the largest area of the KMF, which is also devoid of any field evidence for hydrothermal or metamorphic overprints on the primary to early diagenetic assemblages of the Hotazel strata.

The situation is markedly different in the northern KMF, however, where locally complex structural and hydrothermal activity has evidently resulted in the formation of enriched, carbonate-free manganese ore at the expense of a Mamatwan-type precursor, with hausmnanite and calcic braunite being the two dominant mineral species. This enriched ore is known as "Wessels-type" from the homonymous mine in the northern KMF and contains Mn grades that range generally from 45 to well above 50 wt.% — and is therefore highly sought after by mining companies at present (Gutzmer and Beukes, 1995, 1996a, 1996b; Preston, 2001; Tsikos *et al*., 2003). Figure 4 presents a postulated geographical demarcation of areas dominated by primary (low grade) *versus* hydrothermally altered (high grade) Mn ore.

Sampling

Sample collection for this study was carried out on drillcore intersections of the Hotazel Formation from the Gloria Mn mine area in the northern KMF. Drill cores GL137 and GL136 represent complete stratigraphic sections of the Hotazel Formation, and hydrothermal alteration and/or contact metamorphism appear to have had no effect on the rocks (see also supplementary files 7 & 8). The specific locality where both drill cores were obtained offers a practical advantage in studies that employ high-resolution sampling because the overall stratigraphic thickness of the Hotazel Formation there is somewhat lower compared to that seen in the rest of the KMF (see also Tsikos *et al*., 2003). The selected cores are located approximately 500 meters apart at the northwestern area of Gloria mine, where the Mn content is typically of low-grade, Mamatwan-type ore, *i.e.*, between 36-42 wt.% (Figure 4). The proximity of both drillcore localities results in them being practically identical in terms of lithological variability across stratigraphy, with negligible relative thickness variation between the various lithofacies observed. Drilling of these and many similar cores is routinely performed by the company ASSMANG Ltd as part of their mining operations, including grade control and exploration. Sampling for this study was therefore carried out with the generous permission and support by this company.

A total of 184 half-core sections of lengths generally between 5 and 10 cm were collected, specifically 95 samples from drill core GL137 and 89 samples from drill core GL136. All samples from both cores were taken at a resolution of approximately one sample per meter of core section and thus represent the Hotazel stratigraphy in its entirety, with special emphasis placed on

capturing all lithologic transitions at higher sample resolution. Care was also taken during sampling to avoid any secondary silica/carbonate veining that could compromise the integrity of our geochemical dataset. The half-core samples were subsequently split into two quartered sections, one of which was pulverized for geochemical analysis as bulk rock, while the other was archived. A selection of the archived quarters (mainly from drillcore GL137) was processed further for polished thin sectioning to perform petrographic studies and mineral-specific instrumental microanalyses.

In addition to the 184 samples above, a total of 31 mm-scale subsamples were also collected from three representative samples of drillcore GL136 for fine-scale analytical work. The three samples selected for these analyses represent the three endmember lithologies described earlier, namely BIF, Mn ore and hematite lutite. Original core samples were split into two half cores, one of which was further halved into two quartered intersections. One quarter each of the latter was used for continuous subsampling on a mm-scale, whereas the other was archived. Subsampling of the microbanded Hotazel BIF was most challenging due to inherent textural heterogeneity at a sub-mm scale, coupled with the often diffuse contacts between individual chert/carbonate- and magnetite-rich microbands. Individual band thicknesses also vary across the selected BIF section from <1 mm to >1 cm, which results in modal mineralogical variability on a sub-sample to sub-sample basis. A total of 13 successive bedding-parallel slices of BIF were cut from a 35 cm section at individual thicknesses that ranged from 18-51 mm. This step was taken to capture as faithfully as possible the observed band-to-band modal mineralogical variability and assess the geochemical results against such variability. From a textural viewpoint, the hematite lutite and Mn-rich samples are more homogeneous on a cm-scale, consisting of sub-mm Mn-carbonate laminations and lamination-parallel ovoid populations which are interpreted to be of primary to early diagenetic origin (Kleyenstuber.,1984) set in a very fine-grained oxide/silicate matrix. A total of ten subsamples parallel to the carbonate lamination were selected from a 26.5 cm-thick section of hematite lutite, with individual thicknesses varying between 26 and 32 mm per slice. Similarly, eight lamination-parallel subsamples were selected from a 23 cm-thick Mn-rich (ore) section, ranging from 25 to 31 mm thickness per individual slice.

Analytical methodology

Bulk mineralogical results for a diverse selection of our sample set were obtained using standard XRD analyses on a Brucker X-ray diffractometer at Rhodes University. XRD spectra were obtained at 2θ angles between 5° and 65°, which include all rock-forming minerals of the Hotazel Formation. The data extracted were then analyzed using the mineral identification software *Crystal Sleuth*, whereby sample spectra were compared with published ones of the expected mineral phases (Laetsch and Downs, 2006; Anthony *et al.*, 1990). The XRD results were followed up by backscattered electron (BSE) imaging of representative polished thin sections of all key lithotypes using SEM-EDS instrumentation at Rhodes University. Corresponding quantitative mineral-chemical results for carbonate minerals from all major lithofacies were obtained using EPMA facilities at both Rhodes University (JEOL JXA-8230) and the University of Cape Town (JEOL JXA-8100). Routine instrument settings included a beam generated by a Tungsten cathode, 15 kV accelerating potential, 5 nA current and 1 µm beam size. All elements were measured on Kα peaks; counting times were 10 seconds on the peak and 10 on the background for all elements. Commercial "SPI" standards were used for intensity calibration. The standards were quartz (Si), plagioclase (Ca), diopside (Mg), hematite (Fe) and rhodonite (Mn). Calibration acquisitions were peaked on the standards, while unknown acquisitions were peaked on the samples before each point analysis. The data were collected with JEOL software packages. An automated PRZ(Armstrong) matrix algorithm was applied to correct for differential matrix effects, while oxygen was calculated by stoichiometry (see supplementary file 5 for raw data).

Whole-rock major element compositions were determined by XRF spectrometry on a PANalytical Axios Wavelength Dispersive spectrometer at the University of Stellenbosch. Given the very close similarity of the two chosen drillcore intersections of the Hotazel Formation for this study, we deemed it sufficient to analyze all samples from only one of them (GL136) *via* the XRF technique (see supplementary file 2 for raw data). The spectrometer was fitted with a Rhodium tube; the analytical crystals LIF200, LIF220, PE002, GE111 and PX1; a gas-flow proportional counter and a scintillation detector. The gas flow proportional counter uses a 90% Ar to 10% methane gas mixture. Major element analyses were carried out on fused glass disks using a 2.4kW rhodium tube. Matrix effects in the samples were corrected for by applying theoretical alpha factors and measured line overlap factors to the raw intensities measured with the Super-Q Panalytical

software. Regarding the carbonate (*i.e.*, acetate-soluble) fraction, analyses were performed for all samples from drillcore GL137 using the Poulton and Canfield (2005) analytical protocol. Solution extracts were analyzed at the University of California, Riverside, by inductively coupled plasma-mass spectrometry (ICP-MS; Agilent 7500ce) using H_2 and He in the collision cell, following 100-fold dilution in trace-metal grade 2% HNO_3. This protocol is well established for Fe-rich rocks such as BIFs but had until now not been applied on Mn-rich assemblages like those of the Hotazel Formation. We confirmed the efficacy of the acetate extraction by comparing the bulk carbonate Mn/Ca results with corresponding ratios measured on single carbonate grains from the same samples using the electron microprobe. (For more details, refer to chapter 3.5 in Mhlanga, 2020).

Iron isotope data were obtained on all 31 subsamples collected from the three representative core sections of BIF, Mn ore and hematite lutite and for 30 bulk-rock samples from the upper half of drillcore intersection GL137. We chose the latter approach because iron isotope data from the lower half of a very similar core intersection of the Hotazel Formation are already available in the published literature (Tsikos *et al.*, 2010). Iron extractions and instrumental analyses on the produced purified solutions were performed at the University of Brest, France, using established analytical protocols (Rouxel *et al.*, 2005; 2008; 2016). All analyses are reported in the delta notation relative to the IRMM-014 standard, expressed as $\delta^{56}Fe$, which represents the deviation in *per mil* (‰) relative to the reference material. As $\delta^{56}Fe$ and $\delta^{57}Fe$ are on a single mass fractionation line, only $\delta^{56}Fe$ values are reported in this study:

$$\delta^{56}Fe = [(^{56}Fe/^{54}Fe)_{sample} / (^{56}Fe/^{54}Fe)_{standard} - 1] \times 1000$$

An external precision of 0.03 to 0.06 ‰ (2 SD) for $\delta^{56}Fe$ values has been calculated based on duplicated measurements of standard solutions and geo-reference materials performed during the same analytical session.

Finally, bulk carbonate $\delta^{13}C$ values were obtained on all samples from drill cores GL137 and GL136 after reaction with phosphoric acid at 50°C using analytical facilities at SUERC and the University of Cape Town. Values are reported in the delta (δ) notation relative to the Vienna Pee Dee Belemnite (VPDB) standard. The decision to react our samples at a maximum temperature of 50°C was taken because the Hotazel rocks contain almost exclusively calcite and carbonates of the dolomite group, namely ankerite in BIF and kutnahorite in the Mn-rich intervals (Tsikos *et al.*, 2003; 2010) and thus have relatively low acid solubilities. Moreover, calcite and coexisting

dolomite-type carbonates have been previously shown to have comparable $\delta^{13}C$ values within 1-2 ‰ from each other in any given sample (Tsikos *et al.*, 2003). Therefore, it was expected that bulk $\delta^{13}C$ data would fall within a narrow range between the end-member values for each carbonate species, irrespective of relative modal abundance. It must be noted though that a few selected samples do contain some siderite or rhodochrosite, which react very slowly at 50°C. These samples were therefore also reacted at 70°C over a period of three days to test whether the specific carbonates would have had any significant effect on the bulk $\delta^{13}C$ value measured on the same sample powders after reaction at 50°C. Our analytical results demonstrate that this was not the case, a result which is also consistent with similar previous investigations of BIF from the Asbestos Hills Supergroup of South Africa (Siahi *et al*., 2020). Therefore, the possibility of variable degrees of reaction of siderite or rhodocrosite in samples that contain these minerals is expected to have little to no measurable impact on the bulk $\delta^{13}C$ value as determined through reaction at 50°C.

Results

Mineralogy and textures

The mineralogy of the Hotazel Formation in our two drill cores exhibits predictable variability between the contained Fe- and Mn-rich lithofacies, which has been reported in previously published studies (Gutzmer and Beukes, 1996; Tsikos and Moore, 1997; Tsikos *et al*., 2003; Schneiderhahn *et al*., 2006). As stated earlier, the primary emphasis of our mineral-specific work is to provide full context on the carbonate fraction of the rocks, which can best inform the geochemical results that follow. The present section therefore takes an obvious bias toward the carbonate mineralogy of the Hotazel strata as a common denominator across the entire stratigraphic sequence. To this end, an important challenge lies in delineating as robustly as possible the stratigraphic extent of each of the three main lithofacies in view of the often-gradational contact relationships that develop among them.

The contacts between the Hotazel BIF and the hematite lutite transitions are sharp and easy to decipher, due to the stratigraphic distribution of hematite. The Hotazel BIF is known to be completely hematite-free over most part of the stratigraphy, except for the stratigraphically lowermost portion; in all other respects, hematite only begins to make an appearance as the

hematite lutite transitions are approached at the start of each peak manganese cycle (see Fig. 1). Conversely, the stratigraphically upward disappearance of hematite signifies the return to BIF proper at the end of any given Mn cycle. It follows, therefore, that the appearance or disappearance of hematite can be used as the most reliable physical indicator for the lithological transition between BIF *sensu stricto* and the hematite lutite zones.

Contrary to the above, the transitions between hematite lutite and the three Mn-rich layers are highly gradational and hence far more difficult to define. Mineralogically, such transitions develop through a progressively upward increase in modal braunite content at the expense of hematite and chert, which macroscopically manifests in a very gradual change in the color of the rocks from deep red (hematite-rich and braunite-poor) to black (hematite-poor and braunite-rich). In the absence of geochemical data, the macroscopic definition of such color changes understandably becomes very subjective (see also Fig. 1).

Bearing in mind the above challenges, the BIF mineralogy of the Hotazel Formation is dominated by quartz, magnetite and carbonate minerals (mainly ankerite, calcite and lesser siderite; Fig. 5, 6 & 7). Moderate to minor occurrences of iron silicate minerals (mainly minnesotaite, stilpnomelane and greenalite) were also observed under the microscope in selected chert microbands. The typical texture of the Hotazel BIF is one of rhythmic banding between dominantly magnetite-rich bands and chert-rich ones containing variable carbonate, magnetite, and iron silicate abundances (see Fig. 1).

The most common carbonate mineral in the Hotazel BIF is ankerite, which co-exists with practically all other minerals. In chert-dominated bands, ankerite occurs as mainly disseminated, subhedral to euhedral grains or as massive clusters of subhedral grains. Individual grains develop in the form of rhombohedral crystals containing minute chert inclusions (Figure 6A), with or without magnetite inclusions (Figure 6B). In magnetite-dominated bands, ankerite similarly occurs as subhedral to euhedral disseminations and micro-crystalline masses (Figure 6C-F). The main inclusion type in ankerite here is magnetite, with the latter also occurring along ankerite grain boundaries (Figure 6G & H). Although ankerite and magnetite grains are generally clearly separated in space, occasional complex intergrowths between the two are also seen (Figure 6C). Figure 6B displays apparent compositional zonation in individual ankerite grains represented by brighter cores and darker rims. This feature is not prevalent in all ankerite grains observed in the Hotazel Formation and is not explored further in this paper.

Siderite is the other iron carbonate present in the Hotazel BIF. It is modally not as common as ankerite but rather occurs in increased abundance only in the uppermost BIF above the upper Mn ore layer. Like ankerite, siderite occurs in both chert- and magnetite-dominated bands with subhedral to anhedral grains and microscopic chert and magnetite inclusions and magnetite grains scattered around its grain edges (Figure 7). Both ankerite and siderite appear to co-occur as floating rhombohedra in a chert matrix, lacking any compelling evidence that would suggest a sequential mode of formation (Figure 7B & C). The only observable difference between the two iron carbonates in a petrographic sense can be gleaned through BSE imagery: siderite grains are distinguished from ankerite by their increased brightness, which results from their relatively higher iron content and comparatively smaller grain size relative to neighboring ankerite grains. Finally, siderite in magnetite-dominated bands is far less common than ankerite and occurs mainly as scarce subhedral grains with no observable mineral inclusions.

The mineralogy of the hematite lutite transitions is dominated by hematite as the chief oxide mineral species. The carbonate mineralogy has kutnahorite and Mn calcite as the main carbonate phases, with occasional rhodochrosite also present. Braunite becomes increasingly abundant relative to hematite as the Mn-rich ore layers are approached stratigraphically, while micro-crystalline quartz-rich bands are only observed very close to the contacts with BIF (Figure 5G) and decline in abundance as one moves away from BIF toward highest contents of manganese. Representative mineral textures within the hematite lutite as observed across a selection of samples are displayed in Figure 8A-H. Hematite is a matrix constituent in the form of microscopic grains that develop as either anhedral or needle-like crystals (Figure 8D). Braunite, when present, also forms part of the microcrystalline matrix that encloses carbonate laminae and ovoids. Manganese-rich calcite occurs almost exclusively as microcrystalline laminae and ovoids or as mostly anhedral grains in a hematite(±braunite)-dominated matrix. Within laminae and ovoids of Mn-calcite, irregular blobs of kutnahorite typically occur with sharp grain boundaries showing textural signs of possible replacement of Mn calcite by kutnahorite (Figure 8A-D, G-H). Otherwise, kutnahorite appears to be the modally more prevalent manganese carbonate within the hematite lutite, again chiefly in the form of laminae and ovoids (Figure 8A-D, G-H) and less so as disseminations within the hematite-rich matrix (Figure 8F).

Kutnahorite grains commonly exhibit an apparent chemical zonation as seen in Figure (8C, G & H), which suggests that the Mn content at the rim (light grey) must be higher compared to the core (darker grey), a feature that was confirmed by targeted combined BSE imagery and EPMA analysis. Another textural observation is the successive occurrence of specific minerals across contacts between individual carbonate laminae/ovoids and the surrounding hematite-rich groundmass, in the sequence of:

Mn-calcite – kutnahorite – braunite – hematite,

where braunite forms a "border zone" between the carbonate laminae/ovoids and the hematite-dominated lutitic matrix (Figure 8A & E). Figure 8E shows a kutnahorite-dominated ovoid that is enveloped by such a braunite-rich zone. This feature, however, is not consistently observed across all selected samples. In some cases, such as seen in Figure 8C, G & H, the mineralogical sequence appears to lack braunite as an intermediate phase and is instead:

Mn-calcite – kutnahorite – hematite.

We will also show below how the above mineralogical associations are also observed in the Mn ore layers following required adjustments for the specific mineralogy observed therein.

As suggested in the above, the Mn ore mineralogy is in many ways similar to that of the transitional hematite lutite, with the main difference being the modal dominance of braunite as compared to hematite. An additional feature of potential interest is that — contrary to the hematite lutite transitions — the modally dominant carbonate phase in the Mn ore layers is Mn calcite and to a somewhat lesser extent kutnahorite, while rhodochrosite is completely lacking. The color of Mn carbonate laminae and ovoids in the Mn ore layers thus appears to be macroscopically lighter and brighter (essentially off-white) compared to equivalents in the hematite lutites (see also Fig. 1). This relationship is an indication of a higher Ca/Mn ratio in the Mn ore carbonates, a feature that will be confirmed through corresponding geochemical data in the sections that follow. Another notable mineralogical difference between the hematite lutite and Mn ore layers is the common occurrence of small abundances of the mineral friedelite in the latter, particularly in the upper layer (Fig. 5).

Mineral textures of Mn calcite in the Mn ore layers are very similar to those of adjacent hematite lutite transitions. That is, they occur mainly in the form of carbonate laminae and ovoids and as

subhedral to anhedral grains within braunite-dominated matrix/groundmass as seen in Figure 9B-H. Similarly, kutnahorite occurs within laminae and ovoids, which are composed of Mn calcite. Compared to the hematite lutite transitions, chemical zonation of kutnahorite in the manganese ore is less prevalent, as is its overall modal abundance.

The carbonate ovoids contain both manganese carbonates and occur mainly as lenticular features with variable aspect ratio across individual samples or within a single sample (Figure 9A). In some instances, ovoids of a very high aspect ratio appear to coalesce into semi-continuous laminae. The hosting microcrystalline matrix for the ovoids is dominated by braunite and to a lesser extent hematite.

Arguably the most striking mineralogical feature observed in both hematite lutite and Mn ore layers is that of the characteristic mineralogical sequence from carbonate laminae/ovoids to the matrix containing them. In the case of the Mn ore layers, this sequence occurs as:

Mn-calcite – kutnahorite – friedelite – braunite – hematite,

which is seen in Figure 9B and E – H. By analogy to the braunite in the hematite lutite, friedelite appears to envelope the carbonate laminae/ovoids (Figure 9F & H), thus forming a boundary between the carbonate and silicate/oxide dominated zones. The above sequence must be adjusted accordingly in cases where friedelite is not present.

Stratigraphic bulk-rock major element relationships

The bulk-rock geochemistry of the Hotazel Formation comprises mainly Fe, Mn, Ca, Mg and Si, with minor to trace amounts of Ti, P, Na, K and Al (see also Fig. 10). The concentrations of Ti, K and Na are below detection in most samples and, along with the very low and essentially invariant abundances for P and Al, will not be discussed further in this paper. The average composition of the Hotazel BIF from drillcore GL136 (n=43) records bulk rock Fe-oxide content (as Fe_2O_3) at 45.3±7.8 1SD wt.%; SiO_2 content at 35.5±6.8 1SD wt.%; and MnO_2, CaO and MgO concentrations at 0.6±0.7 1SD wt.%, 7.8±4.6 1SD wt.%, and 1.6±0.6 1SD wt.%, respectively. The transitional hematite lutite (n=19) is characterized by relatively lower average SiO_2 concentration compared to that of adjacent BIF (15.5±4.2 1SD wt.%). Also present in these facies are Fe_2O_3 concentrations

comparable to BIF at 34.5±9.4 1SD wt.% and MnO_2, MgO and CaO contents at 14.9±7.2 1SD wt.%, 4.6±2.1 1SD wt.% and 11.5±7.7 1SD wt.%, respectively. The Mn ore layers (n=26) are collectively dominated by high average MnO_2 at 36.2±9.2 1SD wt.%, followed by average CaO and MgO contents of 15.5±6.2 1SD wt.% and 4.0±1.4 1SD wt.%, respectively. By contrast, average concentrations for SiO_2 and Fe_2O_3 are relatively lower compared to the two other lithofacies mentioned above, with values respectively of 8.5±3.8 1SD wt.% and 16.2±9.4 1SD wt.%.

As expected, most major oxide constituents of the Hotazel succession show apparent concentration gradients across the observed lithologic transitions, which result in the higher variance that characterizes the average oxide composition of the hematite lutite transitions. Bulk Fe-oxide values register a gradual decline in concentration from BIF (as high as 57.9 wt.%) to the Mn ore layers (as low as 4.8 wt.%). Bulk silica patterns are similar in that they peak in the BIF layers (48.7 wt.%) and decline to a lowest value of 2.9 wt.% within the Mn ore layers (Figure 10). The average bulk Mn oxide content in BIF barely exceeds 0.5 wt.% but rises progressively to maxima as high as 54.8 wt.% across transitional hematite lutite and ultimately at the center of the Mn ore layers. Finally, peak LOI (loss on ignition) values in the Mn-rich intervals of the Hotazel succession point to corresponding peaks in mineral-bound volatiles (primarily carbonate-hosted CO_2) and thus higher modal carbonate abundance compared to adjacent BIF. With the goal of presenting these bulk-rock geochemical trends in a more systematic and comprehensive way, we have subdivided the Hotazel stratigraphy into three sub-sections that completely capture the three major Fe-Mn-Fe cycles observed. The results of that approach follow.

The lowermost Fe-Mn-Fe sub-cycle of the Hotazel Formation in drill core GL137 spans the interval from 389.5 to 368.3 meters below present surface (mbps). The succession in this interval occurs in ascending order as lowermost BIF – hematite lutite – Mn ore layer – hematite lutite – BIF. The BIF above and below the first Mn sub-cycle contains relatively high bulk Fe_2O_3 compared to average Hotazel BIF, reaching a maximum value of 57.7 wt.%. Similarly, samples from the same BIF record elevated, albeit variable, bulk MnO_2 contents, with concentrations ranging from as low as 0.2 to as high as 3.5 wt.%. By contrast, the corresponding CaO concentration range is lower (0.5 – 7.1 wt.%) compared to average Hotazel BIF. Bulk MgO concentration ranges between 0.4 to 3.5 wt.%, while bulk SiO_2 fluctuates between 28.3 and 47.7 wt.%.

Bulk-rock Fe_2O_3 contents in the hematite lutite transitions of the lower sub-cycle vary widely, from values as low as 12.6 wt.% to as high as 46.9 wt.%. We also observed a wide range of CaO concentrations (2.6 wt.% to 23.4 wt.%). Concentrations of MnO_2 over this interval range more narrowly (13.1 to 24.2 wt.%) and show characteristic upward decreasing and increasing trends above and below the enclosed Mn ore layer, respectively. The same hematite lutite zones register higher bulk-rock MgO content (6.1 - 9.5 wt.%) compared to similar transitions stratigraphically higher. Bulk-rock SiO_2 in the same rocks ranges more narrowly, from 12.0 to 18.9 wt.%.

The lower Mn ore layer records the highest bulk Mn oxide content (reported as MnO_2) compared to the other two Mn ore layers higher in the stratigraphy (23.1 - 34.8 wt.%), confirming its generally known highest economic value. Corresponding Fe_2O_3 concentrations range from as low as 4.8 to as high as 31.9 wt.%. Bulk-rock CaO content is also high, ranging between 12.8 and 28.2 wt.%. Bulk SiO_2 content is, by comparison, very low, with values ranging from 2.9 to 9.5 wt.%.

The second Fe-Mn-Fe cycle is arguably the lithologically most complex of the three, with a succession in ascending order of hematite lutite – Mn ore – hematite lutite – BIF– hematite lutite**.** The three hematite lutite layers in this cycle are all characterized by highly variable bulk-rock Fe_2O_3 concentrations, ranging from as low as 15.9 to as high as 42.1 wt.%. Corresponding bulk-rock CaO contents are also generally high and range widely from 6.4 to 28.3 wt.%. Bulk-rock MnO_2 contents range more narrowly (5.2 - 12.9 wt.%), and the same applies to those for MgO (2.1 - 4.3 wt.%). The very thin Mn ore layer in the middle cycle has bulk-rock Fe_2O_3 concentrations ranging from 18.0 to 30.8 wt.%. This so-called Mn "marker" layer (Tsikos and Moore, 1997) is also characterized by the lowest bulk-rock MnO_2 content (range: 21.5 - 29.4 wt.%) compared to the upper and lower Mn ore layers, as it is generally known to not exceed 30 wt.%. The marker's average CaO and MgO concentrations range from 8.20 to 15.4 wt.% and 3.20 to 7.0 wt.%, respectively. The narrow BIF layer within the upper portion of the cycle has a bulk-rock Fe_2O_3 concentration ranging from 40.6 to 55.9 wt.%, comparable to that of average BIF across the Hotazel stratigraphy. The same applies to its MgO and MnO_2 contents, which are low and practically invariant at ca. 1.6 wt.% and 1.5 - 2.1 wt.%, respectively. The concentration range for SiO_2 in this BIF layer is 19.7 – 29.8 wt.%.

The upper Fe-Mn-Fe cycle represents arguably the least complex cycle in the Hotazel Formation in terms of fine-scale lithological and geochemical variability. It comprises the succession BIF –

hematite lutite – Mn ore – hematite lutite – BIF. The interval from the underlying BIF to the upper Mn ore layer is characterized by a bulk-rock Fe_2O_3 range of 31.1 to 57.9 wt.% and a corresponding MnO_2 concentration range between 0.2 and 0.9 wt.%. Corresponding bulk-rock SiO_2 contents range between 21.8 and 38.5 wt.%, MgO content is between 0.8 and 1.9 wt.%, and CaO contents range from as low as 4.9 to a maximum value of 19.3 wt.%.

The hematite lutite transitions above and below the upper Mn ore layer are characterized by bulk-rock Fe_2O_3 concentrations between 21.1 and 44.3 wt.% and highest bulk-rock MnO_2 content compared to other lutite layers lower in the stratigraphy, ranging from as low as 6.6 wt.% to a maximum of 33.0 wt.%. Bulk-rock CaO and MgO contents range respectively from 5.2 to 17.0 wt.% and 2.1 to 4.9 wt.%, while bulk-rock SiO_2 reaches its highest concentration of 23.9 wt.% near to the contact with the adjacent BIF. Conversely, the lowest silica concentration of 7.01 wt.% occurs in the transition toward the upper Mn ore layer. Samples from this Mn ore layer record bulk-rock MnO_2 concentrations between 24.1 and 46.9 wt.% and the highest bulk-rock Fe_2O_3 content (from 7.0 to a maximum value of 34.3 wt.%) compared to the ore layers stratigraphically lower. Corresponding bulk-rock CaO and MgO contents range respectively from 5.5 to 27.3 wt.% and 2.1 to 4.9 wt.%.

The stratigraphically highest Fe-Mn-Fe cycle ultimately terminates with a ~24-m-thick BIF, which transitions relatively sharply into carbonates of the overlying Mooidraai Formation. The bulk geochemical composition of the uppermost BIF records a range of Fe_2O_3 concentrations between 28.3 and 58.3 wt.%, SiO_2 concentrations between 21.5 wt.% and 48.7 wt.%, CaO concentrations between 3.5 and 19.6 wt.% and MgO concentrations between 0.6 and 2.2 wt.%. Corresponding bulk-rock MnO_2 contents are low and comparable to the rest of the Hotazel BIF stratigraphy, ranging between 0.1 and 0.8 wt.%.

Chemical stratigraphy of the carbonate fraction

Analytical results for the carbonate fraction of the Hotazel succession across the entire length of drillcore GL137 are presented in the supplementary data file 3. The data are reported as wt.% values for the four elements that typically dominate the carbonate fraction of the Hotazel rocks:

Ca, Mg, Fe and Mn. The results are presented below in the context of each Fe-Mn-Fe sub-cycle as defined in the previous section.

The hematitic BIF at the base of the lower sub-cycle exhibits very low carbonate-hosted Fe and Mg, with concentrations ranging respectively between 0.5 and 0.8 wt.% and 0.2 and 0.6 wt.%. Manganese shows higher variability, from 0.1 to 3.0 wt.%, with higher values recorded near the transitional contact with the overlying hematite lutite. Given that the Ca concentration in the same BIF ranges between 0.7 and 5.9 wt.%, we can conclude that the dominant carbonate minerals in this case are intermediate members of the calcite-rhodochrosite series. Stratigraphically higher, the transitional hematite lutite also has very low carbonate-hosted Fe concentrations ranging between 0.1 and 0.7 wt.%. By contrast, carbonate-hosted Mn concentrations range between 2.4 and 10.4 wt.%, pointing to the clear dominance of Fe-poor Mn carbonate. Corresponding carbonate-hosted Ca concentrations range from as low as 0.9 to as high as 15.5 wt.%, and Mg concentrations are from 0.4 to 1.0 wt.%. These abundances suggest a mixture of Mn carbonates, namely Mn calcite and kutnahorite (and possibly some rhodochrosite). The lower Mn ore layer similarly contains essentially Fe-free carbonates, as revealed by the very low carbonate-hosted Fe content of <0.1 wt.%. The corresponding Mn values fluctuate between 3.8 and 10.4 wt.%, a range that is comparable to that of the adjacent underlying hematite lutite transition. High Ca concentrations – ranging from 6.6 to 14.1 wt.% – combined with Mg contents between 0.9 and 1.7 wt.% point to a somewhat more calcic Mn calcite+kutnahorite carbonate assemblage in the lower Mn ore layer compared to those in adjacent hematite lutites.

The second Fe-Mn-Fe cycle as reported earlier records a significantly more transitional bulk-rock geochemistry compared to the lower and upper Fe-Mn-Fe cycles, and this is replicated in the geochemical signal of the carbonate fraction (Fig. 11). The hematite lutite layer at the base of this cycle has low carbonate-hosted Fe (0.1 – 0.3 wt.%) and a Mn concentration range between 1.3 and 12.4 wt.%, while Ca and Mg abundances range respectively between 2.3 and 4.4 wt.% and 0.5 and 1.3 wt.%. Similarly, the overlying thin Mn ore "marker" layer contains negligible Fe, while Mn concentrations range between 7.0 and 12.5 wt.%. Corresponding Ca values are somewhat lower when compared to those of the lower Mn ore layer (3.7 – 15.7 wt.%), and the same applies to Mg (0.4 – 0.6 wt.%). Collectively, these data suggest a dominance of Mn calcite and lesser kutnahorite in the lower portion of the middle Fe-Mn-Fe sub-cycle. The thin overlying BIF contains both Fe

and Mn in its carbonate fraction, with generally low values ranging between 0.5 and 1.5 wt.% and 0.9 and 3.2 wt.%, respectively. Calcium concentration in the same fraction is relatively high (3.1 – 8.2 wt.%), which suggests the continuing dominance of calcite, as supported by the lower corresponding Mg values (0.1 – 0.4 wt.%). The hematite lutite at the top of this sub-cycle is the most calcite-rich sub-facies of the entire core with Ca concentrations of the carbonate fraction reaching a maximum value of 20.0 wt.%. Carbonate-hosted Mg ranges between 0.5 and 1.3 wt.%, while Fe and Mn range respectively from 0.1 to 1.6 wt.% and 3.8 to 9.7 wt.%. The latter points to the distinctly manganiferous character of the contained calcite(+kutnahorite).

As also mentioned earlier, unlike the middle Fe-Mn-Fe sub-cycle, the upper cycle shows a far simpler and more symmetric stratigraphic relationship in ascending order, namely BIF – hematite lutite – Mn ore – hematite lutite – BIF. The BIF underlying the upper Mn ore layer has high and variable carbonate-hosted Ca contents between 2.6 and 18.3 wt.%, indicating the dominance of calcite(+ankerite). This interpretation is confirmed by the low Mg contents (average at 0.3±0.2 1SD wt.%), while the corresponding Fe range (from 0.3 to 3.0 wt.%) is explained by the co-occurrence of lesser ankerite along with the calcite. Manganese concentrations are very low, with a range of 0.2 to 1.3 wt.% and highest values recorded at the top and bottom margins of this layer in contact with adjacent hematite lutite transitions.

Overlying the BIF layer is a transitional hematite lutite *via* a relatively sharp lithological contact. The carbonate fraction here is high in Ca (3.6 – 13.2 wt.%), while Mg is relatively low, with an average value of 0.5±0.1 wt. 1SD %. These values, combined with high Mn ranging from 3.1 to 14.3 wt., % confirm the prevalence of calcic Mn carbonates (Mn calcite and kutnahorite) in this section. Correspondingly very low iron contents (0.1±0.1 1SD wt.%) suggest negligible partitioning of Fe into the structure of these carbonates. A similar situation is observed in the overlying Mn ore layer, which has the highest average carbonate-hosted Ca concentration compared to other Mn ore layers lower in this succession. Specifically, Ca concentrations range between 5.8 wt.% and 18.1 wt.%, while the corresponding Mg range is low, from 0.4 to 0.8 wt.%. Average carbonate-hosted Mn concentration is also comparatively low (6.5±1.3 1SD wt.%), suggesting a relatively lower in Mn and higher in Ca carbonate mineralogy. Like all Mn-rich assemblages in the Hotazel rocks (Mn ore layers and transitional lutites), carbonate-hosted Fe concentrations here remain very low (ca. 0.1 wt.%).

Overlying the upper Mn ore layer is the stratigraphically thickest hematite lutite (ca. 11.5-m), which also has higher carbonate-hosted manganese concentration compared to the underlying Mn ore layer, with a range of 5.5 to 11.8 wt.%. Conversely, the concentration of Ca in the same carbonate fraction is relatively lower, with a range from 2.9 to 9.1 wt.%, while average Mg concentration is very low (0.7±0.2 1SD wt.%). The iron content in the same carbonate fraction is also low, but it shows a modest increase toward the contact with the uppermost BIF layer (0.1 - 2.4 wt.%).

Above the hematite lutite lies the upper Hotazel BIF layer transitioning into the Mooidraai carbonates stratigraphically higher. Carbonate-specific compositional data suggest a generally ankerite-dominated carbonate fraction with a peak in siderite co-abundance between 252.3 and 236.54 m. Carbonate-specific Ca and Fe concentrations are moderate and variable, ranging respectively from 0.2 to 7.6 wt.% and from 0.4 to 6.7 wt.%. By contrast, average manganese concentrations never exceed 0.5±0.1 1SD wt.%, with highest values registered near the contact with the underlying hematite lutite. Concentrations of carbonate-hosted Mg are highest here by comparison to the BIF layers lower in the succession, with a range from 0.1 to 2.2 wt.%. In general, the section with higher modal siderite *versus* ankerite is reflected through relatively higher carbonate-hosted Fe(+Mg) and correspondingly lower Ca contents.

Finally, a broad compositional transition is observed between the Hotazel Formation and the Moodraai Formation at the top of the Hotazel succession, which agrees with a gradual and progressive increase in bulk $\delta^{13}C$ values, as will be addressed in further discussions below. The carbonate-hosted Fe abundance in the transition samples declines relative to the immediately underlying BIF layer – ranging between 1.7 and 2.5 wt.%, with a corresponding increase in average carbonate-hosted Ca of 17.9±0.6 1SD wt.%. These data point to the increasing dominance of modal calcite relative to ankerite/siderite in approaching the contact with the Mooidraai limestone. This observation is further supported by the correspondingly low Mg (0.44±0.07 1SD wt.%) and Mn (0.5±0.1 1SD wt.%) contents.

Carbonate mineral chemistry

The carbonate-specific speciation results presented in the previous section provide important new insights into the chemistry of the carbonate fraction of the Hotazel strata and its variability across stratigraphy, particularly with respect to the partitioning of the redox-sensitive species Fe and Mn.

However, the results represent the bulk carbonate fraction of each sample, which in almost all cases constitutes a mixture of individual carbonate phases at variable modal abundances from one sample to the next. In order to inform our speciation data with compositional characteristics and variabilities for specific carbonate minerals, we include here selected EPMA analytical results from representative samples across the entire Hotazel stratigraphy. The results and associated signatures are based on compositional information for the typical Fe- and Mn-rich carbonates encountered, namely ankerite/siderite and kutnahorite/rhodochrosite, and are summarized in Figure 12. It should be noted that similar results and conclusions can also be drawn through individual calcite grain analyses, but they are not shown here (see supplementary file 5).

As stated in earlier sections, Mn-calcite and kutnahorite (with occasional rhodochrosite) is the dominant mineral pair in the manganiferous sub-sections of the Hotazel succession, namely the three Mn ore layers and adjacent hematite lutite transitions. Stratigraphic compositional results for Fe (as FeO) from single-grain EPMA analyses of kutnahorite (+ rhodochrosite) grains agree very well with those from corresponding carbonate-fraction analyses discussed in the previous section. Specifically, Fe concentrations are consistently very low, with values not exceeding 1wt.% in most instances. Higher Fe concentrations of a few wt.% are seen only very near the contacts between BIF and hematite lutite transitions or at the lower margin of the hematite-rich BIF in the lowermost part of the Hotazel stratigraphy (Fig. 12). An analogous feature is observed in the analytical results for Mn in ankerite (+ siderite) from the Hotazel BIF. Specifically, ankerite (+ siderite) analyses show low and largely invariant Mn concentrations (as MnO) that range between 1 and 2 wt.% across individual samples. These concentrations become marginally higher by an additional 2-3 wt.% near the contacts with hematite lutite.

It follows, therefore, that Fe carbonate minerals in the Fe-rich sub-sections of the Hotazel Formation record consistently high FeO/MnO ratios by virtue of their very low MnO contents, as determined through single grain (EPMA) and species-specific (carbonate fraction) analyses. Conversely, Mn carbonates in transitional lutites and Mn ore layers record very low and invariant concentrations in terms of Fe, which translates into the very high MnO/FeO ratios seen in single mineral grains and total carbonate extracts. This is a key feature in the context of the objectives of this paper, which will be explored in more detail in the discussion that follows.

Stratigraphic variations in carbon and iron isotope data

Figure 13 presents a comprehensive graphical summary of bulk-rock carbonate $\delta^{13}C$ profiles for both drill cores (GL136 and GL137) at a stratigraphic resolution of one sample per meter of core section on average. All raw data are also included in tabulated form in the supplementary file 1. Both profiles illustrate a generally smooth and closely comparable pattern of low variability in $\delta^{13}C$ around the grand average value of -9.7±2.9 ‰ for drill core GL137 and -10.1±2.7 ‰ for drill core GL136. Our $\delta^{13}C$ data also agree well with previously published data for the Hotazel Formation but also with similar data from other BIF occurrences elsewhere, both in terms of the average $\delta^{13}C$ value and the range and frequency of $\delta^{13}C$ values displayed (Tsikos *et al*., 2022; see also Fig. 2). We observe apparent excursions (positive and negative) in bulk $\delta^{13}C$ of a magnitude generally 2-4 ‰ about the above average across the Hotazel stratigraphy, mostly over intervals of sharp lithologic change (*e.g*., BIF to hematite lutite). Arguably the sharpest of such excursions is observed within the uppermost part of the Hotazel succession, where the Hotazel BIF progressively grades into the near-0 ‰ Mooidraai limestone succession (Tsikos *et al.*, 2001). By contrast, the lowest bulk-rock $\delta^{13}C$ values (-10 to -20 ‰) are seen at the stratigraphically lower BIF layers above and below the lower Mn ore layer, also consistent with previous studies (Tsikos *et al.*, 2003; Schneiderhahn *et al.*, 2006).

Bulk-rock Fe isotope results from a selection of samples across the three key lithofacies (BIF, hematite lutite and Mn ore) are shown in Figure 13. The new data have been combined with those from an earlier study that captured primarily the bottom half of the Hotazel stratigraphy from a neighboring drill core intersection at Gloria Manganese Mine (GL26; Tsikos *et al*., 2010). The joining of the two datasets to produce a composite stratigraphic profile of iron isotope data was facilitated by the availability of iron isotope results from both drill cores that straddle the lithologic contact between the uppermost hematite lutite of the middle Fe-Mn-Fe cycle and the immediately overlying BIF. The specific transition is characterized by consistently very low bulk $\delta^{56}Fe$ values (ca. -2.8 ‰) at the upper margin of the hematite lutite, which rise sharply by about 2 ‰ in samples from the overlying BIF. This positive spike in iron isotopes is faithfully recorded in both drill cores.

A striking feature of the iron isotope composition of the Hotazel Formation is the first-order co-variation between bulk-rock Fe contents and $\delta^{56}Fe$ values across stratigraphy, with highest values

recorded in BIF and lowest in the Mn-rich assemblages (see also Supplementary File 6). The relative difference in δ^{56}Fe data varies depending on exact stratigraphic location; for example, the basal Fe-Mn-Fe cycle records a δ^{56}Fe value of -0.21 ‰ for a single hematitic BIF sample (Fig. 13; Tsikos *et al*. 2010), which decreases to a three-sample average δ^{56}Fe value of -2.08±0.21‰ in the overlying lower Mn ore layer and returns to a single δ^{56}Fe value of -0.19 ‰ in the BIF immediately overlying the latter. In the upper Fe-Mn-Fe cycle, corresponding values in the Mn ore layer average -1.9±0.12 ‰ (n=4), decreasing very slightly in the overlying hematite lutite transition (average δ^{56}Fe at -2.1±0.07 ‰, n=3), and then increasing again to a δ^{56}Fe value range between -1 and -2 ‰ in the overlying upper BIF.

Fine-scale carbon and iron isotope variability

Stratigraphic C and Fe isotope results are presented here at what is likely an unprecedented sampling resolution in studies of BIF. Yet, they still cannot provide conclusive constraints on possible variabilities on even finer scales, which may lead to some uncertainty about the conclusions presented. In recognition of that potential pitfall and in keeping with our methodology used for other analyses, we performed bulk δ^{13}C, δ^{56}Fe and Fe/Ca and Mn/Ca determinations on 31 continuous, mm-scale sub-samples from three representative sections of Mn ore, BIF and hematite lutite from drill core GL136. The bulk Fe/Ca and Mn/Ca ratios serve as geochemical records of variations in modal carbonate *versus* oxide/silicate mineralogy in all three samples, as Ca is an element contained exclusively in the carbonate fraction of the rocks, while the primary Fe and Mn hosts are the minerals magnetite in BIF, hematite in the hematite lutite transitions and braunite in the Mn ore layers. The results are included in the supplementary file 4 and comprehensively illustrated in Figure 14.

The key outcome of our fine-scale analytical approach is the generally very small-scale variability for both the C and Fe isotope ratio records, which lends further support to the robustness of our coarser sampling approach across the entire Hotazel stratigraphy. Arguably the sample set that displays the lowest variance in all four of our chosen geochemical parameters is the one from the uppermost hematite lutite. Here, $\delta^{13}C_{carb}$ and bulk-rock δ^{56}Fe data record averages respectively at -2.1±0.04 ‰ and -12.3±0.2 ‰, while corresponding Fe/Ca and Mn/Ca ratio values average 8.2±1.2 ‰ and 4.8±0.4 ‰, respectively (1SD, n=10). The situation is only slightly different in the sample

set from the lower Mn ore layer. For those samples, $\delta^{13}C_{carb}$, $\delta^{56}Fe$ and Mn/Ca ratios also exhibit low overall variability, with respective averages of -10.5±0.4 ‰, -1.7±0.09 ‰ and 3.2±0.5 (1SD, n=8). Here, a stratigraphic trend of potential significance reveals upward decreasing $\delta^{13}C_{carb}$ and increasing $\delta^{56}Fe$ values, which both appear to correspond to an upward increase in the Mn/Ca ratio and hence increasing modal braunite relative to bulk carbonate abundance. Finally, the BIF sample shows highest variability in the average Fe/Ca ratio (6.9±3.5, 1SD, n=13), which points to strongly variable relative modal abundance between its bulk carbonate fraction (calcite+ankerite) and that of magnetite as the dominant Fe-bearing oxide. The respective $\delta^{56}Fe$ values, by contrast, show very low variance at an average of -1.85±0.05 ‰. Despite the relatively low variance for $\delta^{13}C_{carb}$ values as well (-10.4±0.7 ‰), the corresponding profile appears to be a mirror image of the profile for the Fe/Ca ratio, suggesting a broadly antithetic relationship between high modal magnetite and low $\delta^{13}C_{carb}$, and *vice-versa* (see supplementary file 8).

Discussion

One of the most recognisable and well-documented features of the stratigraphy of the Hotazel Formation is the cyclic alternation between BIF and its three Mn ore layers. From a geochemical viewpoint, this cyclicity is best expressed by the stratigraphic variability in bulk-rock manganese content. As illustrated in Fig. 10, bulk-rock Mn oxide abundances are well below 1 wt.% across practically all BIF intervals; manganese contents rise sharply at the onset of each hematite lutite transition, with a peak at the centre of each cycle, and decline again to very low values as the maximum Mn lithofacies gradually give way up section to hematite lutite and ultimately a return to BIF. Standard macroscopic observations further confirm that increasing manganese contents, as recorded at the onset of each cycle, effectively coincide with the sharp contacts between hematite-free BIF and hematite-bearing lutite. The only part of the Hotazel stratigraphy where that relationship is macroscopically obscured is in the basal BIF underlying the lowermost Mn cycle. As mentioned in the earlier introductory sections, the BIF here is hematite-bearing over most of the interval in question and contains relatively elevated — albeit generally low — bulk manganese content (up to 3.5 wt.%, as MnO_2) compared to the rest of the overlying BIF (Lantink *et al*., 2018). It therefore appears to represent a more transitional BIF subfacies, with mineralogical and geochemical signatures akin to hematite lutite *sensu stricto*.

The modulating mechanism that produced the cyclic Hotazel stratigraphy is not well known but has been loosely attributed to sea-level fluctuations in the form of repeated transgression (BIF) - regression (hematite lutite and manganese ore) cycles (Beukes, 1983; Tsikos and Moore, 1997). These cycles would have been superimposed on a chemical sedimentary environment receiving negligible detrital contributions and characterised by either overlapping or decoupled pathways of primary iron and manganese precipitation. Such precipitation would have presumably taken place predominantly (though not necessarily exclusively) in the form of high valence (oxyhydr)oxides of Fe and Mn, in line with proposed models for both metals involving either aerobic oxidation and/or biologically mediated anaerobic oxidation (*e.g.*, photoferrotrophy; Bekker *et al*., 2010; Konhauser *et al*., 2017).

In this palaeodepositional context, however, determining the exact composition of the precursor sediments in the Hotazel strata is an objective that remains elusive. The traditional view is that the primary Hotazel mineralogy must have been dominated by Fe(III) and Mn(IV) (oxyhydr)oxides, the latter prevailing under transiently fully oxic conditions across the entire water column (e.g. Kirshvink *et al*., 2000; Johnson *et al*., 2016). Once deposited, these mineral phases would have been reactive and susceptible to reduction by Fe- and Mn-reducing bacteria below the sediment-water interface, with associated organic carbon acting as the main electron donor. These reductive diagenetic pathways would have delivered increased amounts of soluble Fe(II) and Mn(II) back into pore-fluid, along with low-$\delta^{13}C$ bicarbonate derived from the remineralisation of organic matter, thus resulting in high degrees of mineral saturation and concomitant formation of isotopically light iron and manganese carbonate minerals dominating the sediment matrix (*e.g.*, siderite, rhodochrocite, etc). Incorporation of Ca(II), Mg(II) and DIC into such carbonates would be possible either from the pore-fluid itself or by diagenetic re-constitutions involving (Mg-)calcite precipitates out of the ambient water column. The complete lack of organic carbon preservation and simultaneous retention of much of the iron and manganese in the rocks in the form of modally abundant Fe(III) and Mn(III) minerals (magnetite, hematite, braunite) would also suggest that the process of metal reduction must have been limited by organic carbon availability.

Pathways of carbonate formation and implications

In the discussion that follows we explore the traditional models by revisiting the carbonate-specific geochemical results presented earlier in this paper (see Fig. 11) and specifically by focusing on the upper Fe-Mn-Fe cycle as the most straightforward example of first order cyclicity in the Hotazel stratigraphy. We have opted to display and discuss our results using a total of five key chemo-stratigraphic parameters, namely four bulk carbonate-specific ratios (Fe/Mn, Mn/Fe, Mn/Ca, Fe/Ca) and the corresponding bulk carbonate $\delta^{13}C$ data, all as obtained from drill core section GL137 (Fig. 15). The results of that exercise are summarized in sequential fashion in the sections that follow.

A. Constraints from carbonate chemostratigraphy

The first and probably most salient observation derived from the plots of Fig. 15 is the excellent differentiation between iron- and manganese-rich carbonate mineralogy across the complete cycle. Specifically, the BIF data record very low contents in carbonate-hosted manganese (lowest Mn/Fe ratios), in good agreement with microprobe results presented earlier for ankerite grains from the same stratigraphic intervals (Fig. 12). By stark contrast, the carbonate fractions in the hematite lutite zones and Mn ore layer contain very low abundances of iron (lowest Fe/Mn ratios) irrespective of manganese content.

Classic models of anaerobic diagenesis of Fe and Mn oxides would address such differentiation – at least partly – on thermodynamic grounds. Specifically, it is known from extant suboxic diagenetic environments (Balzer, 1982; Lovley, 1991; Canfield *et al.*, 1993; Canfield *et al.*, 1993a;1993b; Nealson and Staffarini, 1994; Kappler *et al*., 2005; Posth *et al*., 2013) that microbial Mn(IV) reduction is thermodynamically favoured to occur before Fe(III) reduction, and therefore well-mixed sediments enriched in primary Mn(IV) and Fe(III) oxides would likely undergo substantial Mn reduction before Fe reduction commences. To this end, it is worth noting that while many samples from the hematite lutite zones record a bulk-rock Fe/Mn ratio well above 1 (see Fig. 10), iron reduction and incorporation of at least some recycled Fe(II) into the structure of Mn carbonate minerals has evidently not occurred to any measurable degree, as corresponding microprobe data from kutnahorite grains also confirm (Fig. 12).

B. Carbonates in the Hotazel BIF

A combination of carbonate-specific chemistry and carbonate-carbon isotope results from the BIF sections of the upper Fe-Mn-Fe sub-cycle reveals some insight into the postulated anaerobic diagenetic reactions. Samples from the BIF immediately underlying the upper Mn ore layer (Fig. 15, n=7) appear to record a broad anticorrelation between carbonate-specific Fe/Ca ratios and bulk carbonate $\delta^{13}C$. Such anticorrelation is consistent with the biologically mediated diagenetic processes of iron reduction and concomitant organic matter oxidation, commonly referred to as DIR (Dissimilatory Iron Reduction; Walker, 1984; Pecoits *et al.*, 2009; Heimann *et al.*, 2010; Posth *et al.*, 2013). Diagenetic models involving DIR predict the formation of siderite with a carbon isotope signature closely comparable to that of the original organic matter, provided that the system was not limited by organic carbon availability. If diagenetic carbonate formation also incorporates contributions of seawater DIC from either pore-fluids or reworking of isotopically heavy marine calcite, then the value of the bulk carbonate would reflect the variable mixing of the two carbon sources (DIC and recycled organic carbon) during diagenesis. The dominance of sub- to euhedral stoichiometric ankerite and calcite of intermediate $\delta^{13}C$ in the Hotazel BIF suggests that neomorphic carbonate formation must have resulted from diagenetic homogenisation (see also Siahi *et al.*, 2020) of earlier discrete carbonate populations that included a low $\delta^{13}C$ contribution produced *via* DIR. In that case, the anticorrelation between carbonate $\delta^{13}C$ and the carbonate-specific Fe/Ca ratio can be explained by corresponding variability in relative contributions of DIC-*versus* DIR-sourced bicarbonate during diagenetic carbonate formation. Such variability translates mineralogically into variable modal ankerite *versus* calcite, with the former constituting the direct record of iron reduction *via* DIR.

The foregoing interpretation is, nevertheless, not consistently applicable across the entire Hotazel BIF intersection. The BIF overlying the upper Mn ore layer contains substantial modal siderite in addition to ankerite, hence it records both the highest and most variable carbonate-specific Fe/Ca ratios in the Hotazel BIF. Yet, the same interval displays practically invariant $\delta^{13}C$ values, with an average of *ca.* -10 ‰ (n=12) over much of the section before the positive excursion that marks the transition at the contact with the overlying Mooidraai limestone (Fig. 15). The occasional deposition of essentially pure iron carbonate in the Hotazel BIF is therefore not necessarily accompanied by the very low carbonate $\delta^{13}C$ values that would be predicted by the DIR model.

At this point, it is important to re-visit some of the nuances that stem from the highly heterogeneous textural nature of BIF. The conspicuous banding displayed by classic microbanded BIF such as that seen in the Hotazel Formation (see Fig. 1) is typically manifested by essentially monomineralic magnetite laminae intercalated with magnetite-poor, chert-rich bands dominated by carbonate and silicate iron mineralogy carrying only subordinate magnetite. The precursor sediment to BIF must therefore not have been well mixed with respect to iron oxide, unless it is argued that the microbanding that typifies BIF was produced entirely through post-depositional iron remobilisation and reprecipitation in discrete, bedding-parallel reaction fronts. Moreover, the inference of ferrihydrite as the iron oxyhydroxide precursor of choice (Beukes, 1983; Konhauser *et al.*,2005; Johnson *et al.*, 2003, 2008a, 2008b; Tsikos *et al.*, 2010; Kaiswell *et al.*, 2011; Posth *et al.*, 2013; Kurzweil *et al*. 2016) suggests that maximum fluxes of Fe(III) must have characterised the intervals now represented by magnetite-dominated laminae. By contrast, net fluxes of ferrihydrite would have been substantially subdued during deposition of the precursor sediment to the chert-rich bands and/or became diluted by periodically higher rates of contemporaneous silica (+carbonate) precipitation from the water column.

Biological models for the formation of BIF posit that ferrihydrite deposition would have been accompanied by co-precipitation of organic matter associated with the oxidative process, such as cyanobacterial organic matter in the case of aerobic oxidation and/or photoferrotrophic organic matter in the case of anaerobic oxidation. The assumption of a single oxidative pathway for ferric iron deposition (as ferrihydrite) and organic carbon transfer to the primary sediment would suggest a largely congruent mode of precipitation for both chemical species unless processes of differential redox cycling for either were operative in the ambient water column. Magnetite dominated bands, however, would have recorded only partial reduction of ferric iron — as magnetite is a mixed-valence Fe oxide — presumably limited by primary organic carbon availability. In the case of the Fe-poor chert bands, by contrast, Fe(III) reduction must have been effectively complete when forming chiefly Fe(II) carbonates and less so for Fe(II)-dominated silicate mineralogy (*e.g.*, minessotaite, greenalite). The latter assemblages would also imply the occurrence of sufficient initial organic carbon in the sediment to reduce Fe(III) almost quantitatively.

It is important to add here that the highest manganese content in the Hotazel BIF and thus highest presumed primary flux of precursor Mn(IV) to the sediment relative to Fe(III) is associated

exclusively with the carbonate fraction of the rock, which dominates the comparatively Fe-poor chert bands and not the magnetite-rich laminae. This relationship reinforces the notion that each mineralogically distinct set of bands in BIF probably represents a discrete sub-system and should therefore be treated as record of equally distinct processes and effects.

C. Carbonates in hematite lutite

As shown above, the hematite lutite transitions are dominated by hematite as essentially the sole iron oxide phase and record progressively increasing abundances of manganese at the onset of each Fe-Mn-Fe sub-cycle (Fig 10). We shall assume that the hematite here represents the product of diagenetic dehydration of primary ferrihydrite precipitates that did not undergo reduction *via* DIR, while similar precipitates in adjacent BIF must have been quantitatively transformed *via* DIR to the presently observed assemblages. Figure 15 illustrates that the bulk carbonate fraction (Mn calcite + kutnahorite) of the hematite lutite transitions in the upper Mn cycle similarly records a sharp rise in manganese contents at the onset of the cycle, followed by a progressive decline in manganese abundance at the closure of the same cycle atop the stratigraphically higher Mn ore layer. Mineralogically, the occasional presence of rhodochrosite in the Hotazel succession also coincides with those sub-sections of the hematite lutite transitions that record maximum carbonate-specific manganese content (see also Fig. 12).

The observed up-section rise in carbonate-hosted manganese of the hematite lutite below the upper Mn ore layer offers support to diagenetic models of biologically mediated manganese reduction and concomitant organic carbon oxidation, in a fashion analogous to the processes of DIR in BIF. We will hereafter adopt the term Dissimilatory Manganese Reduction (DMR) to refer to such a diagenetic pathway, on the assumption that the primary diagenetic environment of the Hotazel Formation contained a consortium of anaerobic bacteria that could utilize Fe(III) and/or Mn(IV) as electron acceptors for the remineralisation of organic matter. Increasing availability of primary Mn(IV) oxide in the sediment would have fuelled increased production of Mn(II) *via* DMR, which would be faithfully recorded in the progressively higher Mn(II) contents of the carbonate fraction. Conversely, the upward-declining manganese concentration in the carbonate fraction of hematite lutite above the upper Mn ore layer would signal a corresponding decrease in primary Mn(IV) availability in the sediment and thus lower Mn(II) contributions to Mn carbonate formation *via*

DMR. In both instances, however, DIR was evidently – and somewhat surprisingly – not operative, despite the large bulk-rock abundances of ferric iron oxide in the form of hematite (*i.e.,* initial ferrihydrite).

The carbon isotope records across the two hematite lutite intervals of the upper Fe-Mn-Fe cycle provide additional support for the operation of DMR through their general anticorrelation with corresponding Mn/Ca ratio data. That anticorrelation is particularly well illustrated through the mirror-image relationship of the two records for the hematite lutite transition above the Mn ore layer (Fig. 15). Relationships of this kind generally point to the coupled oxidation of organic carbon and reduction of high-valence manganese (or iron) oxides, on the assumption that higher degrees of Mn(IV) reduction would be commensurate with increased rates of organic carbon respiration and thus higher production of low-$\delta^{13}C$ DIC in pore fluids for diagenetic Mn carbonate growth. It follows, therefore, that maximum availability of Mn(IV) in a precursor sediment with sufficient organic matter concentrations should be expected to lead to the formation of diagenetic rhodochrosite ($MnCO_3$), with $\delta^{13}C$ values potentially approaching those of the organic matter implicated in the reductive process.

D. Carbonates in the Mn ore layer

The carbonate-specific results presented in the previous section for the hematite lutite transitions of the upper Fe-Mn-Fe cycle anticipate similar relationships for the upper Mn ore layer. The inference of DMR as the driving mechanism for progressively higher Mn content and lower $\delta^{13}C$ of the carbonate fraction of the rocks suggests that the isotopically lightest Mn-rich carbonate phases should be expected to dominate the part of the Mn ore layer with peak bulk-rock manganese content. Simply, DMR should have led to the diagenetic formation of isotopically lightest, Mn-rich kutnahorite and rhodochrosite in the central part of the upper Mn ore layer, which records maximum concentration of manganese, so long as sufficient organic carbon was available for reaction in the initial sediment. As it will be shown below, however, the opposite is the case.

We should stress again at this point that there is no clear visual expression of a sharp lithological contact between the hematite lutite transitions and the Mn ore layers in the Hotazel succession, owing to the imperceptible change in the colour of the rocks with changing Fe/Mn ratio. The

carbonate-specific geochemical relationships of Figure 15, however, reveal a conspicuously sharp transition between the two lithofacies that is based entirely on geochemistry and could potentially serve as a chemostratigraphic boundary between them. The specific relationship is best illustrated in the Mn/Ca ratio profile, which registers an abrupt decline from values as high as 4 in the hematite lutite underlying the Mn ore layer to as low as 0.3 in the peak Mn zone above. A similar relationship is also recorded in the other two Fe-Mn-Fe cycles lower in the stratigraphy.

The above-mentioned abrupt drop in the carbonate Mn/Ca ratio has not been reported previously from the Mn ore layers of the Hotazel Formation. An average Mn/Ca ratio value of 0.5 at very low variance persists over approximately 8 meters of the upper Mn ore layer and coincides with the interval recording the highest and most economic bulk manganese concentrations, peaking at *ca.* 47 wt% Mn (as MnO_2). Mineralogically, the above features translate into the increasing dominance of the silicate mineral braunite (+ lesser friedelite) at the expense of hematite, as the stratigraphic centre of the Mn ore layer is approached. At the same time, maximum Mn grades are associated with minimum carbonate modal abundance, as illustrated by the lowest LOI values recorded over the same interval. Maximum Mn grades are therefore not associated with maximum manganese content in the carbonate fraction of the rocks nor with higher carbonate abundances but rather with the modal prevalence of braunite over Mn-poor carbonate across the same stratigraphic interval.

We investigated further the mineral chemistry of the carbonate fraction of the upper Mn ore layer to shed additional light on the low and largely invariant bulk carbonate Mn/Ca ratio, acknowledging that its carbonate mineralogy contains combinations of Mn calcite and kutnahorite. We performed high-resolution microprobe analyses for both Mn calcite and kutnahorite on a single but representative polished thin section from the high Mn zone of the upper Mn ore layer. We present the results for measured Mn/Ca ratios in the histograms of Fig. 16. Although single-spot compositional data reveal a range of Mn/Ca values from as low as 0.1 to as high as 2.1, the histograms illustrate a statistically robust bimodal distribution that represents co-existing low-Mn calcite and Ca kutnahorite compositions, with respective average Mn/Ca ratios of *ca*. 0.25 and 1.25. Given that Mn calcite appears to be modally more abundant than Ca kutnahorite, the average bulk carbonate Mn/Ca value of 0.5 across the high Mn zone of the upper Mn ore layer would translate into a corresponding average modal ratio of Mn calcite to Ca kutnahorite of approximately 3:1.

The above results do not readily support processes of Mn carbonate formation *via* diagenetic DMR. In marked contrast with the results from adjacent hematite lutite transitions, the carbonate fraction of the Mn ore layer contains low-Mn calcite and Ca kutnahorite, resulting in a dominantly Ca-rich bulk carbonate fraction. At the same time, the average $\delta^{13}C$ value of the same carbonate fraction is -8.5 ‰ (n=8), that is, only 3-4 ‰ higher than the lowest values recorded by the more manganiferous carbonate fraction in the hematite lutite transitions. When $\delta^{13}C$ data from the entire Mn-rich portion of the upper cycle (*i.e.*, those from the Mn ore layer and adjacent hematite lutite) are plotted against their respective Mn/Ca compositional ratios (Fig. 17), the data define a broadly linear array with a correlation coefficient R^2 of 0.74. Based on this statistical relationship, end-member pure Ca carbonate in the upper Mn ore layer is extrapolated to have an isotopic composition just below the value of -7 ‰, which is inconsistent with both DMR and equilibrium precipitation of marine calcite in ambient seawater with assumed $\delta^{13}C_{DIC}$ at near-zero ‰.

An alternative interpretation that could reconcile diagenetic DMR with our new carbonate-specific and isotopic data involves partial, one-electron step reduction of primary Mn(IV) to Mn(III), followed by saturation with respect to braunite in the presence of sufficient aqueous Si in the pore fluid. That way, formation of diagenetic Mn carbonate would be curtailed in favour of braunite due to the prevalence of the carbonate incompatible Mn(III) in the sediment, while the respired organic carbon would have been accommodated — partly or wholly — into low-Mn calcite and Ca kutnahorite. At the heart of such an argument is the added requirement of insufficient organic carbon availability in the primary sediment, which would have otherwise led to almost complete reduction of Mn(IV) to Mn(II) if more abundant, as it is evidently the case in the adjacent hematite lutite transitions.

To test the idea presented here for partial oxidation of Mn(II) to Mn(III) rather than reduction of Mn(IV) to Mn (III), given the evidence for a strong role played by Mn(III), it is useful to explore quantitatively the high required abundance of primary organic carbon that would be necessary to reduce an original Hotazel-like sediment dominated by Mn(IV) oxides into the overwhelmingly Mn(III)-rich assemblage suggested by our data. For that purpose, we selected four successive samples from the centre of the upper Mn ore layer that record the highest Mn concentrations (all higher than 40 wt.% as MnO_2) and averaged their major element composition and bulk-carbonate $\delta^{13}C$ (Table 1). We assumed for convenience that all of the contained manganese was originally in

the form of MnO_2 and was reduced wholesale to Mn(III) during diagenetic DMR. (In reality, a fraction of the total Mn occurs as Mn(II) in carbonate minerals, as $1/7^{th}$ of the total Mn in the structure of braunite, and as all Mn contained in coexisting friedelite). Finally, we have assumed that our bulk-rock LOI values represent essentially the carbonate-hosted CO_2 fraction of the rocks, given that organic carbon concentrations range from vanishingly low to undetectable, and hydrous minerals in the Mn ore layer are essentially absent. We have also used the average bulk carbonate $\delta^{13}C$ value as record of respired organic carbon contributions to carbonate growth, on the assumption of closed system diagenetic conditions with respect to total carbon, an average $\delta^{13}C$ value for the original organic matter of -28 ‰ and a corresponding $\delta^{13}C$ value for DIC at 0 ‰.

Table 1: Average major element and $\delta^{13}C$ values representing the four highest manganese samples selected from the top Mn ore layer, drill core GL136 (samples: 53-56).

	Fe_2O_3	MnO_2	CaO	MgO	SiO_2	LOI	$\delta^{13}C$
Avg.	15.49	44.57	11.38	3.64	9.43	15.84	-9.41

The results of our exercise demonstrate that the amount of organic carbon that can be deduced from our geochemical results would have been insufficient to have reduced the entire initial Mn(IV) budget of the sediments into Mn(III). The DMR reaction predicts that one mole of organic carbon will reduce 4 moles of MnO_2 into MnOOH as shown by the following reaction:

e.g., $CH_2O + 4MnO_2 + 4H_2O \rightarrow 4MnOOH + HCO_3^- + 4OH^-$

In absolute terms, the total average Mn content (expressed as MnO_2) now present in our chosen subset of samples is 44.6 wt.%, while the total average CO_2 content (expressed as LOI) is 15.8 wt.%. The average carbonate $\delta^{13}C$ value of the four samples with highest Mn content at -9.4 ‰ suggests that approximately one-third of the bulk-rock CO_2 content (*ca*. 5.3 wt.%) would represent the contribution from remineralised organic matter with a $\delta^{13}C$ value of -28 ‰. As that estimated molar organic carbon abundance cannot have reduced more than half (*ca*. 22 wt.%) of the total initial abundance of Mn(IV) (as MnO_2), the only possibility remaining in support of DMR during diagenesis is that the original sediment must have had a TOC content akin to a calcareous, Mn-rich organic mud, which is not supported by the observed assemblages in the Hotazel strata. To

make such a model work, all the contained TOC would have reacted quantitatively with all the initial Mn(IV) oxide, resulting in a largely Mn(III) assemblage while no DIR would have followed the DMR, despite the high concentrations in co-existing hematite (well above 10 wt.% Fe_2O_3 for most analysed samples). Further, more than half of the originally respired organic carbon budget must have leaked out of the sediment under open system conditions, as the rest was sequestered into low-Mn carbonate mineralogy.

Iron isotope evidence for water-column chemical stratification

The bulk-rock iron isotope geochemistry of the Hotazel Formation was discussed comprehensively in a previous paper by Tsikos *et al*. (2010), and the new data presented earlier in this paper are consistent with the earlier results. One of the key outcomes of the study of Tsikos *et al*. (2010) was the generally very low $\delta^{56}Fe$ values recorded in the Hotazel Formation, which were interpreted to have resulted from protracted Rayleigh fractionation effects related to long-term, oxide-dominated BIF deposition in the pre-GOE oceans. The histograms of Figure 18 present a compilation of results for bulk iron isotope analyses of BIF from the Transvaal Supergroup (Mhlanga, 2020; this study; Tsikos *et al*, 2010; Johnson *et al*., 2008a; Thibon *et al*., 2019). A statistically clear difference is recorded between older BIF of the Asbestos Hills Subgroup (highest $\delta^{56}Fe$) and the Hotazel BIF itself (intermediate $\delta^{56}Fe$). The common denominator for the above two datasets is the very similar and essentially hematite-free mineralogical and geochemical composition of the corresponding BIFs. These similarities allow us to deduce that the iron isotope signature of these rocks is likely dominated by reservoir effects through time and not localised effects during post-depositional processes of iron reworking (*e.g.*, diagenesis, aqueous alteration, etc).

The most insightful dataset of Figure 18 is arguably the one representing the hematite- and Mn-rich lithologies of the Hotazel Formation, namely the hematite lutites and Mn ore layers. The range of data registered in these rocks is one of the lowest on record for a BIF (Tsikos *et al*., 2010). Importantly, the dataset represents iron from essentially a single mineral phase — hematite — as the carbonate fraction of the rocks is effectively Fe-free. The assumption that the hematite in the same rocks represents an isotopically conservative product of dehydration of primary ferrihydrite, suggests that water-column oxidation of iron in the Hotazel sediments must have occurred in an isotopically extremely depleted shallow-water reservoir with respect to dissolved $Fe(II)_{aq}$. This is

supported by the well-demonstrated positive fractionation effects during $Fe(II)_{aq}$ oxidation to insoluble Fe(III), whether such oxidation has taken place abiotically or through biological mediation (Anbar and Rouxel, 2007; Johnson *et al*., 2008a; Heimann *et al*., 2010; Busigny *et al*., 2014; Han *et al*., 2022).

In general, our conclusions agree well with the postulated model for protracted Rayleigh-driven depletion in isotopically heavy iron as proposed by Tsikos *et al* (2010). However, Figure 18 also demonstrates that the hematite-free Hotazel BIF interbedded with the Fe(III)+Mn lithofacies is itself statistically heavier in terms of iron isotopes, even though the two subfacies have evidently formed in a common depositional basin. On the working assumption that the Hotazel BIF shares the same ferric precursor with its enclosed Mn-rich hematitic counterparts, we can attribute that isotopic difference to two possible pathways:

- the first pathway would involve formation of magnetite after ferrihydrite in equilibrium with deeper, Fe(II)-rich waters of a heavier iron isotope signature. It is uncertain, however, whether such a pathway would have operated within bottom ferruginous waters or strictly below the sediment-water interface in the presence of $Fe(II)_{aq}$-rich pore fluids derived from such waters;
- the second pathway would suggest that magnetite formation was not related to partial reduction of ferrihydrite but occurred in a decoupled fashion in connection with an isotopically distinct, deep-water $Fe(II)_{aq}$ reservoir.

The implications of these possibilities are likely to have relevance that extends far beyond the Hotazel Formation to the origins of BIF more generally. The common outcome specifically gleaned from our interpretations is that the primary water column of BIF depositional environments must have been stratified with respect to iron isotopes and that the formation of magnetite in BIF may have occurred through pathways that are not necessarily linked to those postulated for primary ferric oxyhydroxide (*e.g.*, ferrihydrite) deposition.

A proposed genetic model for the Hotazel Formation

In this section, we distill our many and diverse observations into a conceptual model (Fig. 19) for the deposition of the three main lithofacies of the Hotazel Formation, namely BIF, hematite lutite

and Mn ore. More specifically, the model is based on findings and interpretations from this study and relevant information from previous research on BIF in general, including the stratigraphically older Kuruman and Griquatown iron formations in the Transvaal Supergroup (Oonk *et al*., 2017; Siahi *et al*, 2020; Tsikos *et al*., 2022). At the core of our model lies the characteristically cyclic nature of the Hotazel Formation hosting three Mn ore layers interlayered with transitional hematite lutite and BIF (Beukes, 1983, Tsikos and Moore, 1997). As mentioned earlier, the cyclic nature of this unique Fe-Mn succession has been attributed to marine transgressive and regressive cycles in a well-stratified basin during deposition (Beukes, 1983; Tsikos and Moore, 1997), although Beukes (1983) has also proposed periodic hydrothermal plume activity ejecting Mn(II) and Fe(II) in discrete pulses in a dynamic circulating ocean. Although hydrothermal models provide a plausible explanation at least for the source of metals, our focus here is on the depositional mechanism and effective separation between Fe and Mn in producing the Hotazel succession. The transgression-regression model above seems to be applicable in view of predicted models for the Paleoproterozoic oceans, which are thought to have been well-stratified, with clear separation of anoxic, suboxic, oxic and sulphidic layers (e.g., Anbar and Knoll, 2002; Planavsky *et al*., 2009; Kendall *et al*., 2012; summarized in Lyons *et al*., 2014).

Recent suggestions for the possible onset of oxygen production at approximately 2.5Ga are regarded as fundamental precondition for the conceptual modelling of the Hotazel paleoenvironment (Brüske *et al*., 2020) to explain the extensive oxidation and subsequent reduction of both Fe and Mn. The source of Fe(II) and Mn(II) would have been through hydrothermal activity (Beukes, 1983; Isley, 1995; Isley and Abbott, 1999), which enriched the anoxic ocean of the time with $Fe(II)_{aq}$ and $Mn(II)_{aq}$. The source of silica could likewise be attributed to hydrothermal venting (Fischer and Knoll, 2009). Both Fe(II) and Mn(II) would have been oxidized within the partially oxic shallow parts of the seawater column through reaction with cyanobacterially produced O_2.

We argued in earlier sections that at the core of the strikingly interlayered nature of the Hotazel Formation must lie a set of primary depositional processes that resulted in the clear decoupling of iron from manganese deposition. We envision that stratification of the water column with respect to both Fe and Mn must be an assumption of paramount importance in terms of palaeodepositional modelling. Tsikos *et al*. (2010) previously proposed that sustained deposition of Mn-poor BIF

during pre-Hotazel times is likely to have led to the enrichment of dissolved manganese relative to iron in the ocean. This assertion is corroborated by the unusually elevated concentrations of Mn recorded in the upper stratigraphic half of the Griquatown iron formation at the top of the underlying Asbestos Hills Subgroup in the Transvaal Supergroup (Siahi *et al*., 2020).

Nevertheless, such enrichment is not in itself sufficient to explain every aspect of the genesis of the Hotazel Formation. The second requirement of our conceptual model is the first-ever suggestion of one-step oxidation of manganese to soluble $Mn(III)_{aq}$ and ultimately to a solid Mn(III) oxyhydroxide precursor – such as any of the MnOOH polymorphs (*e.g.*, manganite) – under saturated conditions (Namgung *et al*., 2018). Contrary to Mn(IV), the main advantage that Mn(III) offers lies with its role as a powerful dissolved oxidant within stratified basins characterized by bottom water anoxia, as is observed today (Trouwborst *et al*., 2006; Madison *et al*., 2013). Generation of aqueous Mn(III) would have introduced a new key redox player in the pre-GOE marine environment, contributing to the development of redox pathways within the water column (Canfield *et al*., 2005) that collectively drove oxidation of Mn and Fe and the cycling of reduced C compounds such as organic matter and possibly methane. Redox cycling is therefore not exclusively confined to processes occurring below the sediment-water interface as critically discussed in earlier parts of our discussion. Pathways of carbonate formation are transferred largely to the water column, in analogous fashion to recent experimental work simulating aqueous ferrous mineral formation through biogenic Fe(III) reduction (Schad *et al*., 2022). Accordingly, the low $\delta^{13}C$ signatures of at least the iron carbonate minerals are best explained *via* disequilibrium fractionation effects under variable degrees of siderite (super)saturation in the water column (Jiang *et al*., 2022; Tsikos et al., 2022), although such an interpretation must remain tentative with respect to the Mn carbonates which have yet to be explored experimentally.

Our model is partitioned into three parts. Each part accounts for the deposition of a major lithofacies present in the Hotazel succession (BIF, hematite lutite, Mn ore), and collectively all three parts can be merged to account for the temporal pattern of threefold cyclic deposition of the Hotazel strata. The model incorporates first-order mineralogical and geochemical trends as highlighted earlier in this study and could be modified in the future as new information on the Hotazel rocks continues to emerge.

A. Deposition of BIF and water-column DIR.

The first stage of the model accounts for BIF deposition, which would represent a relatively deeper (transgressive) stage in terms of sea level during which primary precipitation is taking place at the redoxcline under anoxic conditions (Fig. 19A). The water column must have been well-stratified in terms of aqueous Fe(II) and Mn(II), with a decline in the aqueous Fe/Mn ratio and increase in pO_2 with decreasing water depth. Oxidation of Mn(II) to aqueous Mn(III), is thought to have driven oxidation of Fe(II) to $Fe(OH)_3$ and effective recycling of $Mn(III)_{aq}$ back into the water column as $Mn(II)_{aq}$ (*i.e.*, a Mn-Fe shuttle). This Mn shuttle would have resulted in the development of a redoxcline zone marked by maximum $Mn(II)_{aq}$ concentrations accompanied by minimum $Fe(II)_{aq}$ concentrations.

Below the Mn shuttle, net primary nucleation and settling of $Fe(OH)_3$ would have taken place. Oxidation of sinking organic particles by the generated $Fe(OH)_3$ would have occurred during water-column DIR, producing primary precursors of iron carbonate (*i.e.*, ankerite and siderite). Periodically high rates of iron oxidation and ferrihydrite formation combined with low rates of water-column DIR would have led to net deposition of ferric iron as either primary or early diagenetic magnetite in equilibrium with bottom Fe(II)-rich waters. Conversely, subdued rates of ferrihydrite formation and increased Fe(II) and organic carbon cycling *via* water-column DIR would have led to the carbonate + silicate-dominated assemblages as precursors to the magnetite-poor chert bands. The resultant mineralogy of the BIF facies would record net depositional processes and mineral nucleation effects that characterized the seawater parcel at and below the postulated Mn shuttle. The present textural manifestation of the mineralogy would therefore reflect mainly recrystallisation effects without necessarily major changes in primary chemical and isotopic signals.

B. Hematite lutite deposition and the role of water-column DMR

We propose that deposition of the precursor sediment to the transitional hematite lutite would have been initiated during regressive cycles and thus shallower water depths (Fig. 19B). The key factor of this stage compared to the BIF one is the transient elimination of a deep and vertically extensive aqueous reservoir of Fe(II). Reductive recycling of Mn(III) to Mn(II) would have been curtailed

by the dwindling availability of aqueous Fe(II), rendering $Mn(III)_{aq}$ (and possibly some solid MnOOH too) as the dominant electron acceptor for organic carbon oxidation at the chemocline. This is the stage during which water-column DMR is thought to have become the prevailing pathway of organic carbon recycling relative to DIR, leading to the formation of primary calcic carbonate species that record increased Mn(II) uptake with decreasing water depth. The Mn carbonate precursors for the Mn-calcite and kutnahorite are therefore thought to have precipitated from zones of DMR in a manner similar to that of Mn carbonate formation in the water column of redox-stratified Green Lake in Fayetteville, New York (Herndon *et al*., 2018). The $\delta^{56}Fe$ values for co-existing hematite would be low and reflective of the light residual Fe(II) pool, due to extended removal of isotopically heavy Fe(III) during ferric oxyhydroxide precipitation and attendant iron isotope fractionation through time. Although such reservoir effects have been argued to have characterized the global pre-GOE marine iron pool (Rouxel et al., 2005), we cannot discount the possibility of local basin restriction to have controlled iron isotope fractionations during BIF deposition in the Transvaal basin (see Figure 18).

C. Manganese ore deposition and aerobic organic carbon oxidation.

The third stage involves the precipitation of the Mn ore layers at even shallower depths (maximum regression) where conditions were arguably the most oxic (Fig. 19C). In this environment, the overwhelming redox pathway would have been the oxidation of manganese to a solid Mn(III) precursor by O_2, consistent with experimental studies (Murray *et al*., 1985) and accompanied by only subordinate iron oxidation. Unlike the situation in the hematite lutite stage, we envision that the shallowest waters would have become much enriched in soluble Mn(III) relative to Mn(II) and thus supersaturated with respect to MnOOH. Net precipitation of solid Mn(III) oxyhydroxide would thus become the dominant pathway of Mn sequestration, leading to abundant braunite (+ friedelite) formation probably during (early) diagenetic re-equilibration of MnOOH with dissolved silica in pore fluids. Limited reduced Mn(II) deposition would be reflected in the correspondingly subdued uptake of Mn(II) during water-column calcic carbonate formation, coupled to the low partitioning of Mn(II) in the Mn silicate (mainly braunite) fraction. In view of the declining abundance of dissolved aqueous Mn(III) relative to MnOOH, we assert that the key oxidant for

organic carbon remineralization would now have become the O_2 that would have also oxidized Mn(II) to Mn(III).

Conclusions and implications for the GOE

In this paper, we revisit the Palaeoproterozoic Hotazel Fe-Mn Formation as a critical window to the evolution of marine redox conditions, processes and progressions at the onset of the GOE. Recognizing the challenge in reconstructing primary sediment mineralogy from the complex mineral assemblages that characterise the rocks today, we employed a high-resolution approach emphasizing a variety of bulk-rock and mineral-specific geochemical tools (*i.e.*, major/minor element analyses combined with carbonate-carbon and iron isotope data). For the first time, we targeted the carbonate fraction of the rocks as a mineral fraction that can provide particularly useful insights into the relative role of diagenesis *versus* primary mineral-forming processes toward the development of the presently observed mineralogical compositions.

Arguably the main outcome of our work relates to our carbonate-specific results assessed in the context of the well-established bulk-rock geochemical signatures of the Hotazel strata. In bulk-rock terms, the composition of the Hotazel rocks reveals clear fractionation between iron and manganese across the corresponding endmember lithotypes, namely BIF and Mn ore layers. While the BIF layers are impoverished in manganese, bulk-rock concentrations of Mn rise sharply across the contacts between BIF and the hematite lutite transitions, ultimately leading to peak abundances in the Mn ore layers. The corresponding carbonate-fraction results faithfully record the sharp rise in manganese content across the BIF-hematite lutite contacts. Additional insight linked to the carbonate-specific results concerns the Mn ore layers, which appear to record Mn-poor, low-$\delta^{13}C$, Ca-rich carbonate mineralogy in coexistence with braunite-dominated assemblages at peak bulk manganese oxide contents. This feature is in marked contrast to what diagenetic models of organic carbon remineralisation by Mn(IV) oxides would typically predict, namely carbonate minerals with maximum uptake in recycled Mn(II).

The above results led us to a critical reconsideration of the role of diagenetic organic matter oxidation and Fe/Mn reduction in delivering the Hotazel carbonate assemblages, as favoured in many previously published models. In doing so, we consider an alternative pathway: primary

water-column processes of Fe- and Mn-carbonate mineral formation as highlighted in recent literature (Siahi *et al*., 2020; Wittkop *et al*., 2020; Jiang *et al*., 2022; Tsikos *et al*., 2022). Although we observed localised trends and relationships between our compositional and carbon isotope data of the types used in previous arguments for diagenetic DIR and DMR, the results are not sufficiently consistent across the entire stratigraphy to fully support those anaerobic diagenetic models for isotopically light carbonate formation. Instead, we propose a stratified water-column model that implicates for the first time aerobic oxidation of Mn(II) to Mn(III) as a central factor in processes of redox cycling and associated primary mineral formation *en route* to the GOE.

Our model contains key new elements that should stimulate discussion around the nature, causes and consequences of the GOE. Our principal assertion is that the production of photosynthetic O_2 and oxidation of Mn(II) to soluble Mn(III) were central requirements for the cyclic deposition of Fe and Mn in the Hotazel succession. We consider this Mn redox transition as being pivotal in the context of the GOE. We note the high manganese contents in the upper part of the older Griquatown iron formation, which are reflected in the unusually high values (up to 8 wt.%) of contained Mn(II) in coexisting siderite and ankerite (Siahi *et al*., 2020). The same carbonate minerals in Hotazel BIF rarely exceed 1.5 wt.% Mn content, unless they are in very close proximity to hematite-lutite transitions. We find it challenging to address these disparate features of manganese distribution and mineral partitioning by invoking fully comparable palaeo-environments of deposition for the two iron formations, and instead consider oxidation of Mn(II) to Mn(III) in the Hotazel paleobasin as its single most important distinguishing attribute in terms of evolving manganese redox pathways leading up to the GOE. Conversely, we consider the apparent enrichment of Mn(II) in the Griquatown paleobasin as a result of passive progressive build-up in seawater $Mn(II)_{aq}$ either locally or ocean-wide following protracted, Mn-poor BIF deposition (Rouxel *et al*., 2005; Tsikos *et al*., 2010). Primary carbonate mineral formation in the form of Mn-bearing high-Mg calcite – subsequently replaced by ankerite and siderite – would have recorded that enriched signature in a geochemically conservative fashion in the absence of Mn(II) oxidation (Siahi *et al*., 2020).

Our interpretations therefore place increased emphasis on $Mn(III)_{aq}$ as an important electron acceptor at the dawn of the GOE for aqueous Fe(II) oxidation, leading to strongly stratified BIF basins and development of Mn-rich shallow waters, as we envision through the postulated Mn

shuttle. Under such a dynamic stratified depositional environment, factors such as seawater transgression and regression can potentially modulate the periodic variability in sedimentary facies – and thus lead to effective fractionation between precipitated iron and manganese – in response to temporal variability in redox conditions across the water column. Figure 20 illustrates how the transition from BIF to Mn ore through hematite lutite in an Fe-Mn-Fe cycle can track an inferred primary redox transition. Across such a transition, corresponding electron acceptors (*i.e.*, Fe(III), Mn(III) and O_2) are successively implicated in water-column remineralisation of organic carbon by processes of DIR, DMR and aerobic oxidation, respectively, in a thermodynamically predictable fashion during an inferred sea-level drop. That apparent "redox ladder" is faithfully recorded in the mineralogy and bulk oxidation state of the rocks as expressed in iron and manganese speciation and repeats itself in reverse at the end of the same cycle stratigraphically higher, during a postulated transgressive stage of sea-level change (Fig. 20).

It remains unknown whether Mn oxidation to Mn(IV) was at all possible during the GOE, but we have found no compelling evidence for its primary operation during deposition of the Hotazel Formation. More broadly, these data provide critical insights into the spatiotemporal fabric of redox conditions at the onset of the GOE. Our overarching goal is to place Mn(III) and its implications into the conversation as an important player in the redox dynamics of the Palaeoproterozoic ocean, by acting as key electron acceptor for the oxidation of at least Fe(II) and organic carbon in seawater, in ways similar to those for water-column, microbial Fe(III) and carbon cycling seen in the modern oceans and as simulated through experiments (Schad *et al*., 2022).

Acknowledgements

X.R. Mhlanga and H. Tsikos acknowledge generous funding by ASSMANG Ltd for the establishment of research unit PRIMOR at Rhodes University between 2014-23. B. Ruziwe from ASSMANG Ltd (Black Rock) is thanked for providing unconstrained access to the two drill cores used in this study. X.R. Mhlanga acknowledges the kind assistance and contribution of S. Bates towards the carbonate speciation analyses at UCR. T.W. Lyons acknowledges financial support from Rhodes University through the Hugh Kelly Visiting Fellowship (2014). Lyons also acknowledges support from the NSF-EAR FESD Program, NASA Astrobiology Institute under

Cooperative Agreement No. NNA15BB03A issued through the Science Mission Directorate and the NASA Interdisciplinary Consortia for Astrobiology Research (ICAR) Program.

References

Anbar, A.D., Duan, Y., Lyons, T.W., Arnold, G.L., Kendall, B., Creaser, R.A., Kaufman, A.J., Gordon, G.W., Scott, C., Garvin, J. and Buick, R., 2007. A whiff of oxygen before the great oxidation event? Science, 317(5846), 1903-1906. DOI: 10.1126/science.1140325

Anbar, A.D. and Knoll, A.H., 2002. Proterozoic ocean chemistry and evolution: a bioinorganic bridge?. science, 297(5584), pp.1137-1142. DOI: 10.1126/science.1069651

Altermann, W. and Nelson, D.R., 1998. Sedimentation rates, basin analysis and regional correlations of three Neoarchaean and Palaeoproterozoic sub-basins of the Kaapvaal craton as inferred from precise U–Pb zircon ages from volcaniclastic sediments. Sediment. Geol., 120(1-4), pp.225-256. https://doi.org/10.1016/S0037-0738(98)00034-7

Anbar, A.D. and Rouxel, O., 2007. Metal stable isotopes in paleoceanography. Annu Rev Earth Planet Sci, 35, 717–746. https://doi.org/10.1146/annurev.earth.34.031405.125029

Balzer, W., 1982. On the distribution of iron and manganese at the sediment/water interface: thermodynamic versus kinetic control. Geochim. Cosmochim. Acta, 46(7), 1153-1161. https://doi.org/10.1016/0016-7037(82)90001-1

Bau, M., Romer, R.L., Lüders, V. and Beukes, N.J., 1999. Pb, O, and C isotopes in silicified Mooidraai dolomite (Transvaal Supergroup, South Africa): implications for the composition of Paleoproterozoic seawater and 'dating the increase of oxygen in the Precambrian atmosphere. Earth Planet. Sci. Lett., *174*(1-2), pp.43-57. https://doi.org/10.1016/S0012-821X(99)00261-7

Bau, M. and Dulski, P., 1996. Distribution of yttrium and rare-earth elements in the Penge and Kuruman iron-formations, Transvaal Supergroup, South Africa. Precambrian Res, 79(1-2), 37-55. https://doi.org/10.1016/0301-9268(95)00087-9

Baur, M.E., Hayes, J.M., Studley, S.A. and Walter, M.R., 1985. Millimeter-scale variations of stable isotope abundances in carbonates from Banded Iron Formations in the Hamersley Group of Western Australia. Econ Geol 80, 270–282. https://doi.org/10.2113/gsecongeo.80.2.270

Bekker, A., Krapez, B., Slack, J.F., Planavsky, N., Hofmann, A., Konhauser, K.O. and Rouxel, O.J., 2012. Iron Formation: The Sedimentary Product of a Complex Interplay among Mantle, Tectonic, Oceanic, and Biospheric Processes-a Reply. Econ Geol, 107(2), 379-380. https://doi.org/10.2113/econgeo.107.2.379

Bekker, A., Slack, J.F., Planavsky, N., Krapez, B., Hofmann, A., Konhauser, K.O. and Rouxel, O.J., 2010. Iron formation: the sedimentary product of a complex interplay among mantle, tectonic, oceanic, and biospheric processes. Econ Geol, 105(3), 467-508. https://doi.org/10.2113/gsecongeo.105.3.467

Beukes, N.J., 1983. Palaeoenvironmental setting of Iron-Formations in the depositional basin of the Transvaal Supergroup, South Africa. Developments in Precambrian Geology, 6, 131-198. https://doi.org/10.1016/S0166-2635(08)70073-4

Beukes, N.J. and Gutzmer, J., 2008. Origin and paleoenvironmental significance of major Iron Formations at the Archean-Paleoproterozoic boundary. Society of Economic Geologists Reviews, 15, 5–47. https://doi.org/10.5382/Rev.15.01

Beukes, N.J. and Klein, C., 1990. Geochemistry and sedimentology of a facies transition — from microbanded to Granular Iron-Formation — in the early Proterozoic Transvaal Supergroup, South Africa. Precambrian Res, 47(1-2), 99–139. https://doi.org/10.1016/0301-9268(90)90033-M

Beukes, N.J. and Smit, C.A., 1987. New evidence for thrust faulting of Transvaal strata in Griqualand West: nature of the thrusts and geological implications with special reference to the age of red beds and paleo-oxidation profiles in the area. South Afr J Geol, 90, 304-378.

Brüske, A., Martin, A.N., Rammensee, P., Eroglu, S., Lazarov, M., Albut, G., Schuth, S., Aulbach, S., Schoenberg, R., Beukes, N. and Hofmann, A., 2020. The onset of oxidative weathering traced by uranium isotopes. Precambrian Res, 338, 105583. https://doi.org/10.1016/j.precamres.2019.105583

Busigny, V., Planavsky, N.J., Jézéquel, D., Crowe, S., Louvat, P., Moureau, J., Viollier, E. and Lyons, T.W., 2014. Iron isotopes in an Archean ocean analogue. Geochim. Cosmochim. Acta, 133, 443–462. https://doi.org/10.1016/j.gca.2014.03.004

Cairncross, B. and Beukes, N.J., 2013. The Kalahari Manganese Field, the adventure continues. Struik Nature, Cape Town.

Cairncross, B., Beukes, N.J. and Gutzmer, J., 1997. The manganese adventure: The South African manganese fields. Associated Ore & Metal Corporation Limited.

Canfield, D.E., Jorgensen, B.B., Fossing, H., Glud, R., Gundersen, J., Ramsing, N.B., Thamdrup, B., Hansen, J.W., Nielsen, L.P. and Hall, P.O J., 1993. Pathways of Organic-Carbon Oxidation in 3 Continental-Margin Sediments. Mar. Geol., 113, 27–40. https://doi.org/10.1016/0025-3227(93)90147-N

Canfield, D.E., Kristensen, E. and Thamdrup, B., 2005. Aquatic Geomicrobiology, in: Advance Marine Biology, edited by Southward, A.J., Tyler, P.A., Young, C.M., and Fuiman, L.A. Elsevier, San Diego, 640.

Canfield, D.E., 1993. Organic matter oxidation in marine sediments. In: Interactions of C, N, P and S biogeochemical Cycles and Global Change. Springer Berlin Heidelberg, 333-363.

Canfield, D.E., 1998. A new model for Proterozoic ocean chemistry. Nature, 396(6710), 450. https://doi.org/10.1038/24839

Canfield, D.E., Thamdrup, B. and Hansen, J.W., 1993. The anaerobic degradation of organic matter in Danish coastal sediments: Iron reduction, manganese reduction, and sulfate reduction. Geochim. Cosmochim. Acta, 57(16), 3867–3883. https://doi.org/10.1016/0016-7037(93)90340-3

Cornell, D.H. and Schütte, S.S., 1995. A volcanic-exhalative origin for the world's largest (Kalahari) manganese field. Miner. Depos., 30(2), 146-151. https://doi.org/10.1007/BF00189343

Cornell, D.H., Schütte, S.S. and Eglington, B.L., 1996. The Ongeluk basaltic andesite formation in Griqualand West, South Africa: submarine alteration in a 2222 Ma Proterozoic sea. Precambrian Res, 79(1-2), 101-123. https://doi.org/10.1016/0301-9268(95)00090-9

Craddock, P.R. and Dauphas, N., 2011. Iron and carbon isotope evidence for microbial iron respiration throughout the Archean. Earth Planet. Sci. Lett., 303, 121–132. https://doi.org/10.1016/j.epsl.2010.12.045

Dodd, M.S., Papineau, D., Pirajno, F., Wan, Y. and Karhu, J.A., 2019. Minimal biomass deposition in banded iron formations inferred from organic matter and clay relationships. Nat. Commun., 10(1), 1-13. https://doi.org/10.1038/s41467-019-12975-z

Fairey, B., Tsikos, H., Corfu, F. and Polteau, S., 2013. U–Pb systematics of the Postmasburg Group, Transvaal Supergroup, South Africa: Primary *versus* metasomatic controls. Precambrian Res. 231, 194–205. https://doi.org/10.1016/j.precamres.2013.03.010

Gumsley, A.P., Chamberlain, K.R., Bleeker, W., Söderlund, U., de Kock, M.O., Larsson, E.R. and Bekker, A., 2017. Timing and tempo of the Great Oxidation Event. PROC. NATL. ACAD. SCI. U.S.A, 114(8), 1811-1816. https://doi.org/10.1073/pnas.1608824114

Gutzmer, J. and Beukes, N.J., 1995. Fault-controlled metasomatic alteration of early Proterozoic sedimentary manganese ores in the Kalahari manganese field, South Africa. Econ Geol, 90(4), 823-844. https://doi.org/10.2113/gsecongeo.90.4.823

Gutzmer, J. and Beukes, N.J., 1996a. Karst-hosted, fresh-water Paleoproterozoic manganese deposits, Postmasburg, South Africa. Econ Geol. 91, 1435–1454. https://doi.org/10.2113/gsecongeo.91.8.1435

Gutzmer, J. and Beukes, N.J., 1996b. Mineral paragenesis of the Kalahari Manganese field, South Africa. Ore Geol. Rev., 11(6), 405–428. https://doi.org/10.1016/S0169-1368(96)00011-X

Han, X., He, Y., Li, J., Kappler, A. and Pan, Y., 2022. Iron isotope fractionation in anoxygenic phototrophic Fe(II) oxidation by Rhodobacter ferrooxidans SW2. Geochim. Cosmochim. Acta, https://doi.org/10.1016/j.gca.2022.06.034.

Heimann, A., Johnson, C.M., Beard, B.L., Valley, J.W., Roden, E.E., Spicuzza, M.J. and Beukes, N.J., 2010. Fe, C, and O isotope compositions of Banded Iron Formation carbonates demonstrate a major role for dissimilatory iron reduction in ~2.5Ga marine environments. Earth Planet. Sci. Lett., 294(1-2), 8–18. https://doi.org/10.1016/j.epsl.2010.02.015

Herndon, E.M., Havig, J.R., Singer, D.M., McCormick, M.L. and Kump, L.R., 2018. Manganese and iron geochemistry in sediments underlying the redox-stratified Fayetteville Green Lake. Geochim. Cosmochim. Acta, 231, 50-63. https://doi.org/10.1016/j.gca.2018.04.013

Jelavić, S., Mitchell, A. and Sand, K., 2020. Fate of organic compounds during transformation of ferrihydrite in iron formations. Geochem Perspect Lett, 15, 25-29. https://doi.org/10.31223/osf.io/pd73x

Jiang, C.Z., Halevy I., and Tosca N.J. 2022. Kinetic isotope effect in siderite growth: Implications for the origin of banded iron formation siderite. Geochim. Cosmochim. Acta, 322, 260-273. https://doi.org/10.1016/j.gca.2022.01.029

Johnson, C.M., Beard, B.L., Beukes, N.J., Klein, C. and O'Leary, J.M., 2003. Ancient geochemical cycling in the Earth as inferred from Fe isotope studies of Banded Iron Formations from the Transvaal Craton. Contrib. to Mineral. Petrol., 144(5), 523–547. https://doi.org/10.1007/s00410-002-0418-x

Johnson, C.M., Beard, B.L. and Ohmoto, H., 2005. Biogeochemical cycling of iron in the Archean-Paleoproterozoic Earth: Constraints from iron isotope variations in sedimentary rocks from the Kaapvaal and Pilbara Cratons. Chem. Geol., 218(1-2), 135–169.

Johnson, C.M., Beard, B.L. and Roden, E.E., 2008a. The Iron Isotope Fingerprints of Redox and Biogeochemical Cycling in Modern and Ancient Earth. Annu Rev Earth Planet Sci, 36(1), 457–493. https://doi.org/10.1146/annurev.earth.36.031207.124139

Johnson, C.M., Beard, B.L., Klein, C., Beukes, N.J. and Roden, E.E., 2008b. Iron isotopes constrain biologic and abiologic processes in Banded Iron Formation genesis. Geochim. Cosmochim. Acta, 72(1), 151-169. https://doi.org/10.1016/j.gca.2007.10.013

Johnson, C.M., Ludois, J.M., Beard, B.L., Beukes, N.J. and Heimann, A., 2013a. Iron Formation carbonates: Paleoceanographic proxy or recorder of microbial diagenesis? Geology, 41(11), 1147–1150. https://doi.org/10.1130/G34698.1

Johnson, J.E., Webb, S.M., Thomas, K., Ono, S., Kirschvink, J.L., Fischer, W.W. (2013b) Manganese-oxidizing photosynthesis before the rise of cyanobacteria. Proceedings of the National

Academy of Sciences of the United States of America 110, 11238-11243. https://doi.org/10.1073/pnas.13055301

Johnson, J.E., Webb, S.M., Ma, C. and Fischer, W.W., 2016. Manganese mineralogy and diagenesis in the sedimentary rock record. Geochim. Cosmochim. Acta, 173, 210-231. https://doi.org/10.1016/j.gca.2015.10.027

Kappler, A., Pasquero, C., Konhauser, K.O. and Newman, D.K., 2005. Deposition of Banded Iron Formations by anoxygenic phototrophic Fe (II)-oxidizing bacteria. Geology, 33(11) 865-868. https://doi.org/10.1130/G21658.1

Kirschvink, J.L., Gaidos, E.J., Bertani, L.E., Beukes, N.J., Gutzmer, J., Maepa, L.N. and Steinberger, R.E., 2000. Paleoproterozoic snowball Earth: Extreme climatic and geochemical global change and its biological consequences. PROC. NATL. ACAD. SCI. U.S.A, 97(4), 1400-1405. https://doi.org/10.1073/pnas.97.4.1400

Klein, C. and Beukes, N.J., 1989. Geochemistry and sedimentology of a facies transition from limestone to iron-formation deposition in the early Proterozoic Transvaal Supergroup, South Africa. Econ Geol, 84(7), 1733-1774. https://doi.org/10.2113/gsecongeo.84.7.1733

Kleyenstuber, A.S.E., 1984. The mineralogy of the manganese- bearing Hotazel Formation, of the Proterozoic Transvaal Sequence in Griqualand West, South Africa. Transactions, Geological Society of South Africa, 87, 257-272. https://hdl.handle.net/10520/EJC-1159ba48ab

Kleyenstuber, A.S.E., 1993. Some significant characteristics of the manganese ores and some of the minerals occurring in the Proterozoic Kalahari Manganese Field, South Africa. Resource Geology, 17, 2-11.

Konhauser, K.O., Newman, D.K. and Kappler, A., 2005. The potential significance of microbial Fe (III) reduction during deposition of Precambrian banded iron formations. Geobiology, 3(3), pp.167-177. https://doi.org/10.1111/j.1472-4669.2005.00055.x

Konhauser, K.O., Planavsky, N.J., Hardisty, D.S., Robbins, L.J., Warchola, T.J., Haugaard, R., Lalonde, S.V., Partin, C.A., Oonk, P.B.H., Tsikos, H. and Lyons, T.W., 2017. Iron formations: A global record of Neoarchaean to Palaeoproterozoic environmental history. Earth Science Reviews, 172, 140-177. https://doi.org/10.1016/j.earscirev.2017.06.012

Kunzmann, M., Gutzmer, J., Beukes, N.J. and Halverson, G.P., 2014. Depositional environment and lithostratigraphy of the Paleoproterozoic Mooidraai Formation, Kalahari manganese field, South Africa. South Afr. J Geol, 117(2), 173-192. https://doi.org/10.2113/gssajg.117.2.173

Kurzweil, F., Wille, M., Gantert, N., Beukes, N.J. and Schoenberg, R., 2016. Manganese oxide shuttling in pre-GOE oceans–evidence from molybdenum and iron isotopes. Earth Planet. Sci. Lett., 452, 69-78. https://doi.org/10.1016/j.epsl.2016.07.013

Lantink, M.L., Oonk, P.B., Floor, G.H., Tsikos, H. and Mason, P.R., 2018. Fe isotopes of a 2.4 Ga hematite-rich IF constrain marine redox conditions around the GOE. Precambrian Res, 305, 218-235. https://doi.org/10.1016/j.precamres.2017.12.025

Lovley, D.R., 1991. Dissimilatory Fe (III) and Mn (IV) Reduction. Microbiol. Rev., 55, 259–287. https://doi.org/10.1128/mr.55.2.259-287.1991

Lovley, D.R., Phillips, E.J.P. (1988). Novel Mode of Microbial Energy-Metabolism - Organic-Carbon Oxidation Coupled to Dissimilatory Reduction of Iron or Manganese. Microbiol. Rev., 54(6), 1472–1480. https://doi.org/10.1128/aem.54.6.1472-1480.1988

Lyons, T.W., Reinhard, C.T. and Planavsky, N.J., 2014. The rise of oxygen in Earth's early ocean and atmosphere. Nature, 506(7488), 307-315. https://doi.org/10.1038/nature13068

Madison, A.S., Tebo, B.M., Mucci, A., Sundby, B. and Luther, G.W., 2013. Abundant porewater Mn (III) is a major component of the sedimentary redox system. Science, 341(6148), 875-878. DOI: 10.1126/science.1241326

Maynard, J.B. (2010). The Chemistry of Manganese Ores through Time: A Signal of Increasing Diversity of Earth-Surface Environments. Econ Geol, 105(3), 535-552. https://doi.org/10.2113/gsecongeo.105.3.535

Mhlanga, X.R., 2020. A reappraisal of the origin of the Hotazel iron-manganese Formation in an evolving early Earth system, through the application of mineral-specific geochemistry, speciation techniques and stable isotope systematics. *Unpublished PhD thesis*, Rhodes University, 161p. http://hdl.handle.net/10962/146123

Oonk, P.B.H., 2017. Fraction-specific geochemistry across the Asbestos Hills BIF of the Transvaal Supergroup, South Africa: implications for the origin of BIF and the history of atmospheric oxygen. *Unpublished PhD thesis*, Rhodes University, 211p. http://hdl.handle.net/10962/50721

Moore, J.M., Polteau, S., Armstrong, R.A., Corfu, F. and Tsikos, H., 2012. The age and correlation of the Postmasburg Group, southern Africa: Constraints from detrital zircon grains. J. African Earth Sci. , 64, 9-19. https://doi.org/10.1016/j.jafrearsci.2011.11.001

Moore, J.M., Tsikos, H. and Polteau, S., 2001. Deconstructing the Transvaal Supergroup, South Africa: implications for Palaeoproterozoic palaeoclimate models. J. African Earth Sci. , 33, 437-444. https://doi.org/10.1016/S0899-5362(01)00084-7

Murray, J.W., Dillard, J.G., Giovanoli, R., Mores, H. and Stumm, W., 1985. Oxidation of Mn(II): initial mineralogy, oxidation state and ageing. Geochim. Cosmochim. Acta, 49, 463-470. https://doi.org/10.1016/0016-7037(85)90038-9

Namgung, S., Chon, C.M. and Lee, H., 2018. Formation of diverse Mn oxides: a review of biogeochemical processes of Mn oxidation. Geosciences, 22(2), 373-381. https://doi.org/10.1007/s12303-018-0002-7

Nealson, K.H. and Saffarini, D., 1994. Iron and manganese in anaerobic respiration: environmental significance, physiology, and regulation. Annu. Rev. Microbiol., 48(1), 311-343.

Nealson, K.H. and Myers, C.R., 1992. Microbial reduction of manganese and iron: new approaches to carbon cycling. Microbiol. Rev., 58(2), 439-443.

Okita, P.M., Maynard, J.B., Spiker, E.C. and Force, E.R., 1988. Isotopic evidence for organic matter oxidation by manganese reduction in the formation of stratiform manganese carbonate ore. Geochim. Cosmochim. Acta, 52(11), 2679-2685. https://doi.org/10.1016/0016-7037(88)90036-1

Okita, P.M. and Shanks, W.C., 1992. Origin of stratiform sediment-hosted manganese carbonate ore deposits: Examples from Molango, Mexico, and TaoJiang, China. Chem. Geol., 99(1), 139-163. https://doi.org/10.1016/0009-2541(92)90036-5

Oonk, P.B.H., Tsikos, H., Mason, P.R., Henkel, S., Staubwasser, M., Fryer, L., Poulton, S.W. and Williams, H.M., 2017. Fraction-specific controls on the trace element distribution in iron

formations: Implications for trace metal stable isotope proxies. Chem. Geol., 474, 17-32. https://doi.org/10.1016/j.chemgeo.2017.10.018

Ostrander, C.M., Nielsen, S.G., Owens, J.D., Kendall, B., Gordon, G.W., Romaniello, S.J. and Anbar, A.D., 2019. Fully oxygenated water columns over continental shelves before the Great Oxidation Event. Nat. Geosci., 12, 186-191. https://doi.org/10.1038/s41561-019-0309-7

Planavsky, N., Asael, D., Hofmann, A., Reinhard, T., Lalonde, S.V., Knudsen, A. Wang, X., Ossa Ossa, F., Pecoits, E., Smith, A.J.B., Beukes, N.J., Bekker, A., Johnson, T.M., Konhauser, K.O., Lyons, T.W. and Rouxel, O.J., 2014. Evidence for oxygenic photosynthesis half a billion years before the Great Oxidation Event. Nat. Geosci., 7, 283-286. https://doi.org/10.1038/ngeo2122

Pecoits, E., Gingras, M.K., Barley, M.E., Kappler, A., Posth, N.R. and Konhauser, K.O., 2009. Petrography and geochemistry of the Dales Gorge banded iron formation: Paragenetic sequence, source and implications for Palaeo-ocean chemistry. Precambrian Res, 172, 163–187. https://doi.org/10.1016/j.precamres.2009.03.014

Pickard, A.L., 2003. SHRIMP U–Pb zircon ages for the Palaeoproterozoic Kuruman Iron Formation, Northern Cape Province, South Africa: evidence for simultaneous BIF deposition on the Kaapvaal and Pilbara cratons. Precambrian Res, 125(3-4), 275-315. https://doi.org/10.1016/S0301-9268(03)00113-X

Planavsky, N., Rouxel, O.J., Bekker, A., Hofmann, A., Little, C.T.S. and Lyons, T.W., 2012. Iron isotope composition of some Archean and Proterozoic iron formations. Geochim. Cosmochim. Acta, 80, 158–169 https://doi.org/10.1016/j.gca.2011.12.001

Planavsky, N., Bekker, A., Rouxel, O.J., Kamber, B., Hofmann, A., Knudsen, A. and Lyons, T.W., 2010. Rare earth element and yttrium compositions of Archean and Paleoproterozoic Fe formations revisited: new perspectives on the significance and mechanisms of deposition. Geochim. Cosmochim. Acta, 74(22), 6387-6405. https://doi.org/10.1016/j.gca.2010.07.021

Polgari, M., Okita, P.M. and Hein, J.R., 1991. Stable isotope evidence for the origin of the Úrkút manganese ore deposit, Hungary. J. Sediment. Res., 61(3), 384-393. https://doi.org/10.1306/D426771C-2B26-11D7-8648000102C1865D

Polteau, S., Moore, J.M. and Tsikos, H., 2006. The geology and geochemistry of the Palaeoproterozoic Makganyene diamictite. Precambrian Res, 148(3-4), 257-274. https://doi.org/10.1016/j.precamres.2006.05.003

Posth, N.R., Köhler, I., Swanner, E.D., Schröder, C., Wellmann, E., Binder, B., Konhauser, K.O., Neumann, U., Berthold, C., Nowak, M. and Kappler, A., 2013. Simulating Precambrian banded iron formation diagenesis. Chem. Geol., 362, 66-73. https://doi.org/10.1016/j.chemgeo.2013.05.031

Preston, P.C.C.R., 2001. Physical and chemical characterization of the manganese ore bed at the Mamatwan mine, Kalahari manganese field. *Unpublished MSc dissertation*, University of Johannesburg, 146p.

Raiswell, R., Reinhard, C.T., Derkowski, A., Owens, J., Poulton, S.H., Anbar, A.D. and Lyons, T.W., 2011. Formation of syngenetic and early diagenetic iron minerals in the late Archean Mt. McRae Shale, Hamersley Basin, Australia: New insights on the patterns, controls and paleoenvironmental implications of authigenic mineral formation. Geochim. Cosmochim. Acta, 75(4), 1072-1087. https://doi.org/10.1016/j.gca.2010.11.013

Rasmussen, B. and Muhling, J.R., 2018. Making magnetite late again: Evidence for widespread magnetite growth by thermal decomposition of siderite in Hamersley banded iron formations. Precambrian Res, 306, 64-93. https://doi.org/10.1016/j.precamres.2017.12.017

Rouxel, O., Sholkovitz, E., Charette, M. and Edwards, K.J., 2008. Iron isotope fractionation in subterranean estuaries. Geochim. Cosmochim. Acta, 72(14), 3413-3430. https://doi.org/10.1016/j.gca.2008.05.001

Rouxel, O., Toner, B., Manganini, S. and German, C., 2016. Geochemistry and Iron Isotope Systematics of Hydrothermal Plume Fall-out at EPR9°50'N. Chem. Geol., 441, 212-234. https://doi.org/10.1016/j.chemgeo.2016.08.027

Rouxel, O.J., Bekker, A. and Edwards, K.J., 2005. Iron isotope constraints on the Archean and Paleoproterozoic ocean redox state. Science, 307(5712), 1088-1091. DOI: 10.1126/science.1105692

Roy, S., 2006. Sedimentary manganese metallogenesis in response to the evolution of the Earth system. Earth Science Reviews, 77(4), 273-305. https://doi.org/10.1016/j.earscirev.2006.03.004

Schad, M., Byrne, J.M., Thomas Arrigo, L.K., Kretzschmar, R., Konhauser, K.O. and Kappler, A., 2022. Microbial Fe cycling in a simulated Precambrian ocean environment: Implications for secondary mineral (trans)formation and deposition during BIF genesis. Geochim. Cosmochim. Acta, 331, 165-191. https://doi.org/10.1016/j.gca.2022.05.016

Schier, K., Bau, M., Smith, A.J.B., Beukes, N.J., Coetzee, L.L. and Viehmann, S., 2020. Chemical evolution of seawater in the Transvaal Ocean between 2426 Ma (Ongeluk Large Igneous Province) and 2413 Ma ago (Kalahari Manganese Field). Gondwana Res, 88, 373-388. https://doi.org/10.1016/j.gr.2020.09.001

Schneiderhahn, E.A., Gutzmer, J., Strauss, H., Mezger, K. and Beukes, N.J. 2006. The chemo-stratigraphy of a Paleoproterozoic MnF-BIF succession - the Voëlwater Subgroup of the Transvaal Supergroup in Griqualand West, South Africa. South Afr J Geol, 109, 63-80. https://doi.org/10.2113/gssajg.109.1-2.63

Siahi, M., Tsikos, H., Rafuza, S., Oonk, P.B.H., Mason, P.R.D., Mhlanga, X.R., van Niekerk, D. and Harris, C., 2020. Insights into the processes and controls for the absolute abundance and distribution of manganese in Precambrian Iron Formations. Precambrian Res, 350, 105878. https://doi.org/10.1016/j.precamres.2020.105878

Sumner, D.Y. and Bowring, S.A., 1996. U-Pb geochronologic constraints on deposition of the Campbellrand Subgroup, Transvaal Supergroup, South Africa. Precambrian Res, 79(1-2), 25-35. https://doi.org/10.1016/0301-9268(95)00086-0

Sumner, D.Y., 1997. Late Archean calcite-microbe interactions; two morphologically distinct microbial communities that affected calcite nucleation differently. Palaios, 12(4), 302-318. https://doi.org/10.2307/3515333

Thibon, F., Blichert-Toft, J., Tsikos, H., Foden, J., Albalat, E. and Albarede, F., 2019. Dynamics of oceanic iron prior to the Great Oxygenation Event. Earth Planet. Sci. Lett., 506, 360-370. https://doi.org/10.1016/j.epsl.2018.11.016

Thompson, K.J., Kenward, P.A., Bauer, K.W., Warchola, T., Gauger, T., Martinez, R., Simister, R.L., Michiels, C.C., Llirós, M., Reinhard, C.T. and Kappler, A., 2019. Photoferrotrophy, deposition of banded iron formations, and methane production in Archean oceans. Sci. Adv., 5(11), p.eaav2869. DOI: 10.1126/sciadv.aav2869

Trendall, A.F., Nelson, D.R., Thorne, A.M., Compston, W., Williams, I.S. and Armstrong, R.A., 1990. Precise zircon U-Pb chronological comparison of the volcano-sedimentary sequences of the Kaapvaal and Pilbara Cratons between about 3.1 and 2.4 Ga. In: Third International Archaean Symposium (Abstract Volume), Perth.

Trouwborst, R.E., Clement, B.G., Tebo, B.M., Glazer, B.T. and Luther, G.W., 2006. Soluble Mn (III) in suboxic zones. Science, 313(5795), 1955-1957. DOI: 10.1126/science.113287

Tsikos, H. and Moore, J.M., 1997. Petrography and geochemistry of the Paleoproterozoic Hotazel iron-formation, Kalahari Manganese Field, South Africa: Implications for Precambrian manganese metallogenesis. Econ Geol, 92(1), 87–97. https://doi.org/10.2113/gsecongeo.92.1.87

Tsikos, H., Beukes, N.J. and Harris, C., 2003. Deposition, Diagenesis, and Secondary Enrichment of Metals in the Paleoproterozoic Hotazel Iron Formation, Kalahari Manganese Field, South Africa. Econ Geol, 98(1), 1449–1462. https://doi.org/10.2113/gsecongeo.98.7.1449

Tsikos, H., Mathews, A., Erel, Y. and Moore, J.M., 2010. Iron isotopes constrain biogeochemical redox cycling of iron and manganese in a Palaeoproterozoic stratified basin. Earth Planet. Sci. Lett., 298(1-2), 125–134. https://doi.org/10.1016/j.epsl.2010.07.032

Tsikos, H., Siahi, M., Rafuza, S., Mhlanga, X.R., Oonk, P.B.H., Papadopoulos, V., Boyce, A.C., Mason, P.R.D., Harris, C., Gröcke, D.R. and Lyons, T.W., 2022. Carbon isotope stratigraphy of Precambrian Iron Formations and implications for the early biological pump. Gondwana Res, 109, 416-428. https://doi.org/10.1016/j.gr.2022.05.007

Walker, J.C.G., 1984. Suboxic diagenesis in banded iron formations. Nature, 309(5966), 340-342. https://www.doi.org/10.1038/309340a0

Walraven, F., 1995. Zircon Pb-evaporation age determinations of the Oak Tree Formation, Chuniespoort Group, Transvaal sequence: implications for Transvaal-Griqualand West basin correlations. South Afr J Geol, 98(1), 58-67. https://hdl.handle.net/10520/EJC-929187cc0

Wittkop, C., Swanner, E.D., Grengs, A., Lambrecht, N., Fakhraee, M., Myrbod, A., Bray, A.W., Poulton, S.W., and Katsev, S., 2020. Evaluating a primary carbonate pathway for manganese enrichments in reducing environments. Earth Planet. Sci. Lett. https://doi.org/10.1016/j.Earth Planet. Sci. Let. 2020.116201.

Figure Captions

Figure 1: (I) A drill core log (GL137) showing the cyclic nature of the Hotazel Formation in its entirety. (II) Representative view of the lithologic transition: BIF-hematite lutite-Mn ore as it develops in a drill core intersecting the lower section of the uppermost Mn cycle of unaltered Hotazel Formation at Gloria Mn mine. Width of core: 4.5cm.

Figure 2: Ranges of bulk carbonate-carbon isotopes from various Archean-Palaeoproterozoic deposits around the globe. a) Hotazel Mn rich layers [**avg -9.9 ‰**]; and b) Hotazel BIF [**avg -10.0 ‰**] (this study); c) Ghaap group (Asbestos Hills and Koegas BIFs) [**avg -9.5 ‰**] (Rafuza 2015; Beukes and Klein 1990, Heimann et al, 2010), Johnson et al., 2013a); d) Hamersley BIFs [**avg -8.2 ‰**] (Becker and Clayton 1972; Baur et al 1985; Kaufman et al 1990). All deposits are of low metamorphic grade with maximum burial temperatures ~300°C for the Western Australian deposits and ~150°C for the Transvaal basin deposits (Klein and Gole 1981a; Miyano and Klein 1983a; Klein 2005).

Figure 3: Regional stratigraphy of the Transvaal Supergroup in the Griqualand West Basin, Northern Cape Province, South Africa. Thickness and age data from: a: Kunzmann et al. (2014); b: Tsikos et al. (2003), c: Polteau et al. (2006); d: Oonk et al. (2017); e: Sumner (1997); f: Bau et al. (1999); g: Cornell et al. (1996); h: Gumsley et al. (2017); i: Moore et al. (2012); j: Trendall et al. (1990); k: Pickard (2003); l: Sumner and Bowring (1996), m: Altermann and Nelson (1998); n: Walraven (1995). Modified from Oonk (2017).

Figure 4: Generalized geological map of the Kalahari Manganese Field (KMF) indicating the locality of drill cores GL136 and GL137 sampled in this study.

Figure 5: X-ray diffraction spectra (5-65° 2-theta) from the three representative lithofacies BIF (A, D, and H), Mn-ore (B, C and F), and hematite lutite (E and G) throughout the entire stratigraphy from drill core GL137. Abbreviations: Ank (ankerite); Mt (magnetite); Cc (calcite);

Kut (kutnahorite); Hem (hematite); Br (braunite); Frd (friedelite). GL137 samples selected: 3(A), 8(B), 15(C), 18(D), 54(E), 61(F) 75(G), 91(H).

Figure 6: SEM-BSE images of ankerite-dominated BIF from drillcore GL137, samples: 47(A), 43(B), 77(C & H), 79 (D & E), 90(F), and 45(G), indicating textural relationships between oxide, silicate and carbonate minerals. Abbreviations: Cc (calcite); Ank (ankerite); Mt (magnetite); Qz (quartz); Kut (kutnahorite); Hem (hematite); Br (braunite).

Figure 7: SEM-BSE images of siderite textural relationships in BIF from drillcore GL137, sample: 38(A) and 90(B-D). Abbreviations: Cc (calcite); Ank (ankerite); Sid (siderite) Mt (magnetite); Qz (quartz); Kut (kutnahorite); Hem (hematite); Br (braunite).

Figure 8: SEM-BSE images of textural relationships between carbonates and oxides in transitional hematite lutite from drillcore GL137, samples: 25(A), 10(B), 34(C), 35(D), 54(E), 22(F), and 36 (G & H). Abbreviations: Cc (calcite); Ank (ankerite); Mt (magnetite); Qz (quartz); Kut (kutnahorite); Hem (hematite); Br (braunite).

Figure 9: SEM-BSE images of mineral textures in manganese ore from drill core GL137. Samples: 13(A & B), 63(C, E & G), 10(D), and 15(F & H), show relationships between manganese-rich carbonates, silicates and hematite. Abbreviations: Cc (calcite); Ank (ankerite); Mt (magnetite); Qz (quartz); Kut (kutnahorite); Hem (hematite); Br (braunite); Frd (friedelite).

Figure 10: High-resolution major oxide chemostratigraphic relationships from drill core GL136. Subdivisions into different sub-cycles are labeled along the right-hand edge of the figure.

Figure 11: High resolution chemostratigraphy of the Hotazel Formation from drill core GL137 indicating variations in carbonate-hosted stratigraphic trends for Fe, Mn, Ca, Mg (in wt.%) across all major lithofacies (BIF, Mn ore and transitional hematite lutite).

Figure 12: Averaged major-element compositions of kutnahorite (light grey), rhodochrosite (dark grey), ankerite (light green) and siderite (dark green) obtained from spot analyses on polished thin sections of representative samples across the Hotazel stratigraphy. It must be noted that only average data that were derived from five or more spot analyses per individual sample are reported here (see supplementary file 5 for complete sets of analyses). SD=standard deviation (1σ); *n*=number of analyses.

Figure 13: Stratigraphic, bulk-rock $\delta^{56}Fe$ and carbonate $\delta^{13}C$ records from drill cores GL136 and GL137. The $\delta^{56}Fe$ data from this study represent predominantly the upper half of the Hotazel stratigraphy (red markers) and complement $\delta^{56}Fe$ results for the lower half of the Hotazel succession from a very similar intersection (GL26) as reported by Tsikos *et al. (*2010) (blue markers). See text for more details.

Figure 14: High-resolution profiles of bulk carbonate $\delta^{13}C$, bulk $\delta^{56}Fe$, bulk Fe/Ca and bulk Mn/Ca from three representative samples of (top down): uppermost hematite lutite; middle BIF; and lowermost Mn-ore layer of the Hotazel Formation from drillcore GL136.

Figure 15: High resolution bulk carbonate-specific ratios and bulk carbonate $\delta^{13}C$ data from the upper Fe-Mn-Fe cycle of the Hotazel Formation, drillcore GL137.

Figure 16: Left: Scanned thin-section of manganese ore showing distribution of carbonate laminae. Right: Mn-calcite (dark grey) and kutnahorite (light grey) MnO/CaO ratio distributions and textural variations between laminae (L1-L7) across the same thin section. Note: length of white scale bar on BSE images represents1*0* µm.

Figure 17: Carbonate $\delta^{13}C$ *versus* Mn/Ca from samples of the Mn rich portions (hematite lutite and Mn ore layer) of the Fe-Mn-Fe upper cycle in the Hotazel Formation.

Figure 18: Ranges of bulk rock $\delta^{56}Fe$ values from: A) Hotazel hematite lutite (orange) & Mn ore (black) (this study; Thibon *et al*., 2019), B) Hotazel BIF (this study; Thibon *et al*., 2019), and C) Asbestos Hills BIF (Johnson *et al*., 2008a; Thibon *et al*., 2019).

Figure 19: A conceptual model for the deposition of the Hotazel Formation presented in three stages. Gradients of Fe/Mn, $\delta^{56}Fe_{aq}$ and $\delta^{13}C_{DIC}$ characterize ambient seawater. $O_{2(aq)}$ levels increase from anoxic to partially oxic with decreasing depth. (**A**) Deep level BIF deposition where an active Mn-Fe shuttle ($Mn(III)_{aq}$ oxidizes dissolved Fe(II) to ferrihydrite) recycles manganese back into solution as Mn(II), while primary ferric oxyhydroxide particles are partially reduced *via* DIR below the redoxcline, forming primary carbonates and possibly magnetite and silicates as they "rain down" to the seafloor. High Fe/Ca in solution leads to Fe carbonate saturation and precipitation. Carbonate minerals thus record seawater chemical signatures and recrystallize below the sediment-water interface through early and late-stage diagenesis. (**B**) During hematite lutite deposition, Mn oxidation just below the redoxcline leads to formation of soluble Mn(III) and

increasingly of MnOOH particles with decreasing water depth. Here, reduction of $Mn(III)_{aq}$ (and possibly of particulate MnOOH as well) will drive Fe(II) oxidation to Fe(III) but will also overwhelm redox cycling of C_{org} through DMR, leading to primary Mn carbonate saturation and nucleation. Highest Mn carbonate as rhodochrosite would be expected to be precipitated from zones of highest Mn(II) in solution relative to Ca(II). (**C**) During peak Mn deposition (Mn ore layers), a Mn-Fe shuttle is not operative in the shallowest parts of the water column above the redoxcline due to pervasive oxidation of both dissolved Mn(II) and Fe(II) by cyanobacterially produced O_2. Aerobic C_{org} oxidation is thus the dominant pathway here, resulting in low-Mn, Ca-rich carbonate formation (Mn-poor calcite and Ca-kutnahorite) and dominant Mn(III) precipitation as MnOOH. The latter is subsequently expected to be transformed into braunite in equilibrium with aqueous Si during diagenesis. Contemporaneous $Fe(OH)_3$ precipitation (eventually preserved as hematite) is ongoing throughout but very subdued by comparison.

Figure 20: An idealized diagram illustrating a regression-transgression cycle in the Hotazel Formation. The switch between redox pathways (DMR, DMR, and aerobic oxidation) corresponds to the succession of the three main lithotypes (BIF, Hematite lutite, and Mn ore layer) and tracks the stratigraphic change in the carbonate Mn/Ca ratio profile (left) as also shown in Fig. 15 earlier.

Figures

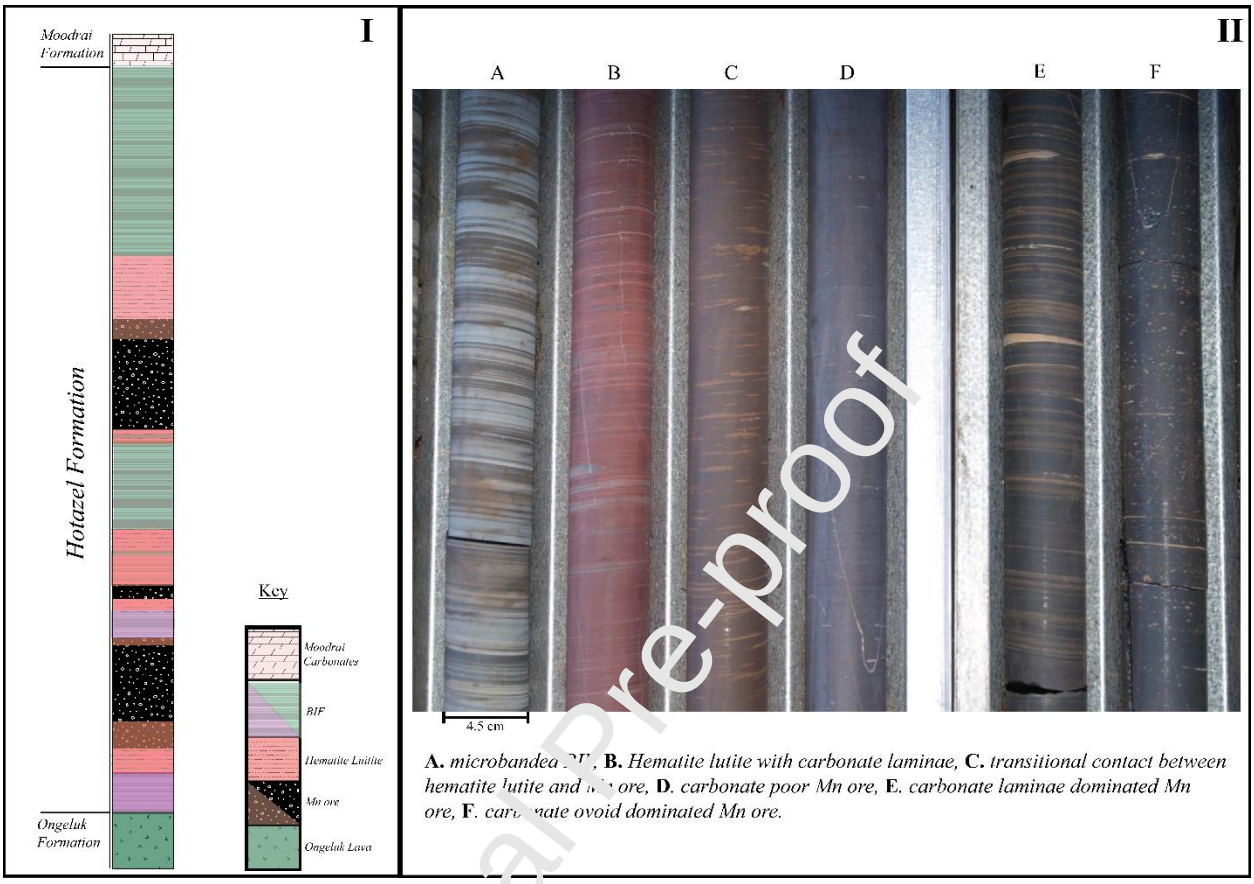

A. *microbanded BIF*, **B.** *Hematite lutite with carbonate laminae*, **C.** *transitional contact between hematite lutite and Mn ore*, **D.** *carbonate poor Mn ore*, **E.** *carbonate laminae dominated Mn ore*, **F.** *carbonate ovoid dominated Mn ore.*

1

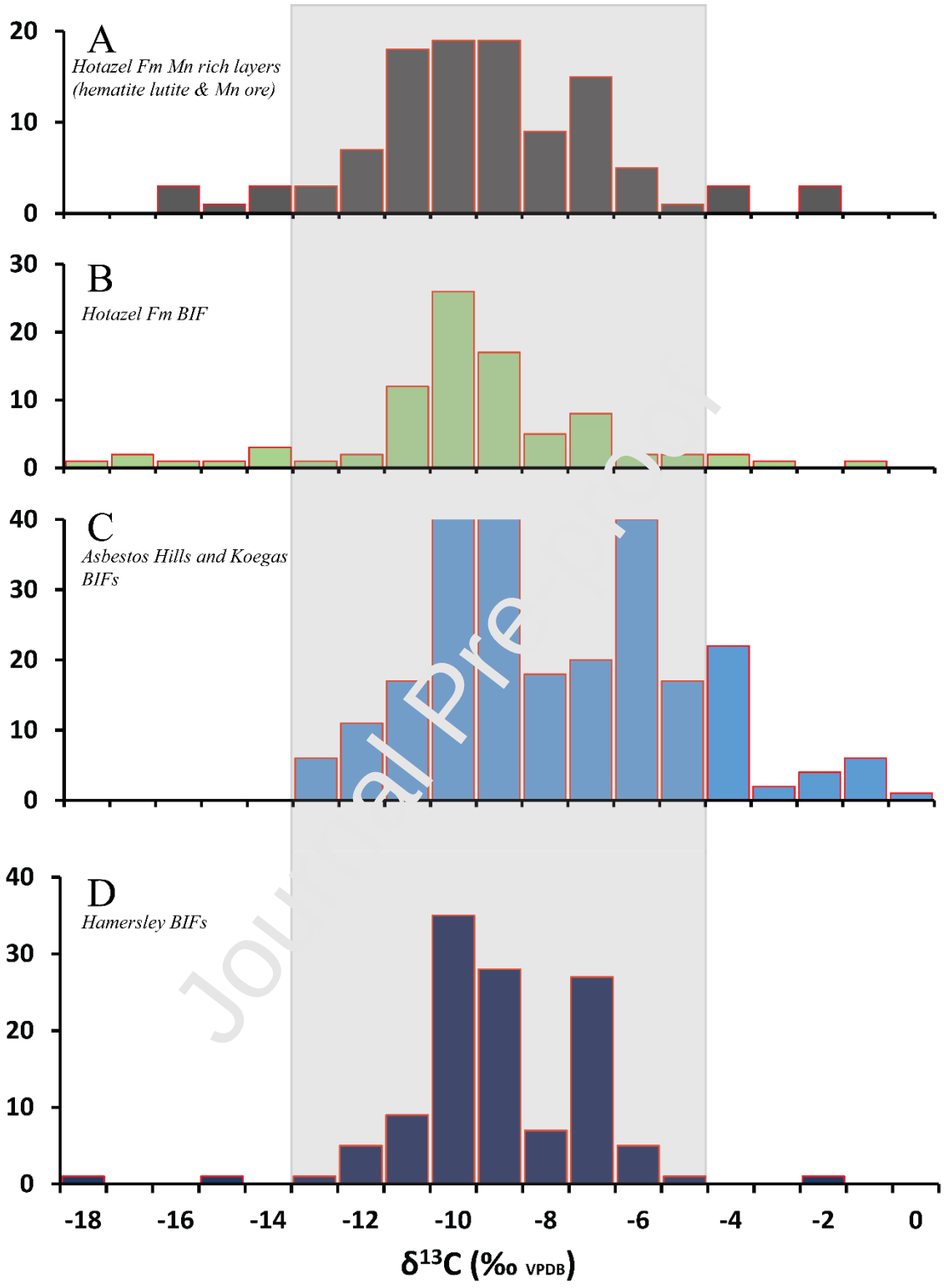
A
Hotazel Fm Mn rich layers
(hematite lutite & Mn ore)
B
Hotazel Fm BIF
C
Asbestos Hills and Koegas
BIFs
D
Hamersley BIFs
20
10
0
30
20
10
0
40
30
20
10
0
40
30
20
10
0
-18
-16
-14
-12
-10
-8
-6
-4
-2
0
δ13C (‰ VPDB)

2

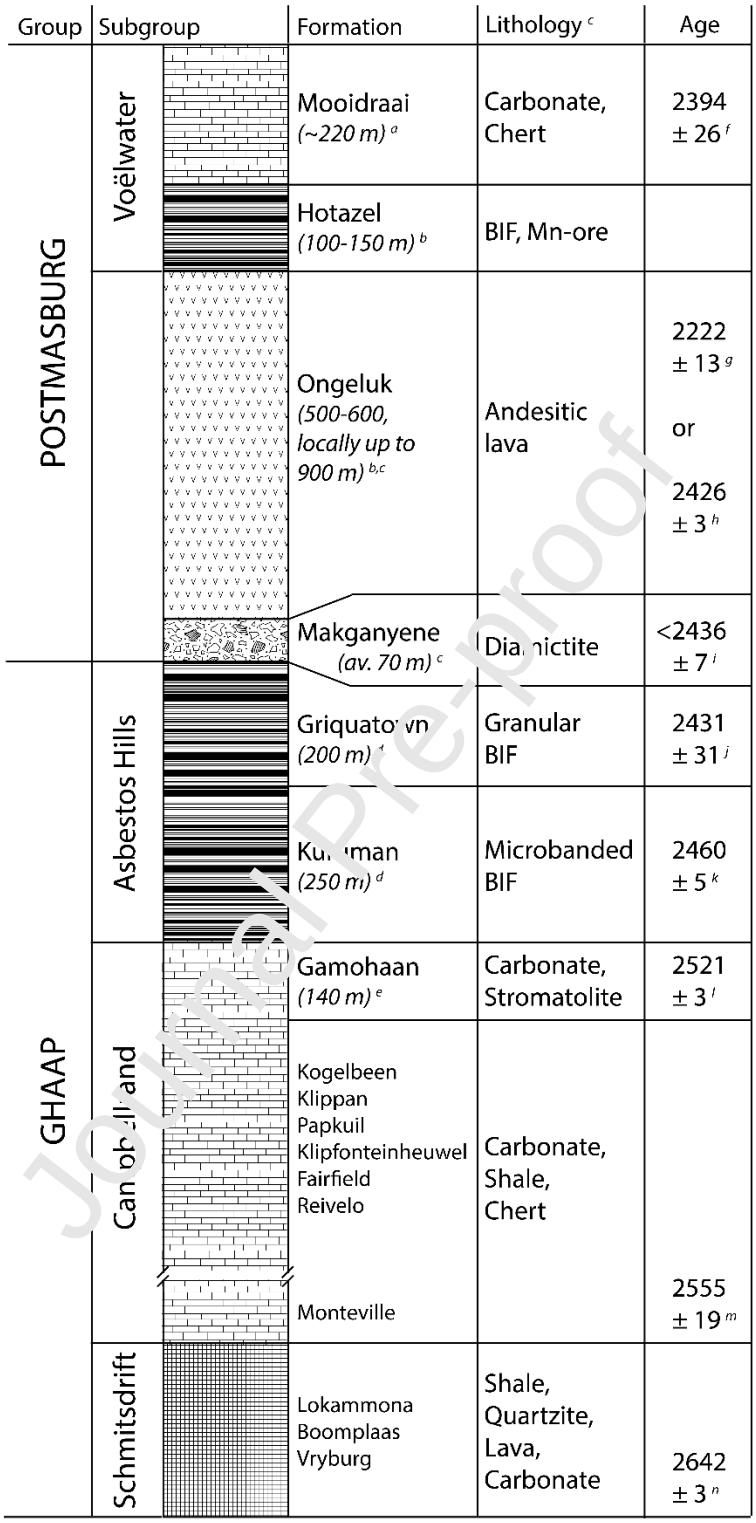
Group
Subgroup
Formation
Lithology c
Age
POSTMASBURG
GHAAP
Voëlwater
Asbestos Hills
Schmitsdrift
Mooidraai
(~220 m) a
Carbonate, Chert
2394 ± 26 f
Hotazel
(100-150 m) b
BIF, Mn-ore
Ongeluk
(500-600, locally up to 900 m) b,c
Andesitic lava
2222 ± 13 g
or
2426 ± 3 h
Makganyene
(av. 70 m) c
Diamictite
<2436 ± 7 i
Griquatown
(200 m) d
Granular BIF
2431 ± 31 j
Kuruman
(250 m) d
Microbanded BIF
2460 ± 5 k
Gamohaan
(140 m) e
Carbonate, Stromatolite
2521 ± 3 l
Kogelbeen
Klippan
Papkuil
Klipfonteinheuwel
Fairfield
Reivelo
Carbonate, Shale, Chert
Monteville
2555 ± 19 m
Lokammona
Boomplaas
Vryburg
Shale, Quartzite, Lava, Carbonate
2642 ± 3 n

3

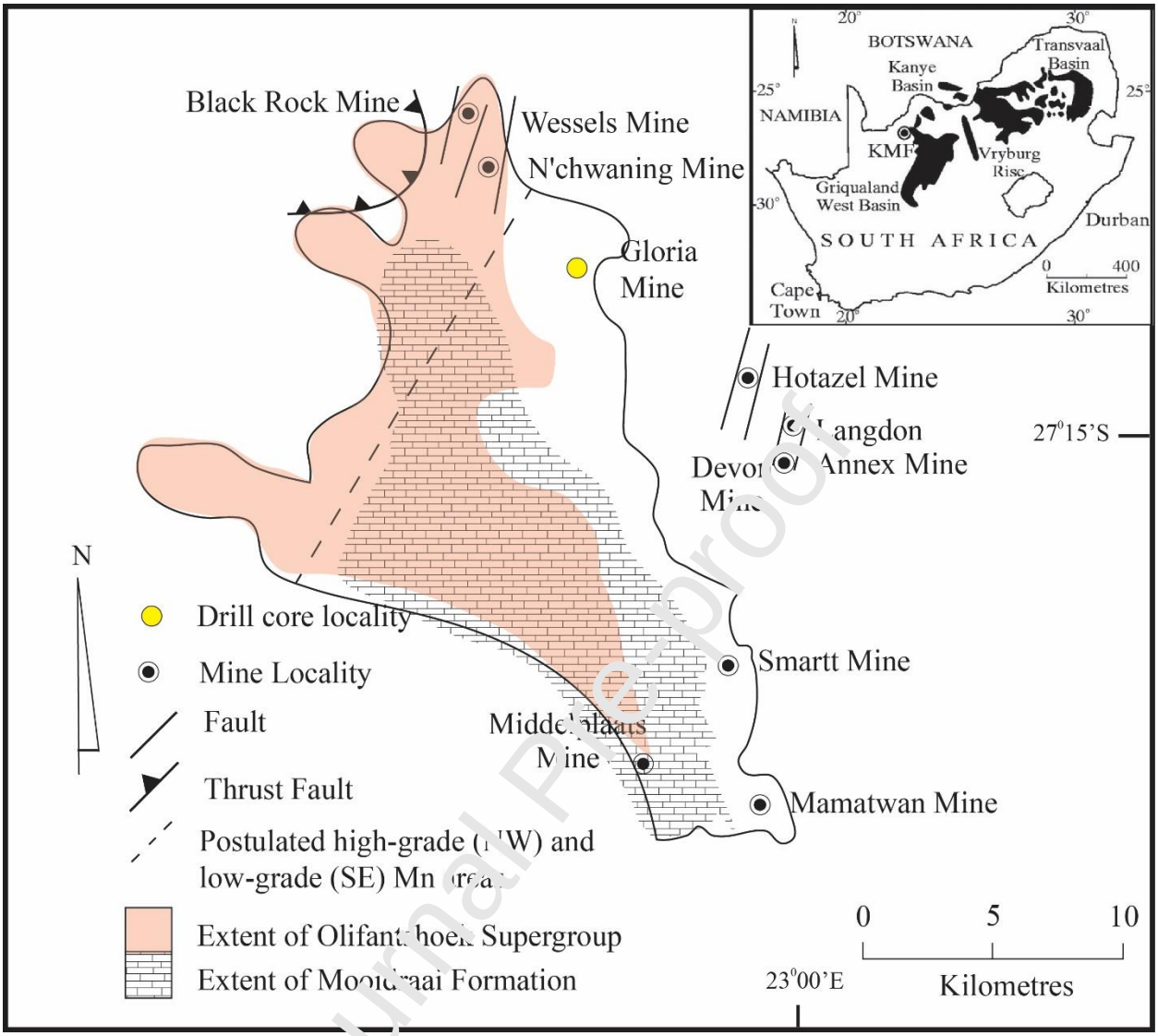

4

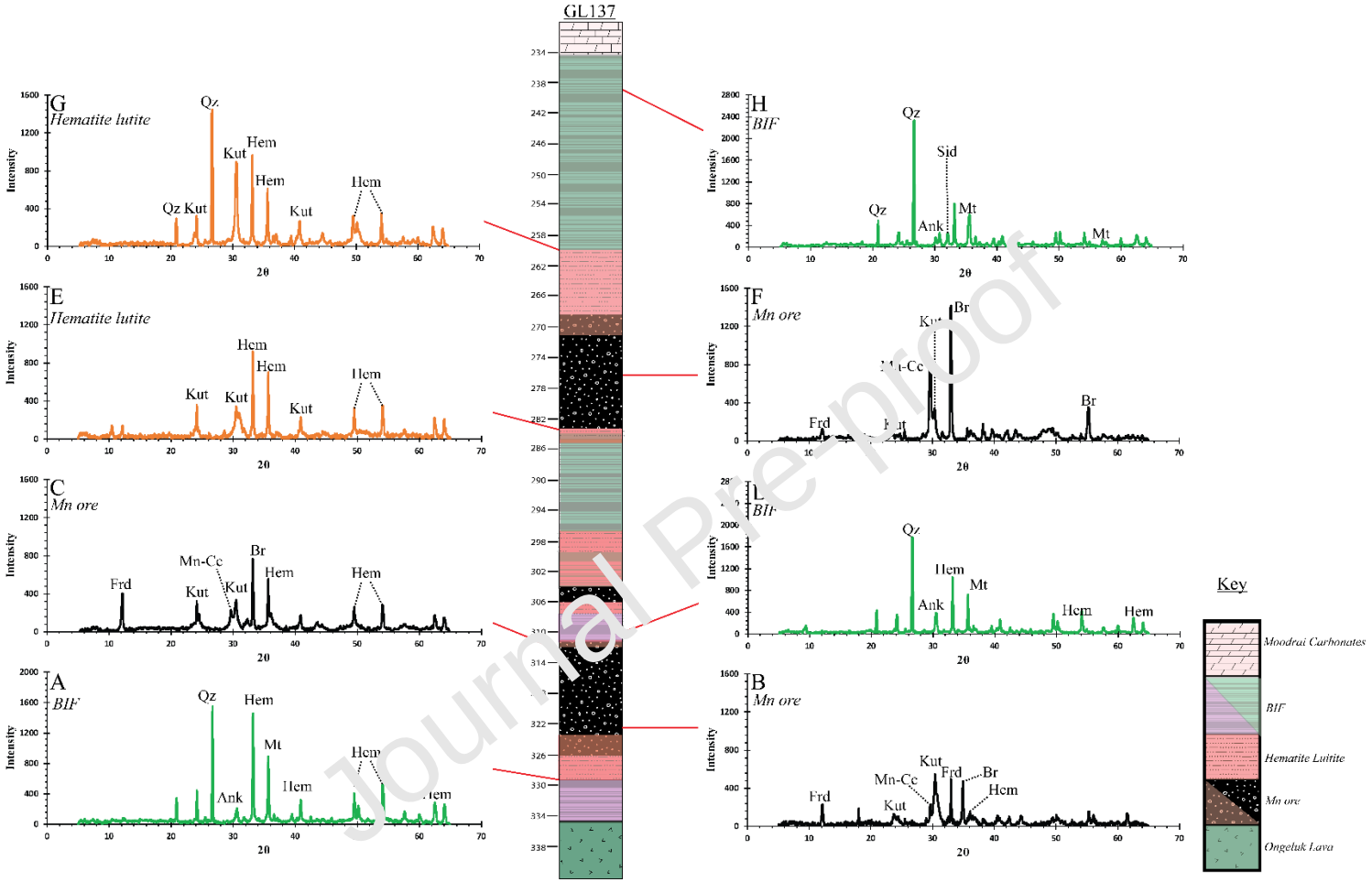

5

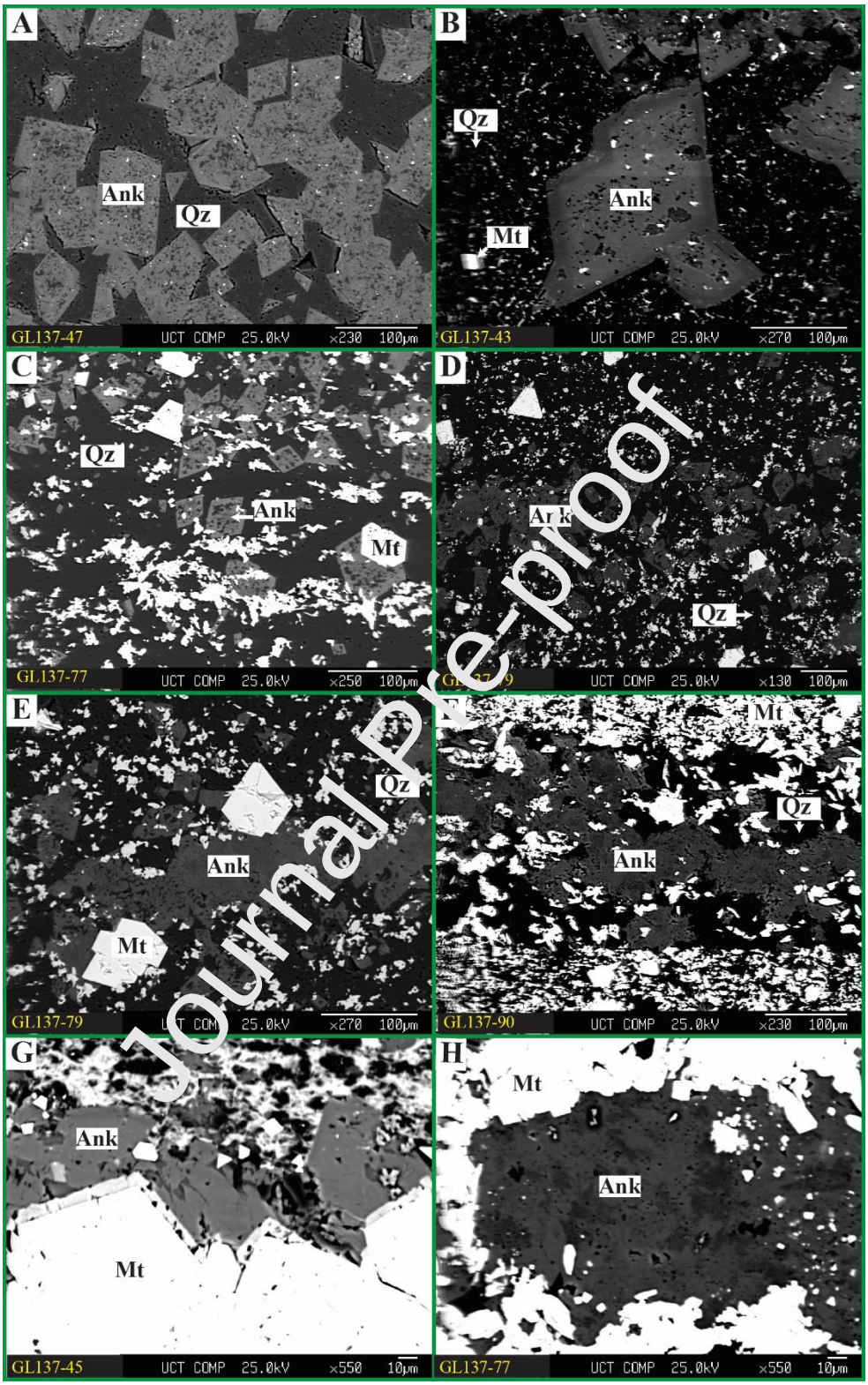

6

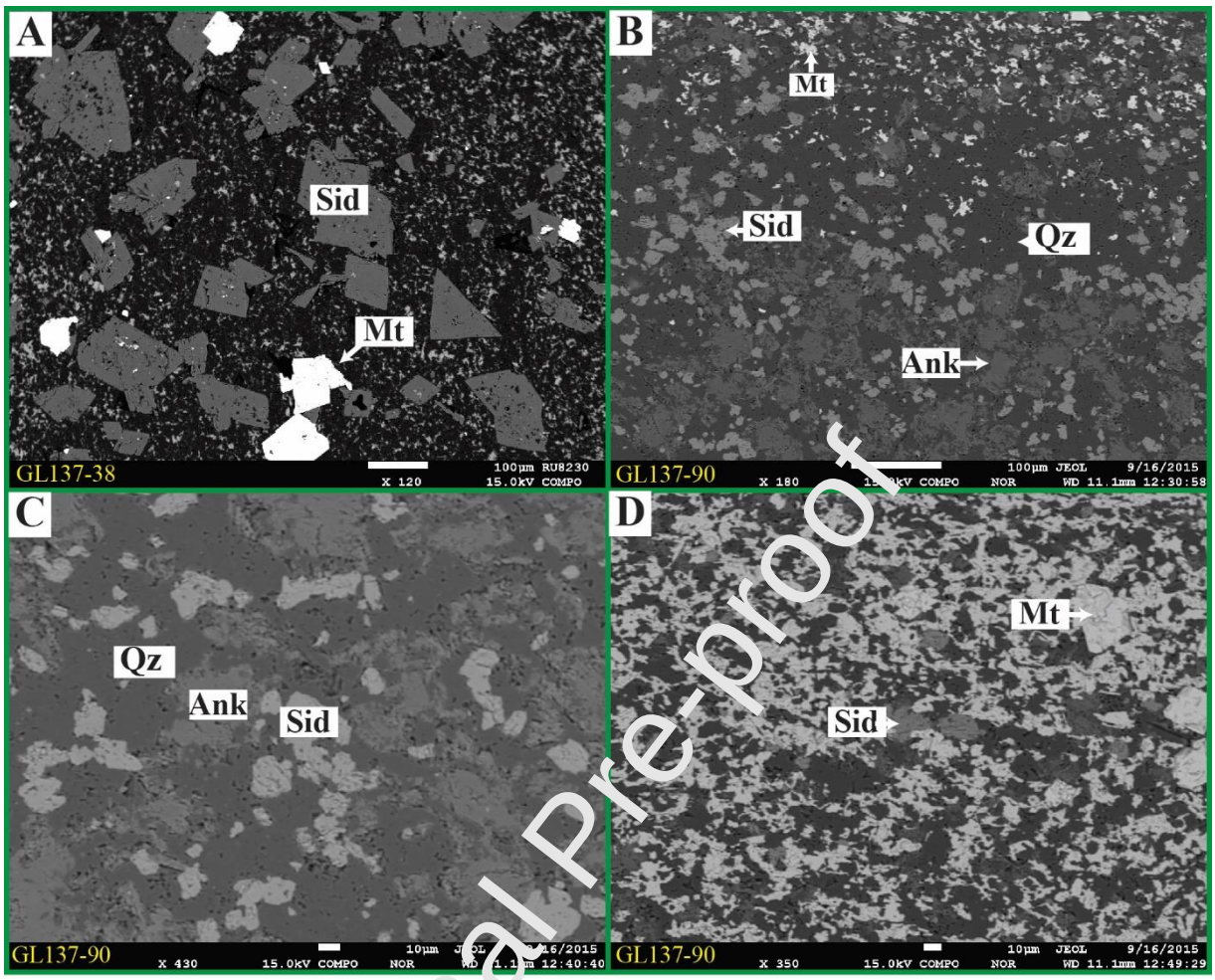

7

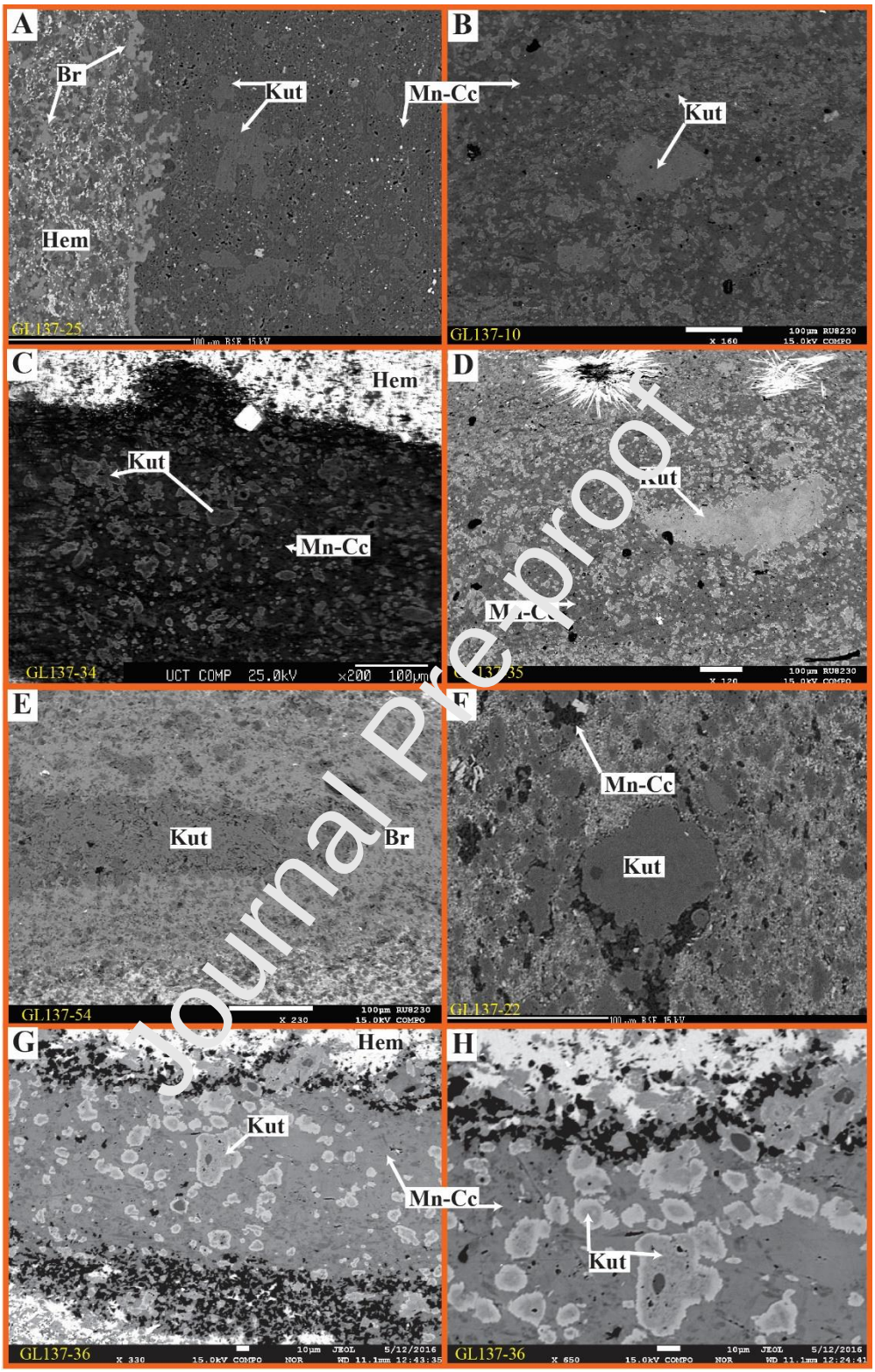

8

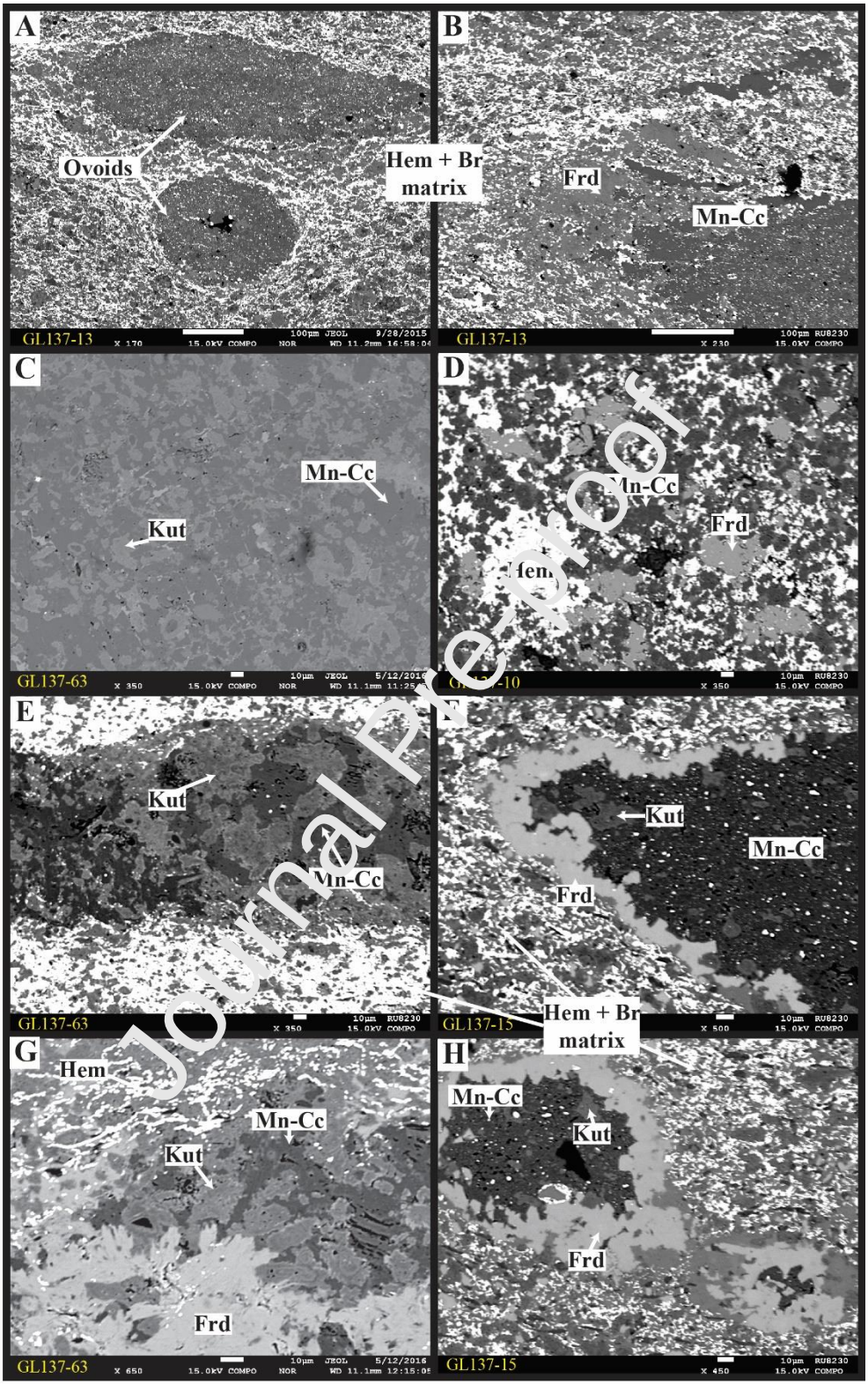

9

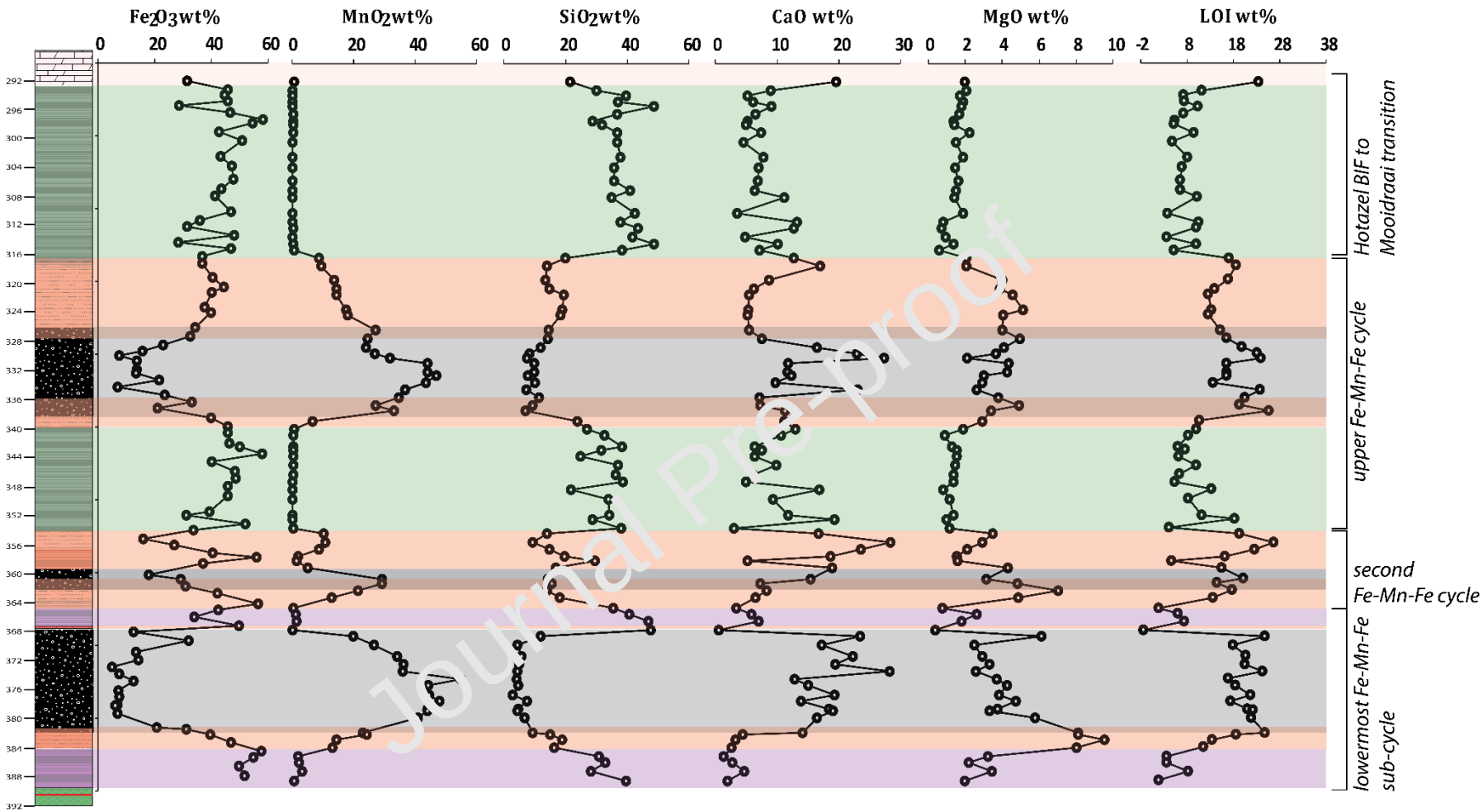

10

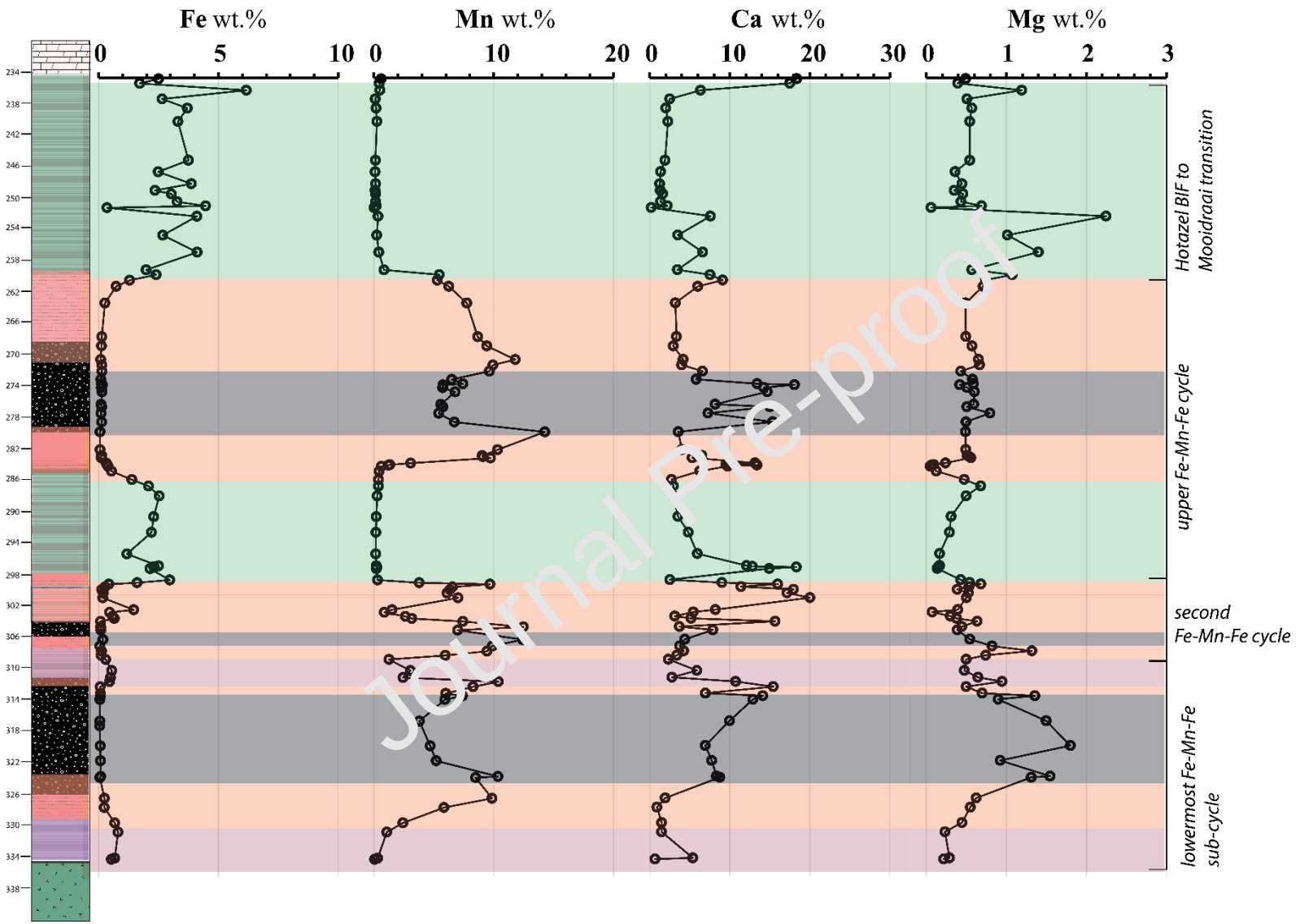

11

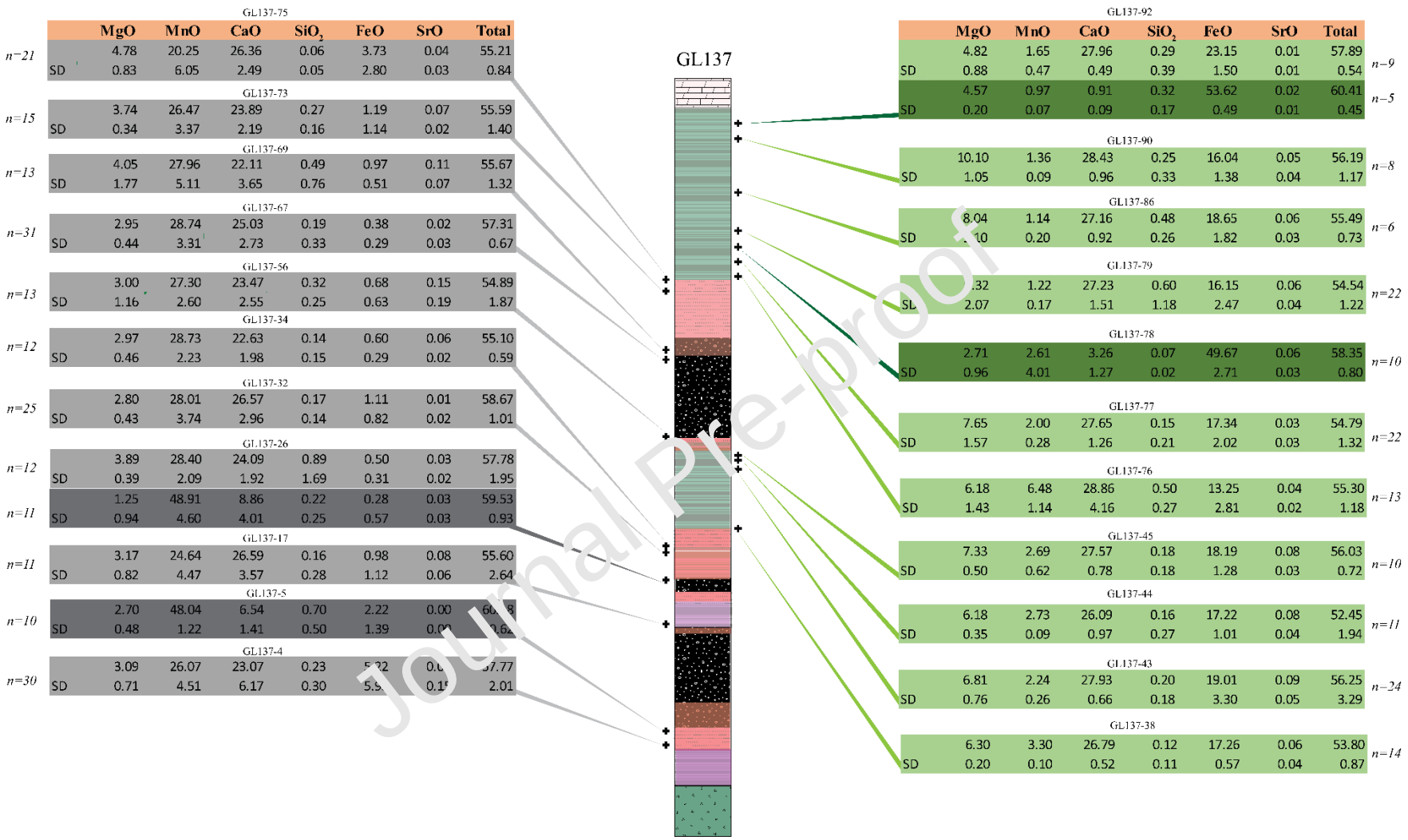

12

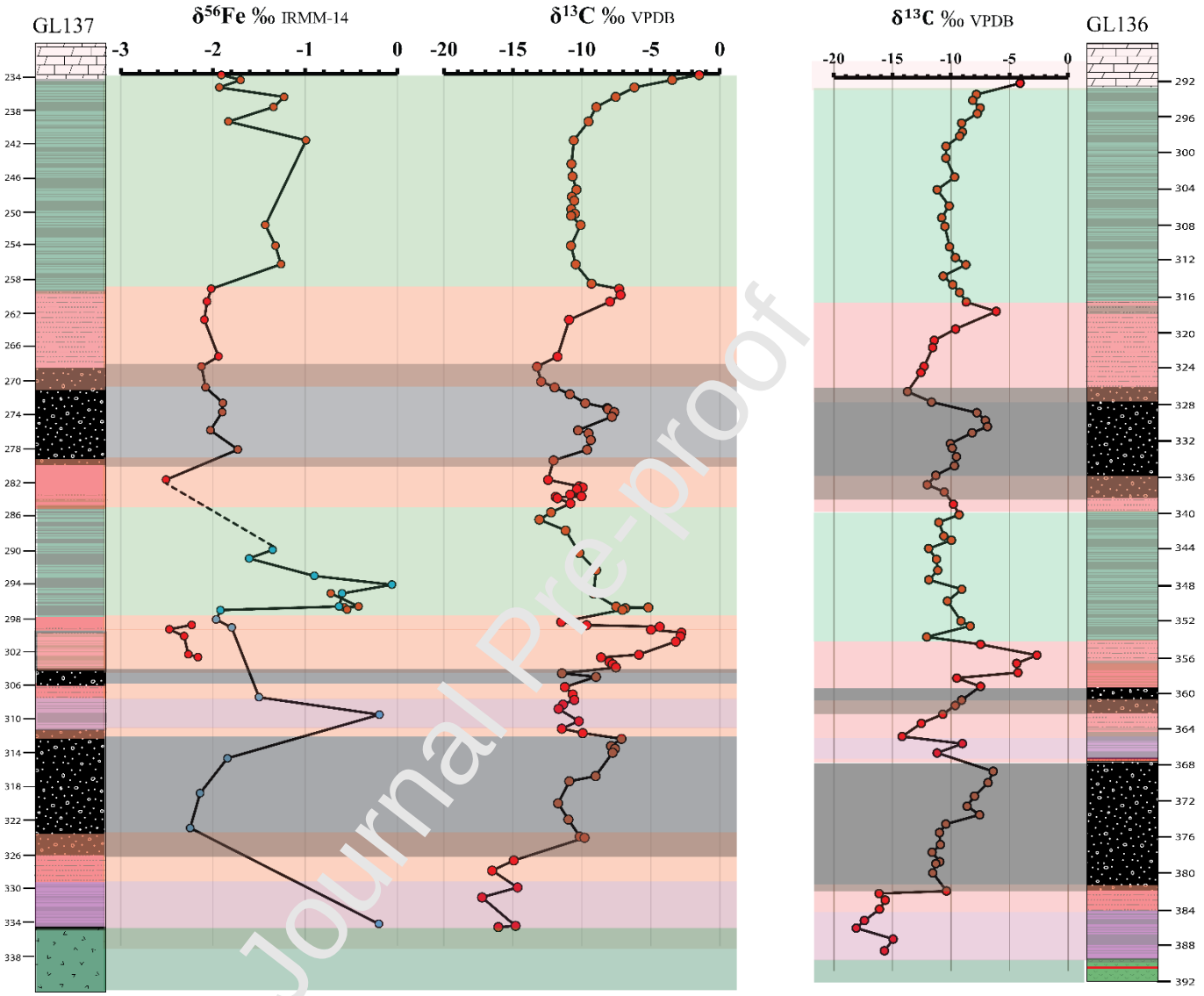

13

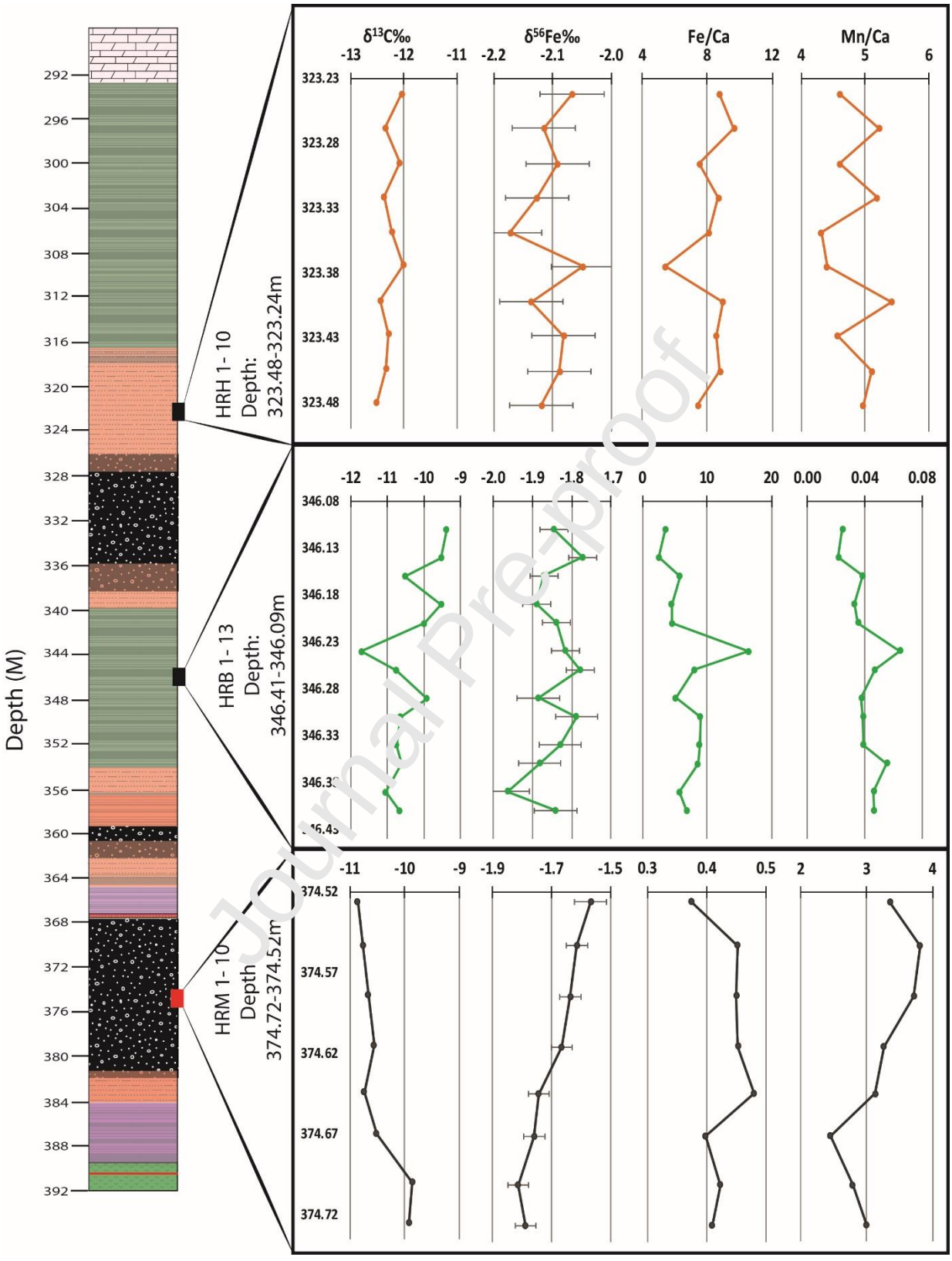

14

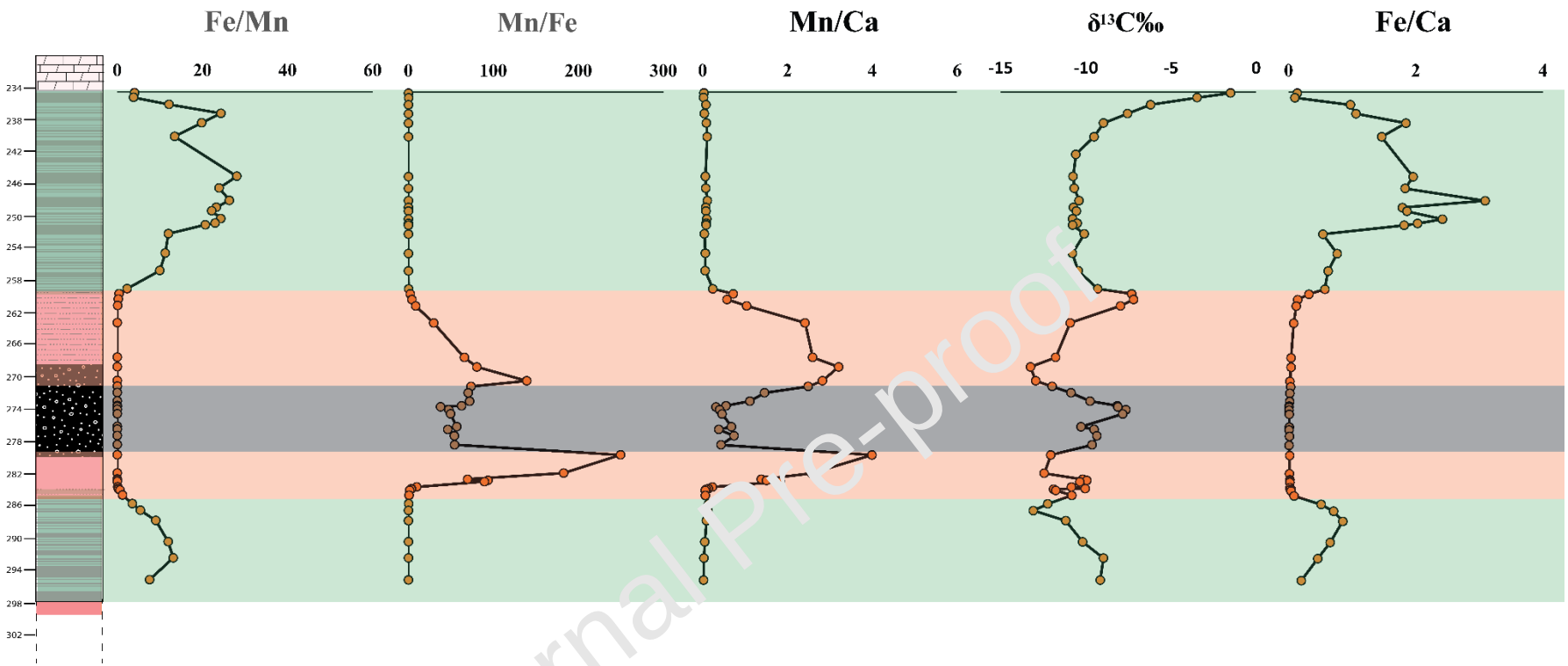

15

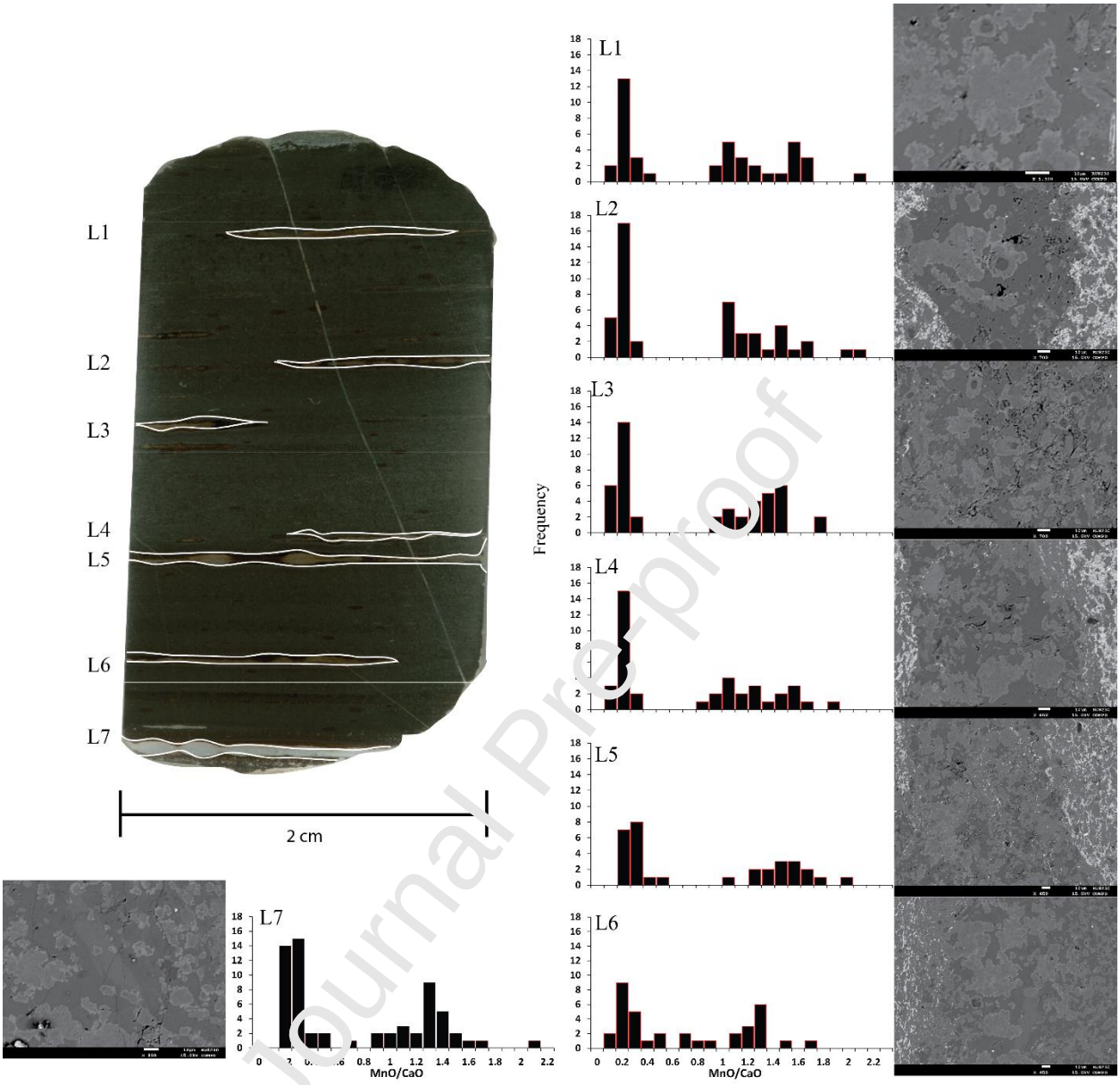

16

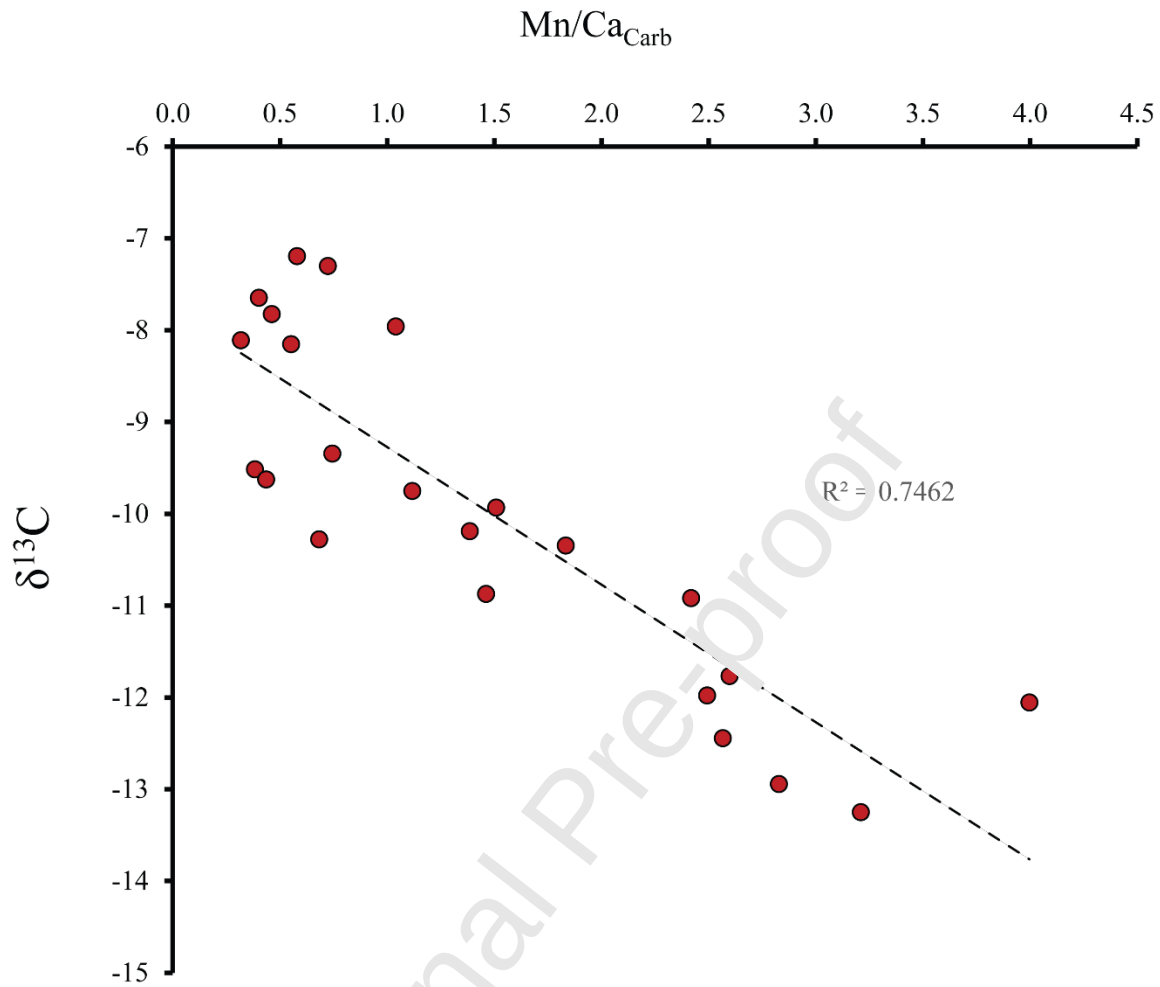

17

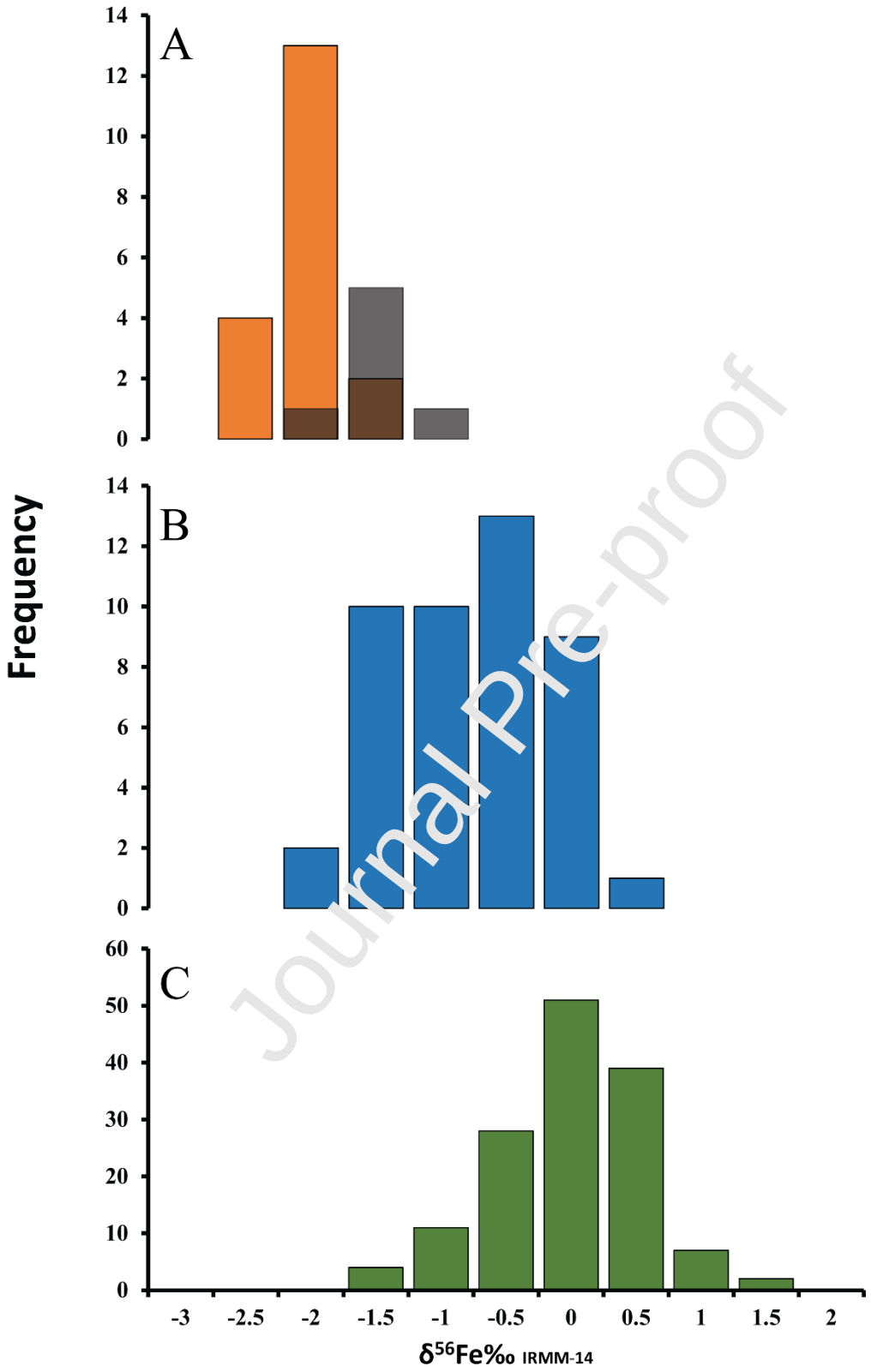

18

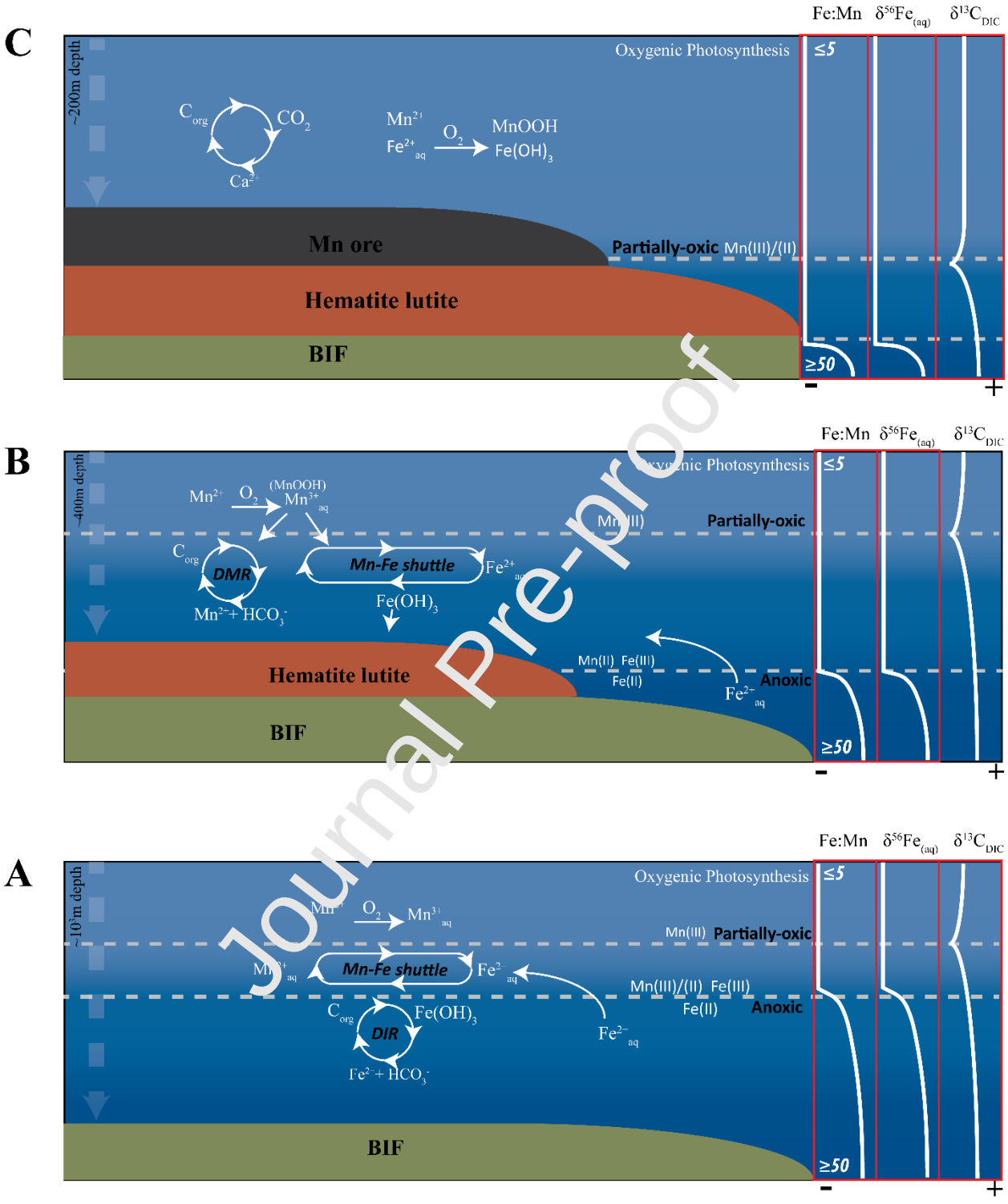

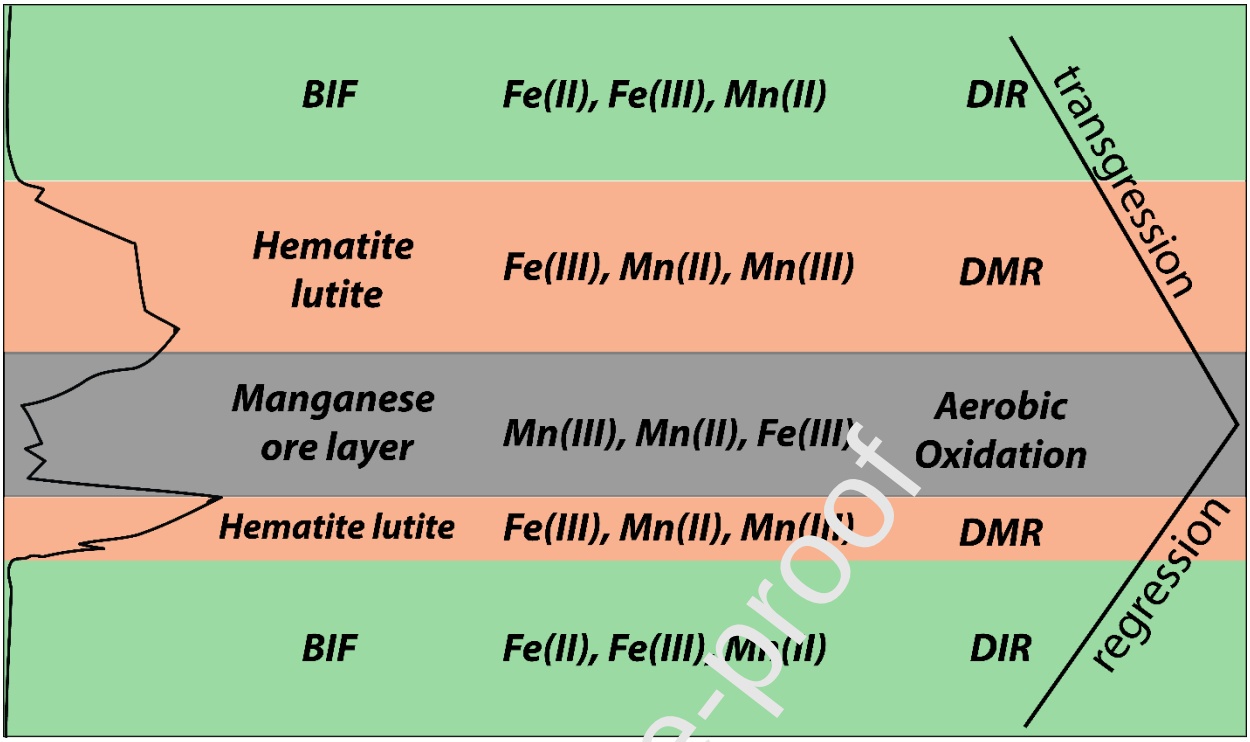

20

Abstract

The 2.4Ga Hotazel Formation is a cyclically interlayered sequence of banded iron formation (BIF) and manganese-rich sedimentary rock at the uppermost part of the Neoarchaean-Palaeoproterozoic Transvaal Supergroup in South Africa. It represents an unusual stratigraphic association in the context of the origin of BIF and the coevolution of oxygen and life on early Earth and hence bears special relevance to the environmental conditions and processes that characterized the period leading up to the Great Oxidation Event (GOE) at *ca.* 2.3Ga. The mineral assemblages that characterize the Hotazel rocks are dominated by carbonate, silicate and oxide minerals, which are traditionally interpreted as predominantly diagenetic in origin, particularly the carbonates. By contrast, primary mineral assemblages are inferred to have been dominated by ferric oxyhydroxides and tetravalent manganese oxides, which show no preservation in the rock record and consequently hinder reconstruction of environmental conditions during sedimentation. Here, we revisit the Hotazel succession with a focus on its bulk-rock and carbonate-specific mineralogical, geochemical and stable isotope (C, Fe) composition by applying for the first time a high-resolution stratigraphic approach to sampling and analysis. Our main aim is to constrain the precursor mineralogy to the Fe- and Mn-rich facies in the Hotazel strata in order to unravel the redox conditions behind the massive cyclic deposition of Fe and Mn at the onset of the GOE. Our carbonate-specific results question traditional diagenetic models for the development of the carbonate fraction of the rocks and instead place the origin of much of the present mineralogy on water-column processes in a stratified basin characterized by successive redox pathways with changing water depth. These pathways exploited a series of thermodynamically predictable electron acceptors for organic carbon recycling, which included – probably for the first time in Earth history – aqueous Mn(III) and O_2 as electron acceptors for the oxidation of both Fe(II) and organic carbon. The emergence of Mn(III) was also critical for the development of a Mn redox shuttle, which led to effective water-column stratification between aqueous Mn and Fe in the depositional basin. We conclude that the first known record of Mn(II) to Mn(III) oxidation as recorded in the Hotazel Formation must be a fundamentally diagnostic step in the redox evolution of the oceans and atmosphere in the lead-up to the GOE.

author contribution statement

Mhlanga Xolane, Reginald: Conceptualization, Writing - Original Draft, Investigation, Visualization, Data Curation, Resources, Formal analysis.

Tsikos Harilaos: Conceptualization, Writing - Review & Editing, Supervision, Funding acquisition

Lee Bridget: Resources, Data Curation

Rouxel Olivier: Resources, Data Curation

Boyce Adrian: Resources, Data Curation

Harris Chris: Resources, Data Curation

Lyons Timothy: Conceptualization, Writing - Review & Editing, Supervision, Resources.

Conflict of interest statement

We have no conflicts of interest to disclose.